FACULTY OF
NUCLEAR SCIENCES
AND PHYSICAL
ENGINEERING
CTU IN PRAGUE

MASTER'S THESIS

Study of hadron structure within quantum chromodynamics

Bc. Dagmar Bendová

Supervisor: **Ing. Jan Čepila, PhD., Department of Physics, FNSPE CTU in Prague**

Academic year: 2017/2018

FAKULTA
JADERNÁ
A FYZIKÁLNĚ
INŽENÝRSKÁ
ČVUT V PRAZE

DIPLOMOVÁ PRÁCE

Studium struktury hadronů v rámci kvantové chromodynamiky

Bc. Dagmar Bendová

Školitel: **Ing. Jan Čepila, PhD., Katedra fyziky, FJFI ČVUT v Praze**

Akademický rok: 2017/2018

Prohlášení:

Prohlašuji, že jsem svou diplomovou práci vypracovala samostatně a použila jsem pouze podklady (literaturu, projekty, software, atd.) uvedené v přiloženém seznamu.

Nemám závažný důvod proti použití tohoto školního díla ve smyslu §60 Zákona č. 121/2000 Sb., o právu autorském, o právech souvisejících s právem autorským a o změně některých zákonů (autorský zákon).

V Praze dne 7.5.2018 Dagmar Bendová

Title:

Study of hadron structure within quantum chromodynamics

Author: Bc. Dagmar Bendová

Field of study: Experimental Nuclear and Particle Physics

Project type: Master's thesis

Supervisor: Ing. Jan Čepila, PhD., Faculty of Nuclear Sciences and Physical Engineering, Czech Technical University in Prague

Abstract: In QCD the growth of the gluon density in hadron at high energies (small Bjorken-x) is presumed to be saturated due to the unitarity constraints. The production of vector mesons is sensitive to the gluon distribution in the impact-parameter plane and therefore it represents an excellent probe of the structure of the proton. The evolution of the gluon density with Bjorken-x can be described by the Balitsky–Kovchegov equation (BK). In this work the factorization of the impact-parameter dependence of the dipole amplitude is discussed. The dipole amplitude is obtained from the solution of the BK equation and results are compared to the GBW parametrization. The equation is solved numerically and the input prescriptions are discussed. The main emphasis is given to the exclusive photoproduction and electroproduction of J/ψ. Results are compared to data from HERA and the LHC. Also the predictions for the structure function F_2 are discussed.

Key words: color dipole model, vector mesons, parton saturation, Balitsky–Kovchegov evolution equation, hot-spot model.

Název práce:

Studium struktury hadronů v rámci kvantové chromodynamiky

Autor: Bc. Dagmar Bendová

Obor: Experimentální jaderná a částicová fyzika

Druh práce: Diplomová práce

Vedoucí práce: Ing. Jan Čepila, PhD., Fakulta jaderná a fyzikálně inženýrská, České vysoké učení technické v Praze

Abstrakt: QCD předpovídá saturaci růstu gluonové hustoty v hadronu při vysokých energiích (malých Bjorkenových x) z důvodu zachování unitarity. Produkce vektorových mezonů je citlivá na rozdělení gluonů v příčné rovině, a proto představuje vynikající sondu do struktury protonu. Evoluce gluonové hustoty s Bjorkenovým x může být popsána Balitského–Kovchegovovou rovnicí (BK). V této práci je diskutována možnost faktorizace závislosti dipolové amplitudy na vzdálenosti dipolu a protonu v příčné rovině. Dipolová amplituda je získána řešením BK rovnice a výsledky jsou porovnány s dobře známou GBW parametrizací. Řešení rovnice je provedeno numericky a jsou diskutovány konkrétní volby vstupních možností. Hlavním obsahem práce je exklusivní fotoprodukce a elektroprodukce mezonu J/ψ. Výsledky jsou srovnány s daty z HERY a LHC. Stejně tak jsou srovnány předpovědi strukturní funkce F_2.

Klíčová slova: barevný dipolový model, vektorové mezony, partonová saturace, Balitského–Kovchegovova evoluční rovnice, hot-spot model.

Acknowledgment:

The great gratitude goes to my supervisor Dr. Jan Čepila for his guidance, provided advices, many useful explanations and comments, both on physics and programming, and also for his enourmous patience with my workflow. I would also like to thank to prof. Guillermo Contreras for his many insightful comments on physics and for his support of my work. And of course my greatest gratitude goes to my family and the closest ones who have been here for me during the hard times of my studies.

Contents

Introduction

The structure of a hadron is governed by the strong interaction between its constituents (partons, which are identified with quarks and gluons). Currently, the most succesful theory of strong interaction is the Quantum Chromodynamics (QCD). The growth of the gluon density with increasing energy (resp. with decreasing Bjorken-x) has been predicted from perturbative QCD and at some point, it was also measured experimantally at HERA [1]. However, this growth of the gluon density would result in divergencies which have not been observed. It is therefore expected, that at some point, the new effects arise and tame this growth. Such a phenomenon is called saturation and implies the emergence of a new scale, which is called the saturation scale. The evolution of parton densities with increasing energy can be viewed in two "directions", which correspond to the evolution according to increasing Q^2 or decreasing Bjorken-x. With the increasing scale Q^2 of the process one can observe the hadron with better resolution. Therefore the original parton splits into more "smaller" partons when increasing the resolution. This evolution is described by DGLAP equations. At small Bjorken-x the hadron is dominated by gluons. The linear evolution of gluon densities according to $\ln\left(\frac{1}{x}\right)$ results in the situation in which more gluons of the "same" size appear with decreasing x. At some point the gluon density in the proton is so large, that the their wave functions start to overlap and the gluons therefore recombine and the saturation is reached at this point. One model that describes saturation is the Color Glass Condensate formalism using the JIMWLK equation which accounts for the non-linear evolution of gluon densities. A limit case of the JIMWLK equation is the Balitsky-Kovchegov evolution equation of the dipole scattering amplitude, which is one of the main interests of this work.

The inner structure of hadron can be probed via the deep inelastic scattering (DIS) which is the highly energetic scattering of a lepton off a hadron. The virtual photon is exchanged in the interaction af an incoming lepton with the target hadron, and its inner structure can be observed assuming very short wavelength of the photon. In the exclusive process a vector meson can be produced in the final state. Depending on the scale Q^2 of the process we can distinguish the photoproduction at $Q^2 \to 0$ and the electroproduction at scales $Q^2 \gtrsim 1$. The production of a vector meson is sensitive to the distribution of gluons in the impact parameter plane, therefore this process is expected to be a good probe to search for gluon saturation. Since we expect the emergence of a new particle in the final state, the photon-proton scattering has to be governed by the strong interaction. This can be viewed within the color dipole approach to deep inelastic scattering in which the photon interacts with the hadron via one of its Fock's states. The most probable is the interaction with the $q\bar{q}$ state, hence the "color dipole" in the name of the approach. The amplitude of the $\gamma^* p \to VMp$ process depends on the overlap of the virtual photon and vector meson wavefunctions and the cross section of the interaction of the color dipole with the hadron. The later depends on the impact parameter b between the dipole and the hadron. Under the assumption that the impact parameter b dependence of the dipole-hadron amplitude can be factorized, we can describe the transverse structure of the hadron by an appropriate choice of the profile function. The dipole amplitude then depends only on the Bjorken-x and the transverse size of the dipole and can be obtained as a solution to the b-independent BK equation.

This document is organized as follows. In the first chapter I will introduce deep inelastic scattering (DIS) and the color dipole approach to DIS. Then the production of a vector meson within the color dipole formalism will be described. The QCD evolution equations and the saturation phenonenon will be introduced in the second chapter, including the Balitsky–Kovchegov equation with its main properties and several possible choices for the kernel and the initial condition of the equation.

The third chapter is dedicated to dipole cross sections, which will have been introduced within the color dipole approach of the vector meson production. Their properties are discussed with an emphasis on the choice of factorisation of the impact-parameter b dependent part of the dipole scattering amplitude resulting in two parts of the amplitude – x and dipole size dependent and b-dependent. Within this chapter we describe the procedure to solve the impact parameter independent BK equation and we compare the solutions for different choices of initial conditions, kernel of the integro-differential equation, strong coupling constant behavior or the choice of specific numerical method. Various possible choices of the form of the b-dependent part of the dipole cross section are also discussed in this chapter. One of the recent models is a so-called hot-spot model, which is introduced in this chapter as well.

The main results of this work will be described in the fourth chapter. First, I discuss predictions, from the models introduced before, for the structure function F2, and compare them to the combined DIS data from the H1 and ZEUS experiments at HERA. The rest of the chapter describes the predictions for exclusive J/ψ cross sections. I present three sets of predictions and compare them to the experimentally measured data from HERA and even from the ALICE experiment. First the photoproduction and electroproduction cross sections using a Golec-Biernat–Wusthoff model of the dipole cross section are obtained. In the second part of this chapter I will focus on the exclusive J/ψ photoproduction and electroproduction cross sections obtained using the solution of the Balitsky–Kovchegov equation to determine the dipole cross section. And in the final part of the chapter I will show the results of the predictions for exclusive J/ψ photoproduction and electroproduction cross sections obtained from the GBW parametrization of the dipole cross section when using the hot-spot model to obtain the impact parameter b-dependent part of the amplitude.

Chapter 1

Phenomenology of high-energy particle collisions

1.1 Deep Inelastic Scattering

Deep inelastic scattering (DIS) is a highly energetic scattering of an incoming lepton off a hadron. It represents an important processes through which we can study the inner partonic structure of hadrons. The lepton-hadron scattering is denoted by following relation

$$l(k) + N(P) \to l'(k') + X \tag{1.1}$$

and its visual interpretation can be seen in Figure 1.1. In eq. (1.1) l denotes the incoming lepton with four-momentum k and N is the hadron with four-momentum P. An incoming lepton interacts with the hadron via the exchange of a virtual photon γ^* with four-momentum q. The outgoing lepton with four-momentum k' is then represented by l' and X denotes any final state system allowed by conservation laws. The hadron can be either a nucleon or a nucleus with mass number A. However in the following text we will restrict ourselves to lepton-proton interactions. The observed proton structure changes depending on the wavelength, and thus on the transferred momentum, of the virtual photon. When the probing photon has a long wavelength compared to the proton size, a point-like particle with electric charge $+1e$ is seen. With decreasing photon wavelength the proton is first seen as a charged particle with finite size and with even greater decrease of the wavelength, which corresponds to the increase of momentum transfer, the inner structure of the proton becomes observable. The last described case represents the deep inelastic scattering.

1.1.1 Lorentz invariant variables

The kinematics of lepton-nucleon scattering kinematics can be expressed using so-called *Lorentz invariant variables* which are defined as follows [2], [3]

$$s \equiv (P + k)^2 \tag{1.2}$$

$$W^2 \equiv (P + q)^2 = M_X^2 \tag{1.3}$$

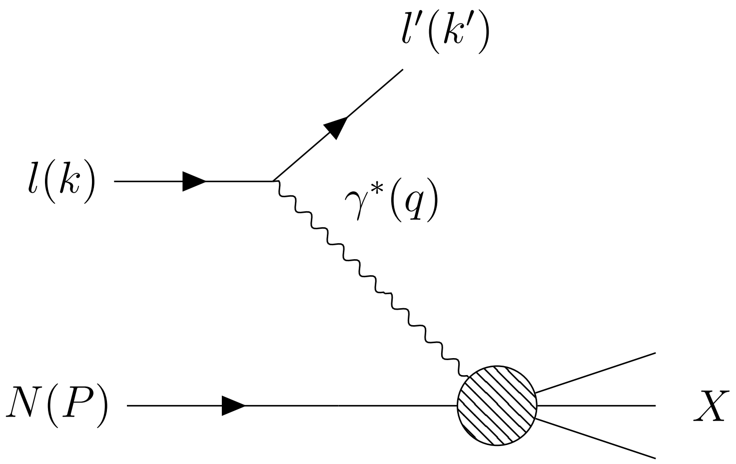

Figure 1.1: A schematic diagram of the electron-proton scattering. The incoming, resp. outcoming lepton four-momentum is denoted by k, resp. k', q denotes the virtual photon γ^* four-momentum, P denotes the incoming hadron four-momentum and X denotes the final state system.

$$Q^2 \equiv -q^2 = -(k - k')^2 \tag{1.4}$$

$$x \equiv \frac{Q^2}{2P \cdot q} \tag{1.5}$$

$$y \equiv \frac{P \cdot Q}{P \cdot k} \tag{1.6}$$

$$\nu \equiv \frac{P \cdot q}{m_p} \tag{1.7}$$

The Mandelstam variable s represents the total energy of the interaction in the centre-of-mass (CMS) frame and W^2 represents the centre-of-mass energy of the photon-proton system which is equal to the square of invariant mass M_X of the produced hadronic system X. The square of the momentum transferred from lepton to proton q^2 determines the photon virtuality Q^2. Relation (1.5) defines the *Bjorken-x*. In the infinite momentum frame it can be interpreted as the fraction of the target proton's longitudinal momentum carried by one of its constituents (called *partons*). The inelasticity y represents the fraction of the lepton energy carried by the virtual photon and ν is the total energy passed from the lepton to the proton, with mass m_p, in the target's rest frame.

1.1.2 DIS cross section and parton model

The basic quantity describing any general scattering process such as (1.1) is the differential cross section. One can calculate it by obtaining the invariant amplitude of the process which in the case of deep inelastic scattering of electron on proton can be written [3] as the contraction of two tensors $L^{\mu\nu}$, $W_{\mu\nu}$

$$\overline{|M_{fi}|^2} = \frac{e^4}{Q^4} L^{\mu\nu}(k,k')W_{\mu\nu}(P,q), \tag{1.8}$$

where

$$L^{\mu\nu}(k,k') = 2\left[k^{\mu}k'^{\nu} + k^{\nu}k'^{\mu} - g^{\mu\nu}(k\cdot k')\right] \tag{1.9}$$

is the tensor associated with the vertex at which the lepton emits the virtual photon, assuming we can neglect the electron mass. Unlike the photon emission from the lepton, which is a well understood process in Quantum Electrodynamics (QED), its interaction with the proton can not be directly computed using perturbative Quantum Chromodynamics because the proton structure is completely unknown at this stage. However we can parametrize the photon-proton interaction by introducing the hadronic tensor $W_{\mu\nu}$. Eliminating the parity violating term and the terms which result zero in the contraction of the tensors [3] the resulting hadronic tensor can be written as

$$W_{\mu\nu}(P,q) = -W_1 g_{\mu\nu} + W_2\frac{P_\mu P_\nu}{m_p^2}, \tag{1.10}$$

where m_p is the proton mass and W_1, W_2 are the inelastic form factors, which parametrize the photon-proton coupling. The contraction is then

$$L^{\mu\nu}W_{\mu\nu} = \frac{4(k\cdot P)}{y}\left[xy^2 W_1 + \frac{\nu}{m_p}W_2\left(1 - y - \frac{xym_p^2}{Q^2}\right)\right]. \tag{1.11}$$

It is common to introduce another pair of dimensionless functions - F_1 and F_2. They are called the *structure functions* and are related to inelastic form factors as

$$F_1 \equiv W_1; \qquad F_2 \equiv \frac{\nu}{m_p}W_2. \tag{1.12}$$

In general, they depend on x and Q^2 of the process. The QCD-related part of the scatterring is now included in the structure functions of the proton. One can thus rewrite the lepton-proton tensor contraction (1.13) using functions (1.12) as

$$L^{\mu\nu}W_{\mu\nu} = \frac{4(k\cdot P)}{y}\left[xy^2 F_1(x,Q^2) + \left(1 - y - \frac{xym_p^2}{Q^2}\right)F_2(x,Q^2)\right]. \tag{1.13}$$

and express the differential cross section in the limit of high energies $s >> M$ as

$$\frac{\mathrm{d}^2\sigma}{\mathrm{d}x\mathrm{d}Q^2} = \frac{4\pi\alpha^2}{Q^4}\left[y^2 F_1(x,Q^2) + (1-y)\frac{F_2(x,Q^2)}{x}\right], \tag{1.14}$$

where $\alpha = \frac{e^2}{4\pi} \approx \frac{1}{137}$ is the electromagnetic coupling constant.

In Feynmann's parton model [4, 5] the deep inelastic scattering is seen as the scattering of the virtual photon on one of the partons which constitute the inner structure of the proton. The

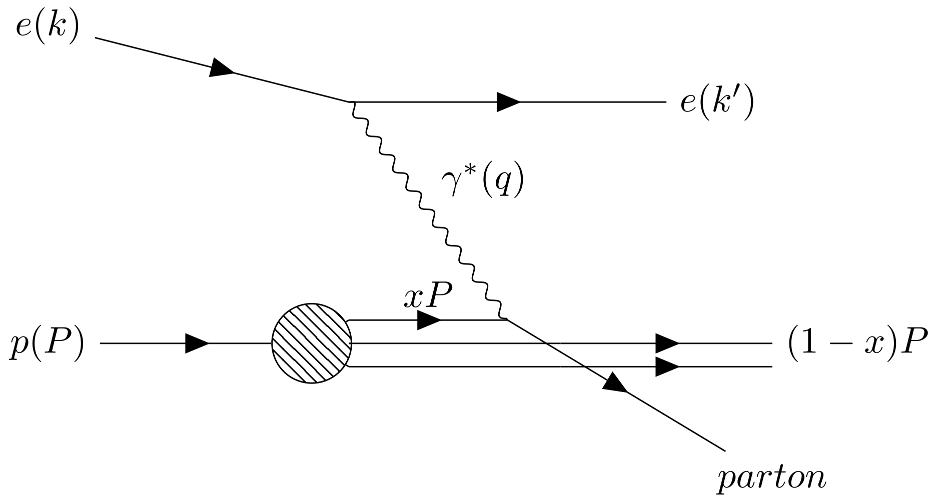

Figure 1.2: Sketch of the parton model interpretation of the deep inelastic scattering, according to [6].

situation is illustrated in Figure 1.2. In the infinite momentum frame one can neglect the masses of particles. The incoming particles also carry only the longitudinal part of the momentum. Partons inside the proton carry the fraction of this momentum which is equivalent to Bjorken-x (1.5) as mentioned in the previous section. The differential cross section of the electron-parton scattering is then given as

$$\frac{\mathrm{d}^2\sigma}{\mathrm{d}x\mathrm{d}Q^2} = \frac{4\pi\alpha^2}{Q^4}\left[(1-y)+\frac{y^2}{2}\right]\sum_i e_i^2 f_i(x), \tag{1.15}$$

where the sum runs over all parton flavours, e_i is the effective charge of the parton of flavour i and $f_i(x)$ represents its parton distribution function.

Comparing this relation to the above derived relation (1.15) for the electron-proton scattering cross section and with the assumption that partons are spin-$\frac{1}{2}$ particles, one can obtain the following expressions for the structure functions

$$F_1(x) = \frac{1}{2}\sum_i e_i^2 f_i(x), \qquad F_2(x) = \sum_i e_i^2 x f_i(x); \tag{1.16}$$

leading to the so-called *Callan-Gross relation*

$$F_2(x) = 2xF_1(x). \tag{1.17}$$

Note that structure functions are independent of Q^2 in the quark-parton model. This phenomenon is called *Bjorken scaling* [7]. The Q^2 dependence of structure functions can be obtained from the so-called DGLAP evolution equation which will be briefly introduced in the following chapter.

Structure functions can also be expressed using the total cross section $\sigma^{\gamma^* p}$ of the photon-proton interaction, which consists of two parts [3]

$$\sigma^{\gamma^* p} = \sigma_T + \sigma_L = C\left(1 + \frac{Q^2}{4M^2x^2}W_2\right) \tag{1.18}$$

where C is the overall normalization factor [3] given by

$$C = \frac{8\pi^2\alpha}{W^2 - M^2 + Q^2}, \tag{1.19}$$

and

$$\sigma_T = CW_1, \qquad \sigma_L = C\left[-W_1 + \left(1 + \frac{Q^2}{4M^2x^2}\right)W_2\right] \tag{1.20}$$

correspond to the cross section of transversaly, resp. longitudinally polarized photons scattering off the nucleon. One can then define the transverse structure function F_T as

$$F_T \equiv \frac{2x}{C}\sigma_T = 2xF_1, \tag{1.21}$$

and then the relation for the structure function F_2 can be obtained as

$$F_2 = \frac{2x}{C}\left[\frac{Q^2}{Q^2 + M^2x^2}\right](\sigma_T + \sigma_L) \doteq F_T + F_L. \tag{1.22}$$

Experimental measurements of the structure functions are often expressed in dependence on the *reduced cross section* defined as [1]

$$\sigma_r(y, x, Q^2) = F_2(x, Q^2) - \frac{y^2}{1 + (1 - y^2)}F_L(x, Q^2). \tag{1.23}$$

As can be seen the longitudinal structure function F_L is

$$F_L = F_2 - 2xF_1. \tag{1.24}$$

It represent the measure of the violation of the Callan-Gross relation (1.17) as the $F_L = 0$ if the proton consists of only spin-$\frac{1}{2}$ fermions (i.e. quarks) [8]. The longitudinal structure function therefore gives a direct measure of the gluonic contribution to the proton inner structure.

The F_2 structure function and deep inelastic scattering cross section measurements were carried out with great precision by the H1 and ZEUS experiments at HERA [1, 9].

1.2 Color dipole model of the DIS

The dipole model provides a framework to describe the strong interaction within the deep inelastic scattering. In the target proton's rest frame the photon can fluctuate into a quark-antiquark pair. The transverse size of the pair is denoted as $\vec{r}$ and the quark carries a fraction z of the photon's light-cone momentum [8, 10, 11]. The lifetime of the $\gamma^* \to q\bar{q}$ fluctuation is much longer than the timescale of the interaction under the condition that

$$x \ll \frac{1}{MR}$$

where M and R are the target proton mass and radius, respectively. Thus, it is apparent that the color dipole approach is valid at small x which corresponds to high energies. The $\gamma^* p$ scattering is then assumed to proceed in the following stages: first the incoming virtual photon fluctuates into a $q\bar{q}$ dipole, then the dipole interacts strongly with the target proton via the exchange of a colorless state. In the first approximation we consider this state to be a pair of gluons and the actual exchanged particle is often called Pomeron [12]. In the last stage of the interaction the $q\bar{q}$ pair recombines back to form the virtual photon. The whole process is depicted in Fig. 1.3.

The total elastic $\gamma^* p \to \gamma^* p$ cross section of the deep inelastics scattering can be obtained from the optical theorem [10, 12] as

$$\sigma_{T,L}^{\gamma^* p}(x, Q^2) = \mathrm{Im}\mathcal{A}_{T,L}^{\gamma^* p}(x, Q^2, \Delta = 0) = \sum_f \int \mathrm{d}^2 r \int \mathrm{d}z |\Psi^* \Psi|_{T,L}^f \sigma_{q\bar{q}}(\tilde{x}, r) \tag{1.25}$$

where $\mathcal{A}_{T,L}^{\gamma^* p}$ is the scattering amplitude for the elastic $\gamma^* p \to \gamma^* p$ process, $|\Psi^* \Psi|_{T,L}^f$ is the overlap of transversaly, resp. longitudinally, polarised virtual photon wave functions, $\sigma(\tilde{x}, r)_{q\bar{q}}$ is the cross section of the dipole-proton scattering and Δ denotes the transverse momentum lost by the outgoing proton.

Note that the dipole amplitude $N(\tilde{x}, r)$ (resp. the dipole cross section $\sigma_{q\bar{q}}$) in DIS is evaluated at

$$\tilde{x} = x\left(1 + \frac{4m_f^2}{Q^2}\right), \tag{1.26}$$

which represents a kinematical shift in the definition of Bjorken-x [13]. The shift is made in order to approach safely the photoproduction limit.

The photon wave function can be derived from the QED and the square of the wave functions, summed over the polarizations of virtual photon and $q\bar{q}$ helicities, can be written [8, 11, 14] as

$$|\Psi^* \Psi|_T^f = \frac{3\alpha}{2\pi^2} e_f^2 \left[\left(z^2 + (1-z)^2\right) \epsilon^2 K_1^2(\epsilon r) + m_f^2 K_0^2(\epsilon r)\right], \tag{1.27}$$

$$|\Psi^* \Psi|_L^f = \frac{3\alpha}{2\pi^2} e_f^2 \left[4Q^2 z^2 (1-z)^2 K_0^2(\epsilon r)\right], \tag{1.28}$$

where T and L refer to transverse and longitudinal polarization of the virtual photon, e_f is the electric charge of the quark of flavour f in the units of elementary charge, K_0 and K_1 are the modified Bessel functions of the second kind (see eq. A.24 defined in Appendix A), $r \equiv |\vec{r}|$ and

$$\epsilon^2 = z(1-z)Q^2 + m_f^2, \tag{1.29}$$

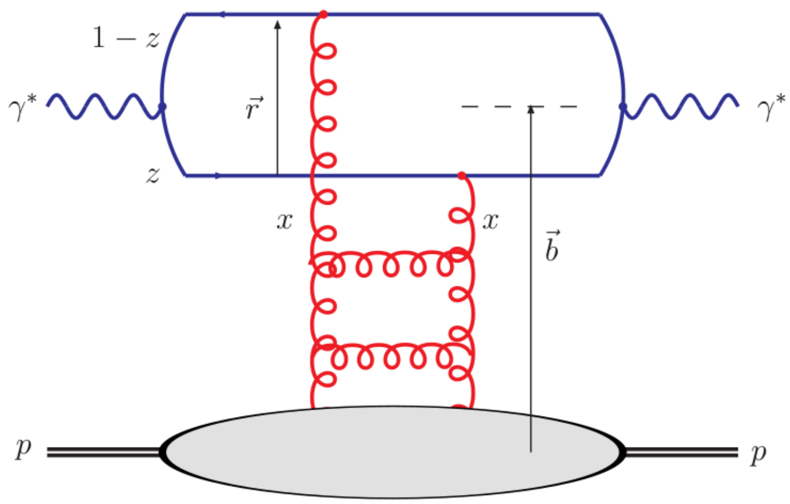

Figure 1.3: Schematic diagram of the elastic scattering of a virtual photon off the proton in the color dipole picture for inclusive DIS [10].

where m_f is an effective mass of the quark with flavour f.

The total cross section $\sigma_{q\bar{q}}$ for the $q\bar{q}$ scattering on the proton can be (again using the optical theorem [8, 10, 12]) obtained from the dipole amplitude $N(x, r, b)$ which represents the imaginary part of the dipole-proton scattering amplitude as follows:

$$\sigma_{q\bar{q}}(\tilde{x}, r) = 2 \int \mathrm{d}^2 b N(\tilde{x}, r, b) = \sigma_0 N(\tilde{x}, r), \tag{1.30}$$

where we assumed the average over the impact parameter [15] considering the target is finitely big and homogeneous. The resulting σ_0 parameter has the interpretation as the average area of the quark distribution in the transverse plane and it can be obtained from a fit to experimentally measured data.

The dipole cross section $\sigma_{q\bar{q}}$ can be obtained from various parametrizations and models such as the GBW parametrization [13, 16], which was one of the first succesfull parametrizations of the dipole cross section, or the BGBK model [17] or the CGC model [18], etc. In the following, I will use only the GBW approach which parametrizes the dipole cross section as

$$\sigma_{q\bar{q}}^{\mathrm{GBW}}(x, r) = \sigma_0 \left[1 - \exp\left(-\frac{r^2 Q_s^2(x)}{4} \right) \right] \equiv \sigma_0 N(x, r), \tag{1.31}$$

where $Q_s(x)$ denotes the x-dependent saturation scale

$$Q_s^2(x) = Q_0^2 \left(\frac{x_0}{x} \right)^{\lambda_{\mathrm{GBW}}} \ [\mathrm{GeV}^2], \tag{1.32}$$

which is closely related to the gluon density in the transverse plane. The exponent λ_{GBW} determines the growth of the dipole cross section with decreasing x and Q_0, x_0 are free parameters. For large dipoles the cross section saturates and its value approaches the constant σ_0.

The dipole cross section can also be obtained as a solution to the Balitsky-Kovchegov evolution equation for the dipole scattering amplitude $N(x, r)$ (see Section 2.3.2 and Section 3.2). The scattering amplitude reaches values between 0 and 1, where the latter corresponds to a saturated state (see Chapter 2.3.2). At fixed x the dipole amplitude behaves as $N \to 0$ for dipoles with small transverse size $r \to 0$ due to color transparency and for big dipoles $N \to 1$ as it is more probable for the big dipole to interact with the proton. On the other hand, for fixed values of r and with decreasing x the dipole amplitude grows towards one because with increasing energy the number of gluons grows and it is therefore more probable for the dipole to interact with such a dense target.

Using the result (1.22) and with (1.19) we can obtain the relation for the structure function F_2 in the limit of small Bjorken-x

$$F_2(x, Q^2) = \frac{Q^2}{4\pi^2\alpha}(\sigma_T + \sigma_L), \tag{1.33}$$

which depends on the transverse and longitudinal photon-proton cross section defined in eq. (1.25).

1.3 Production of vector mesons

In high-energy scattering processes, such as deep inelastic scattering introduced in the previous section, one can observe so-called diffractive events. Their main signature is the presence of a large rapidity gap, which is an interval of few units of rapidity in which no particle are produced.

One of the interesting scenarios is the exclusive production of vector mesons. These processes represent a uniquely clear environment for the studies of cross sections of various vector mesons such as J/ψ, $\psi(2S)$, ρ, ϕ or even Υ mesons due to the presence of areas where no other particles are observed. These processes can also serve as excellent probes of the proton shape and partonic structure; specifically gluon densities at low-x can be studied. An example of diffractive scattering process can be seen in Figure 1.4, where X in general represents any created system of particles, however here the system X is taken to be a produced vector meson. The photon-proton interaction is viewed as a pomeron exchange. The fraction of the proton longitudinal momentum carried by the pomeron is defined as

$$x_{\mathbb{P}} = \frac{(P - P')\cdot q}{P \cdot q} = \frac{M_{VM}^2 + Q^2 - t}{W^2 + Q^2 - m_p^2}, \tag{1.34}$$

where M_{VM} and m_p are the masses of the produced vector meson and proton, respectively. The momentum transfer $t = (P - P')^2$ is related to Δ introduced in Chapter 1.2 as

$$\Delta^2 = -t.$$

Note that besides exclusive production, dissociative vector meson production — where the scatterred proton is broken into a hadronic system — is also possible.

Production of a vector meson in deep inelastic scattering can be well described within the color dipole approach presented in Chapter 1.2, where the photon wave function is obtained

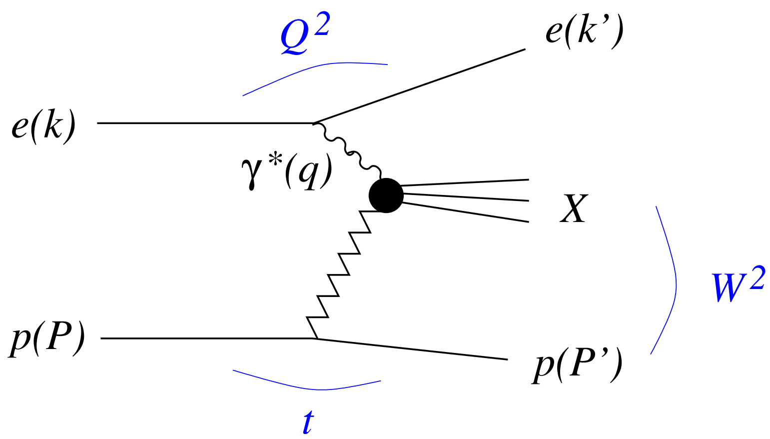

Figure 1.4: Schematic diagram of the diffractive scattering in DIS. The incoming, resp. outgoing electron four-momentum is denoted by k, resp. k', q denotes the virtual photon γ^* four-momentum and P, resp. P' denotes the incoming, resp. outgoing proton four-momentum. Q^2 respresents the virtuality of γ^* defined as (1.4), W^2 denotes the photon-proton centre-of-mass energy defined as (1.3), t is the squared four-momentum transfer of the proton [19].

from QED and the vector meson wave functions are determined from a phenomenological model. The graphical interpretation of the situation can be seen in Figure 1.5.

The amplitude for the exclusive production of a vector meson in the final state [10] is given by

$$\mathcal{A}_{T,L}^{\gamma^* p \to VMp} = \int \mathrm{d}^2 r \int_0^1 \frac{\mathrm{d}z}{4\pi} |\Psi_{VM}^* \Psi_{\gamma^*}| \mathcal{A}_{q\bar{q}}(x, r, \Delta), \tag{1.35}$$

where $|\Psi_{VM}^* \Psi_{\gamma^*}|$ denotes the overlap of the photon and vector meson wave functions. Note that x in this case represents Bjorken-x of the exchanged pomeron

$$x = \frac{M_{VM}^2 + Q^2}{W^2 + Q^2}, \tag{1.36}$$

derived from relation (1.34) under the assumption of large W^2 in the electroproduction. In the photoproduction the relation (1.36) is further simplified to

$$x = \frac{M_{VM}^2}{W^2}. \tag{1.37}$$

Following [10, 20], the invariant amplitude (1.35) can be rewritten as

$$\mathcal{A}_{T,L}^{\gamma^* p \to VMp} = i \int \mathrm{d}^2 r \int_0^1 \frac{\mathrm{d}z}{4\pi} \int \mathrm{d}^2 b |\Psi_{VM}^* \Psi_{\gamma^*}|_{T,L} \exp\left[-i\left(\vec{b} - (1-z)\vec{r}\right)\vec{\Delta}\right] \frac{\mathrm{d}\sigma_{q\bar{q}}}{\mathrm{d}^2 b}, \tag{1.38}$$

where $\vec{b}$ represents the impact parameter between the proton and the dipole, see Figure 1.5.

With the assumption that the trasverse profile of the proton does not have an angular dependence, we can perform the angular integrations in the amplitude and reduces the prescription to

$$\mathcal{A}_{T,L}^{\gamma^* p\to VMp} = i\int_0^\infty \mathrm{d}r 2\pi r\int_0^1 \frac{\mathrm{d}z}{4\pi}\int_0^\infty \mathrm{d}b 2\pi b |\Psi_{VM}^*\Psi_{\gamma^*}|_{T,L} J_0(b\Delta) J_0\left((1-z)r\Delta\right)\frac{\mathrm{d}\sigma_{q\bar{q}}}{\mathrm{d}^2 b}, \tag{1.39}$$

with J_0 being the Bessel function of the first kind (A.21) and $\frac{\mathrm{d}\sigma_{q\bar{q}}}{\mathrm{d}^2 b}$ represents the differential $q\bar{q}$-proton cross section which in general depends on the impact parameter b.

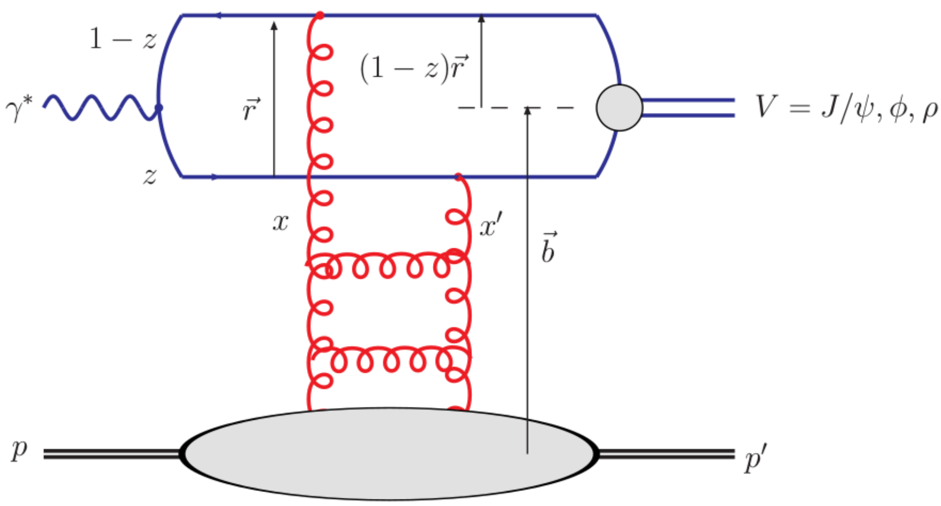

Figure 1.5: Schematic diagram of the elastic scattering of a virtual photon off the proton in the color dipole picture for exclusive vector meson production [10].

1.3.1 Wave functions

The overlap of a the virtual photon and the vector meson wave functions is defined as [15]

$$|\Psi_{VM}^*\Psi_{\gamma^*}|_T = \frac{1}{2}\sum_{h\bar{h}}\left(\Psi^*_{VM,h\bar{h},\lambda=1}\Psi_{\gamma^* h\bar{h},\lambda=1} + \Psi^*_{VM,h\bar{h},\lambda=-1}\Psi_{\gamma^* h\bar{h},\lambda=-1}\right), \tag{1.40}$$

$$|\Psi_{VM}^*\Psi_{\gamma^*}|_L = \sum_{h\bar{h}}\Psi^*_{VM,h\bar{h},\lambda=0}\Psi_{\gamma^* h\bar{h},\lambda=0}, \tag{1.41}$$

where sum runs over $q\bar{q}$ helicities and λ is the polarization of the virtual photon.

The photon wave functions are calculated using perturbative QED, see [14]. The vector meson wave functions are modelled following the presumption that the vector meson is predominantly a $q\bar{q}$ state with the same spin and polarization structure as in the photon case [15].

The overlap between the photon and vector meson wave functions reads [10]

$$|\Psi_{VM}^*\Psi_{\gamma^*}|_T = \hat{e}_f e\frac{N_C}{\pi z(1-z)}\left[m_f^2 K_0(\epsilon r)\phi_T(r,z) - \left(z^2+(1-z)^2\right)\epsilon K_1(\epsilon r)\partial_r\phi_T(r,z)\right], \tag{1.42}$$

$$|\Psi^*_{VM}\Psi_{\gamma^*}|_L = \hat{e}_f e \frac{N_C}{\pi} 2Qz(1-z)K_0(\epsilon r)\left[M_{VM}\phi_L(r,z) + \delta \frac{m_f^2 - \nabla_r^2}{M_{VM}z(1-z)}\phi_L(r,z)\right], \tag{1.43}$$

where $\hat{e}_f$ represents the effective charge of the given vector meson, m_f is the mass of the quark of flavour f, K_0 and K_1 are Bessel functions of the second kind (A.24) and ϵ was already defined in (1.29). The parameter δ is chosen to be 0 or 1 according to one's choice to exclude or include non-local part of the wave function in the overlap (1.43).

The scalar part $\phi_{T,L}$ of the wave function is in general model-dependent. For the photon case they are given by modified Bessel functions (A.24). In the vector meson case they are obtained under the assumption that a hadron at rest can be modelled by a Gaussian distribution in the transverse plane. Various models of the scalar wave functions are used, for their review see e.g. [10]. In the following work I use the boosted Gaussian model [21, 22, 23] in which the scalar parts of the wave functions for first excited states are given as

$$\phi_{T,L}(r,z) = N_{T,L}z(1-z)\exp\left[-\frac{m_f^2R^2}{8z(1-z)} - \frac{2z(1-z)r^2}{R^2} + \frac{m_f^2R^2}{2}\right], \tag{1.44}$$

with its derivatives being

$$\partial_r\left(\phi_{T,L}(r,z)\right) = -\frac{4z(1-z)r}{R^2}\phi_{T,L}(r,z), \tag{1.45}$$

$$\nabla_r^2\left(\phi_{T,L}(r,z)\right) = \left[\frac{2}{r} - \frac{4z(1-z)r}{R^2}\right]\partial_r\left(\phi_{T,L}(r,z)\right). \tag{1.46}$$

For the full calculation of derivates of the scalar parts $\phi_{T,L}$ of the wave functions see Appendix C. The constants $N_{T,L}$ and R are determined from the normalization conditions and from the leptonic decay width of the vector meson, see [10].

1.3.2 Differential and total cross section

The formula for the transversal and longitudinal differential cross section for exclusive photoproduction of vector mesons is given as

$$\frac{\mathrm{d}\sigma_{T,L}^{\gamma^* p\to VMp}}{\mathrm{d}|t|} = \frac{1}{16\pi}|\mathcal{A}_{T,L}^{\gamma^* p\to VMp}|^2,. \tag{1.47}$$

For the purpose of this work the amplitude $\mathcal{A}_{T,L}^{\gamma^* p\to VMp}$ given by (1.39) can be rewritten as

$$\mathcal{A}_{T,L}^{\gamma^* p\to VMp} = i\pi\sigma_0 A_b \cdot (A_r)_{T,L}, \tag{1.48}$$

with corresponding parts of the amplitude given by following relations

$$A_b = \int_0^\infty \mathrm{d}b\left(bJ_0(b\Delta)T_p(b)\right), \tag{1.49}$$

$$(A_r)_{T,L} = \int_0^\infty \mathrm{d}r \left(rN(x,r)(A_z)_{T,L}\right), \tag{1.50}$$

$$(A_z)_{T,L} = \int_0^1 \mathrm{d}z \left(|\Psi^*_{VM}\Psi_{\gamma^*}| J_0\left[r\Delta(1-z)\right]\right). \tag{1.51}$$

Resulting differential cross section for the exclusive process is then given as a sum of transversal and longitudinal contributions

$$\frac{\mathrm{d}\sigma^{\gamma^* p\to VMp}}{\mathrm{d}|t|} = \frac{\mathrm{d}\sigma_T^{\gamma^* p\to VMp}}{\mathrm{d}|t|} + \frac{\mathrm{d}\sigma_L^{\gamma^* p\to VMp}}{\mathrm{d}|t|} = \frac{1}{16\pi}\left(|\mathcal{A}_T^{\gamma^* p\to VMp}|^2 + |\mathcal{A}_L^{\gamma^* p\to VMp}|^2\right). \tag{1.52}$$

The total cross section can be obtained by integrating the differential cross section (1.52) over the t in the range given by experimental data:

$$\sigma(x,Q^2) = \int \mathrm{d}|t| \frac{\mathrm{d}\sigma}{\mathrm{d}|t|}. \tag{1.53}$$

1.3.2.1 Phenomenological corrections to the cross section

Correction on the real part of the scattering amplitude

The expression for the cross section of exclusive vector meson production (1.52) is obtained under the assumption that the S-matrix is purely real and therefore the scattering amplitude (1.35) is purely imaginary. One can take into account the real part of the amplitude by multiplying the transversal and longitudinal scattering amplitude (1.39) by a factor $\sqrt{1+\beta_{T,L}^2}$ where $\beta_{T,L}$ is the ratio of real to imaginary parts of the scattering amplitude $\mathcal{A}_{T,L}^{\gamma^* p\to VMp}$ [10] calculated as

$$\beta_{T,L} = \tan\left(\frac{\pi\lambda_{T,L}}{2}\right), \qquad \lambda \equiv \frac{\partial \ln\left(\mathcal{A}_{T,L}^{\gamma^* p\to VMp}\right)}{\partial \ln\left(\frac{1}{x}\right)}. \tag{1.54}$$

Performing the derivative in (1.54) for the GBW parametrization (1.31) one gets

$$\lambda_{T,L} = \frac{1}{\mathcal{A}_{T,L}^{\gamma^* p\to VMp}} \frac{\partial\left(\mathcal{A}_{T,L}^{\gamma^* p\to VMp}\right)}{\partial \ln\left(\frac{1}{x}\right)} =$$

$$= \frac{1}{\mathcal{A}_{T,L}^{\gamma^* p\to VMp}} i \int_0^\infty \mathrm{d}r 2\pi r \int_0^1 \frac{\mathrm{d}z}{4\pi} \int_0^\infty \mathrm{d}b 2\pi b |\Psi^*_{VM}\Psi_{\gamma^*}|_{T,L} J_0(b\Delta) J_0\left((1-z)r\Delta\right) \frac{\partial}{\partial \ln\left(\frac{1}{x}\right)} \left(\frac{\mathrm{d}\sigma_{q\bar{q}}}{\mathrm{d}^2 b}\right) =$$

$$= \frac{\lambda_{\mathrm{GBW}} Q_s^2(x)}{4} \cdot \frac{\int_0^\infty \mathrm{d}r \left(r^3 \exp\left[-\frac{r^2 Q_s^2(x)}{4}\right](A_z)_{T,L}\right)}{(A_r)_{T,L}}.$$

Skewedness correction

Since the two gluons in the diagram in Figure 1.5 in general carry different proton momenta fractions x and x' one should use the off-diagonal gluon distribution [15]. The skewed effect can be accounted for in the limit of $x' \ll x \ll 1$ by multiplying the transversal and longitudinal scattering amplitude (1.39) by a factor $(R_g)_{T,L}$ given by [15]

$$R_g(\lambda_{T,L}) = \frac{2^{2\lambda_{T,L}+3}}{\sqrt{\pi}} \frac{\Gamma\left(\lambda_{T,L} + \frac{5}{2}\right)}{\Gamma(\lambda_{T,L} + 4)} \tag{1.55}$$

where $\Gamma(z)$ is the gamma function (A.19) defined in Appendix A and $\lambda_{T,L}$ is obtained from (1.54). However the skewed effect should vanish in the leading $\ln\left(\frac{1}{x}\right)$ limit.

Chapter 2

QCD evolution equations of parton densities

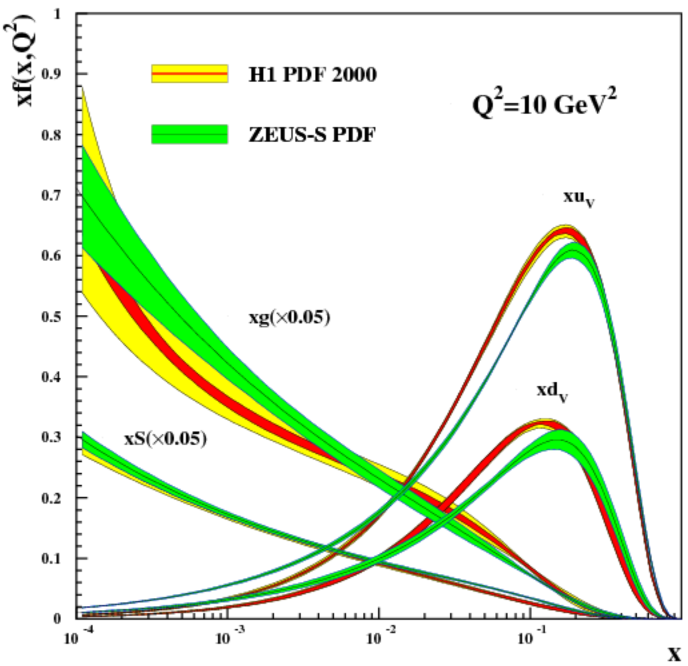

Figure 2.1: The evolution in Bjorken-x of the gluon, sea-quarks and valence-quarks distributions for $Q^2 = 10$ GeV measured at HERA. Sea-quark and gluon distributions have been reduced by a factor of 20 [24].

As proposed in the parton model [4, 5] hadrons are composed of partons which are bound inside it by the strong force. Partons are in general identified with quarks and gluons. The number of quarks and gluons, which is expressed by means of parton distribution functions, changes with the boost of the proton. At low energies, which at fixed Q^2 correspond to large

Bjorken-x since $s \sim \frac{Q^2}{x}$, valence quark distribution functions form the main contribution to the overall structure function F_2 (1.16). However with increasing energy of the hadron, i.e. with decreasing x, more sea quarks and gluons emerge and eventually form the main contribution to the parton density inside the proton. Parton distribution functions for different constituents of the proton as extraxted from HERA data can be seen in Figure 2.1. Note that the sea quark and gluon distributions have been reduced by a factor of 20 in order to fit inside the picture.

The evolution of parton densities with increasing energy can be in fact viewed in two ways. If we fix the Bjorken-x and increase the energy, it results in increasing the scale of the process Q^2. At higher scales one can see the parton content with better resolution and thus more "smaller" partons can be seen. This evolution is described by the DGLAP evolution equations. On the other hand, increasing energy at the scale Q^2 fixed results in smaller Bjorken-x or equivalently it results in higher rapidities $Y = \ln\left(\frac{1}{x}\right)$. According to the BFKL evolution equation, the gluon density grows with decreasing x and one can thus see more partons with the "same" size. The whole situation is depicted in Figure 2.2.

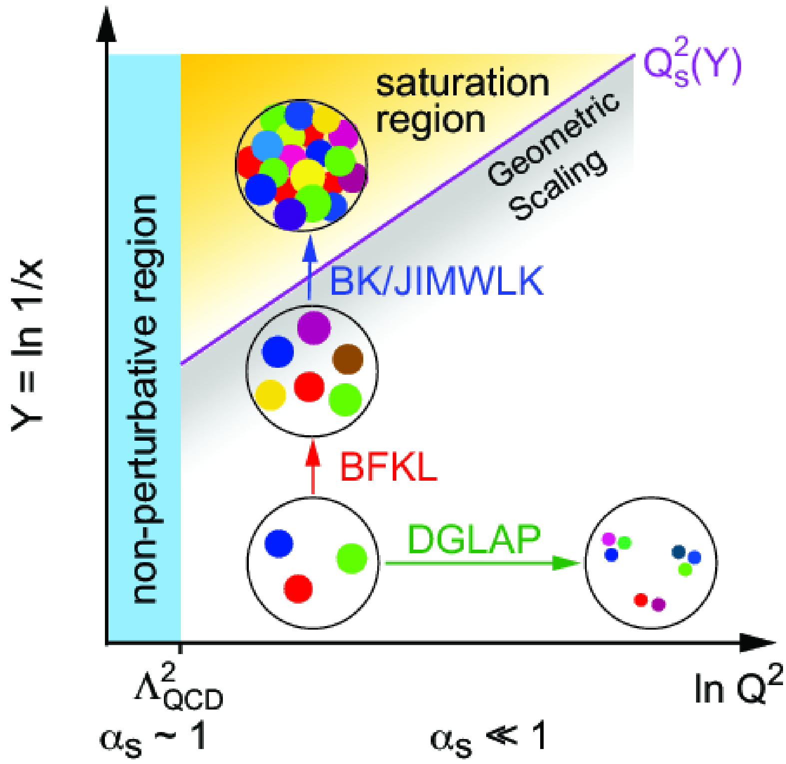

Figure 2.2: Diagram showing the QCD evolution of the partonic structure of the proton and the validity range for the different evolution equations [25].

2.1 DGLAP evolution equations

The Dokshitser–Gribov–Lipatov–Altarelli–Parisi (DGLAP) equations [26, 27, 28] describe the influence of higher order pQCD corrections on the distribution functions of the parton model. They describe the change of the parton size with increasing Q^2 and fixed Bjorken-x, i.e. for higher scales of the interaction. The DGLAP equations at leading-logarithmic order can be written as [29]

$$\frac{\mathrm{d}q_f(x,Q^2)}{\mathrm{d}\ln Q^2} = \frac{\alpha_S}{2\pi}\int_x^1 \frac{\mathrm{d}y}{y}\left[q_f(y,Q^2)P_{qq}\left(\frac{x}{y}\right) + g(y,Q^2)P_{qg}\left(\frac{x}{y}\right)\right], \tag{2.1}$$

$$\frac{\mathrm{d}g(x,Q^2)}{\mathrm{d}\ln Q^2} = \frac{\alpha_S}{2\pi}\int_x^1 \frac{\mathrm{d}y}{y}\left[\sum_f q_f(y,Q^2)P_{gq}\left(\frac{x}{y}\right) + g(y,Q^2)P_{gg}\left(\frac{x}{y}\right)\right], \tag{2.2}$$

where α_S is the running coupling constant of the strong interaction, $q_f(y,Q^2)$, resp. $g(y,Q^2)$, represents the distribution function of a quark with flavour f, resp. a gluon, with a momentum fraction y and a virtuality Q^2 and the sum in eq. (2.2) runs over quarks and antiquarks of all flavours, i.e. $f = 1, ..., n_f$.

The functions $P_{ij}(z)$ are the *Altarelli-Parisi splitting functions* given as

$$P_{qq} = \frac{4}{3}\frac{1+z^2}{(1-z)_+} = P_{gq}(1-z), \tag{2.3}$$

$$P_{qg}(z) = \frac{1}{2}\left(z^2 + (1-z)^2\right) = P_{qg}(1-z), \tag{2.4}$$

$$P_{gq}(z) = \frac{4}{3}\frac{1+(1-z)^2}{z} = P_{qq}(1-z), \tag{2.5}$$

$$P_{gg}(z) = 6\left(\frac{1-z}{z} + \frac{z}{(1-z)_+} + z(1-z)\right) = P_{gg}(1-z). \tag{2.6}$$

The regularization "+ prescription" [29] is defined as

$$\int_0^1 \mathrm{d}z\frac{f(z)}{(1-z)_+} = \int_0^1 \mathrm{d}z\frac{f(z)-f(1)}{1-z}, \tag{2.7}$$

where $(1-z)_+ = (1-z)$ for $z < 1$ but infinite at $z = 1$.

The evolution of parton densities is thus governed by the P_{qq}, P_{qg}, P_{gq} and P_{gg} functions. The function P_{qq} represents the probability that a quark emits a gluon which results in a quark with momentum reduced by a fraction z. The function P_{qg} represents the probability that a gluon converts into a $q\bar{q}$ pair with the quark carrying a fraction z of the gluon momentum and thus the antiquark carrying a momentum fraction $(1-z)$. Similarly, the P_{gq} function represents the probability that a quark-antiquark pair annihilates into a gluon which carries a fraction z of the original quark momentum. And finally the P_{gg} function gives the probability that a gluon emits another gluon via the triple-gluon vertex which results in a gluon with momentum reduced by a fraction z.

The first of DGLAP equations (2.1) therefore expresses the situation that a quark with momentum fraction x could have originated from a parent quark with a larger momentum fraction y, which has radiated a gluon, or it could have originated from the gluon with momentum fraction y, which has fluctuated into a $q\bar{q}$ pair. The second DGLAP equation (2.2) represents a similar evolution for gluons governed by the functions P_{gq} and P_{gg}. This means that a gluon could have originated from either the $q\bar{q}$ pair annihilation or from the gluon with larger momentum fraction y, which has radiated another gluon [29]. A symbolic graphical interpretation of the gluon DGLAP evolution equation can be seen in Fig. 2.3.

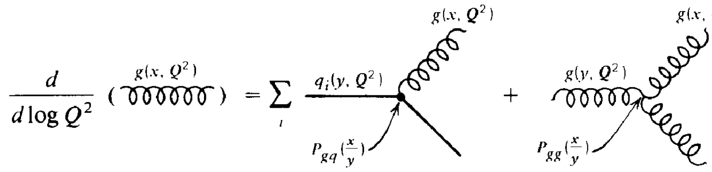

Figure 2.3: Symbolic representation of the gluon evolution equation (2.2). [29]

2.2 BFKL evolution equation

The Balitsky–Fadin–Kuraev–Lipatov (BFKL) evolution equation [30, 31] has been derived for fixed Q^2 and for the small-x limit at which DGLAP equations cease to be valid.

The BFKL equation is formulated for gluons which dominate the small-x region. In leading logarithmic approximation it reads [32]

$$\frac{\partial f(x,k_T^2)}{\partial \ln \frac{1}{x}} = \frac{3\alpha_S}{\pi} k_T^2 \int_0^\infty \frac{\mathrm{d}k_T'^2}{k_T'^2} \left[\frac{f(x,k_T'^2) - f(x,k_T^2)}{|k_T'^2 - k_T^2|} + \frac{f(x,k_T^2)}{\sqrt{4k_T'^4 + k_T^4}} \right] \tag{2.8}$$

where $\vec{k_T}$ is the transverse momentum of the emitted gluon and $f(x,k_T^2)$ represents the unintegrated gluon density which can be related to the standard gluon density by

$$xg(x,Q^2) = \int_0^{Q^2} \frac{\mathrm{d}k_T^2}{k_T^2} f(x,k_T^2). \tag{2.9}$$

Equation (2.8) can be solved analytically for fixed α_S. The result in the saddle point approximation [32] is then

$$\frac{f(x,k_T^2)}{\sqrt{k_T^2}} \propto \left(\frac{x}{x_0}\right)^{-\lambda}, \qquad \lambda = \frac{\alpha_S N_C}{\pi} 4\ln 2 \tag{2.10}$$

where x_0 is the initial Bjorken-x and N_C is the number of colors. As can be seen, the gluon density is expected to rise with a power of $\frac{1}{x}$ for decreasing x, i.e. $xg(x,Q^2) \propto x^{-\lambda}$.

The BFKL equation thus represents an evolution in x which plays a key role in the evolution of the $q\bar{q}$ pair within the color dipole picture which will be described in the following section.

2.3 Parton saturation and the Color Glass Condensate

The evolution of a parton density with increasing energy has already been introduced in the previous section. Let us recall the situation in which the increase of the number of partons with the "same" size is observed with decreasing x. This behaviour could lead to divergent cross sections which are however not observed in experimental measurements, the cross section is observed to be finite. The key to the explanation of this phenomenon lies in the saturation of parton densities. At sufficiently low-x values, the phase space of the hadron is completely filled with the created partons and therefore the emergence of other new partons is not energetically favourable. Wave functions of partons start to overlap leading to their recombination. The recombination naturally opens the phase space for new partons to emerge. This delicate balance occurs along the saturation scale which separates the dilute and saturated (dense) regime as depicted in Figure 2.2. The saturation scale in general depends on both Bjorken-x and the scale Q^2, because due to the evolution with increasing scale the saturation region is reached at even lower x of the newly emerging partons.

The Color Glass Condensate (CGC) is an effective field theory which aims to approximate QCD in the saturation regime at which the hadron represents a very densely packed medium filled with interacting gluons. The name of the model is closely related to the state it describes and its properties. "Color" stands for the fact that the medium is composed of particles with color charge, "Glass" refers to the slow evolution of the system and the term "Condensate" is related to the filled phase space of the hadron. For a review of the main aspects of the Color Glass Condensate see references [24, 33].

Within the CGC framework, gluon densities at high energies are assumed to be very large and thus they correspond to strong classical color fields. The evolution of these fields with increasing energy can be obtained by including quantum corrections to the classical fields, which are calculated via non-linear evolution equations such as the JIMWLK or the Balitsky-Kovchegov equation.

The CGC model represents a useful tool to describe the QCD evolution of the early stages of ultra-relativistic heavy-ion collisions [34]. The relativistic hydrodynamic description of the spacetime evolution of the created QGP medium depends on the initial conditions of the collision. As the fast nuclei can be viewed as dense CGC states filled with interacting gluons, the initial conditions could be obtained possible from the CGC framework.

2.3.1 JIMWLK equation

The Jalilian-Marian–Iancu–McLerran–Weigert–Leonidov–Kovner (JIMWLK) equation [35, 36, 37, 38] gives the evolution in Bjorken-x (or in rapidity Y) of the probability distribution of the Wilson lines $W_Y[V]$ [8]. The idea behind the JIMWLK equation derivation is to separate partons into two groups - those with large x and those with small x. Large-x partons serve as a classical source for the small-x partons. With the evolution in rapidity Y (or with decreasing x) partons become those with large x and are incorporated among other previous classical sources. Therefore, the JIMWLK evolution includes the successive emission of classical gluon fields which with decreasing-x become further sources of "new" gluon fields. It represents a non-linear modification to the BFKL equation by accounting for the recombination of gluons. I will introduce the JIMWLK equation only briefly in the following text. The full derivation using the light-cone quantum field theory approach can be seen for example in [14] or in [39]. The equation reads

$$\begin{aligned}\frac{\partial W_Y[\alpha]}{\partial Y} = \frac{\alpha_S}{2} \int \mathrm{d}^2 x_T \mathrm{d}^2 y_T \frac{\delta^2}{\delta\alpha^a(x^-, \vec{x}_T)\delta\alpha^b(y^-, \vec{y}_T)} \left(\eta^{ab}_{\vec{x}_T\vec{y}_T} W_Y[\alpha]\right) \\ -\alpha_S \int \mathrm{d}^2 x_T \frac{\delta}{\alpha^a(x^-, \vec{x}_T)} \left(\nu^a_{\vec{x}_T} W_Y[\alpha]\right).\end{aligned} \tag{2.11}$$

Light-cone fields $\alpha(x^-, \vec{x_T}) \equiv A^+(x^+ = 0, x^-, \vec{x_T})$ are related to the fundamental Wilson line which defines the propagator of an eikonal quark moving along the light-cone x^-–axis as follows:

$$V_{\vec{x}_T} = \mathrm{P}\exp\left[\frac{ig}{2}\int_{-\infty}^{\infty} \mathrm{d}x^- t^a \alpha^a(x^-, \vec{x}_T)\right] \tag{2.12}$$

where P represents the path ordering and t^a are the SU(N_C) generators in the fundamental representation. Similarly the eikonal antiquark propagator can be derived as a hermitean conjugate to (2.12).

The renormalization group procedure developed by the authors of the JIMWLK equation allows one to resum leading logarithmic contributions to the gluon distribution functions, which corresponds to the resummation of multiple pomeron exchanges. At the lowest level, i.e. for one pomeron exchange, the equation reduces to the BFKL equation. [40]

Due to its complexity there exists no analytical solution to the JIMWLK equation. Its solution have been though obtained numerically, using the lattice discretization of transverse coordinate space [41].

2.3.2 Balitsky–Kovchegov evolution equation

The Balitsky–Kovchegov (BK) equation gives the evolution with rapidity $Y = \ln\left(\frac{1}{x}\right)$ of the $q\bar{q}$ dipole scattering amplitude $N(r, Y)$. It can be obtained from the JIMWLK evolution equation presented in the previous section in the limit of large number of colors $N_C \gg 1$, see e.g. [14]. The BK evolution equation was originally derived using two different approaches which has resulted in the "same" nonlinear evolution equation.

Balitsky [42] based his approach on the BFKL evolution equation (2.8). As already mentioned, the BFKL equation violates the unitarity of the scattering amplitude at high energies. Therefore, Balitsky proposed a gauge-invariant operator expansion for high-energy amplitudes with the relevant operators being gauge factors ordered along light-like lines, i.e. Wilson-line operators. The BFKL equation can then be seen as an evolution equation for these operators, with respect to the slope of the line, and its gauge-invariant generalization performed by Balitsky turns out to be a nonlinear evolution equation of parton densities.

On the other hand Kovchegov, similarly as the authors of the JIMWLK equation, based his approach on Mueller's dipole model [43, 44]. In his work [40], Kovchegov resummed all multiple-pomeron exchanges in DIS contributing to the structure function F_2 of the target hadron in the leading logarithmic approximation in the large N_C limit, resulting in an evolution equation for the dipole scattering amplitude N.

The impact-parameter independent Balitsky–Kovchegov equation in its most common form reads as

$$\frac{\partial N(r,Y)}{\partial Y} = \int \mathrm{d}^2 r_1 K(r,r_1,r_2) \left[N(r_1,Y) + N(r_2,Y) - N(r,Y) - N(r_1,Y)N(r_2,Y)\right] \tag{2.13}$$

where $r \equiv |\vec{r}|$ is the transverse size of the dipole and $K(r,r_1,r_2)$ represents the kernel of the above stated integro-differential equation.

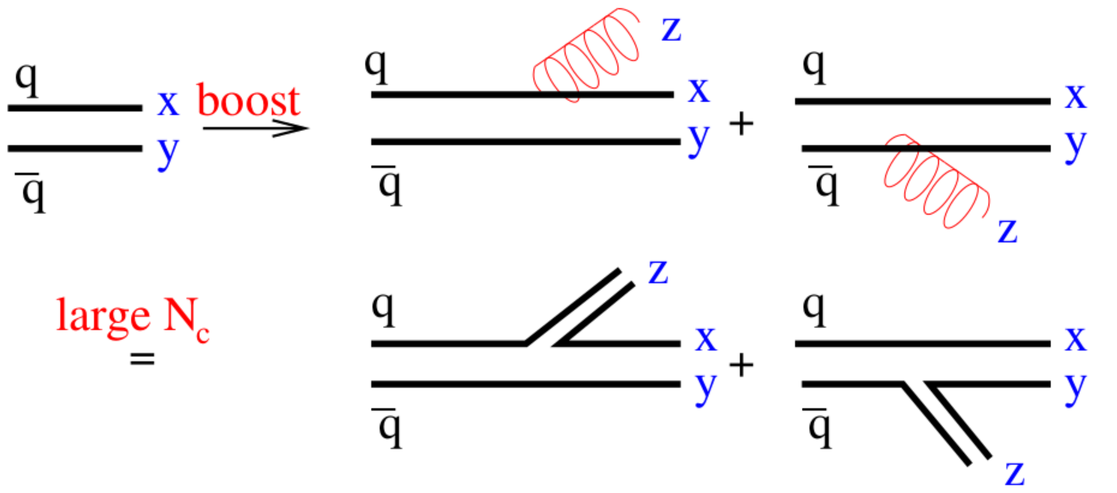

Figure 2.4: Diagrams for the gluon emission in the color dipole evolution and its large N_C limit. [45]

The interpretation of the Balitsky–Kovchegov equation can be made as follows and its graphical illustration can be seen in Figure 2.4. The parent dipole with transverse size $\vec{r} = \vec{x} - \vec{y}$, where $\vec{x}$ and $\vec{y}$ denote locations of the ends of the dipole, emits a gluon with position $\vec{z}$ when evolved in rapidity. The gluon emission is described by the BFKL evolution equation (2.8). In the large-N_C limit the gluon can be approximated as another $q\bar{q}$ pair and the situation corresponds to the emergence of two new dipoles with transverse sizes $\vec{r}_1 = \vec{x} - \vec{z}$ and $\vec{r}_2 = \vec{y} - \vec{z}$. The probability is described by the first three linear terms in eq. (2.13), where the amplitudes $N(r_1,Y)$ and $N(r_2,Y)$ correspond to the two daughter dipoles and the amplitude $N(r,Y)$ correspond to the original dipole. The last non-linear term in (2.13) corresponds to the recombination of the newly formed $q\bar{q}$ pair and ensures unitarity of the scattering amplitude in the local transverse configuration space, i.e. $N(r,Y) \in [0,1]$. The comparison of the solution N of (2.13) with the situation when the non-linear term is omitted resulting in the unitarity violation is depicted in Figure 2.5.

Similarly as for the JIMWLK equation, the Balitsky–Kovchegov equation does not have an analytical solution and has to be solved numerically. Studies of the numerical solution to the BK equation and its properties according to the choice of the initial conditions and the kernel of the equation (2.13) were performed e.g. in [15, 45, 46] and some of them will be presented in the following chapters.

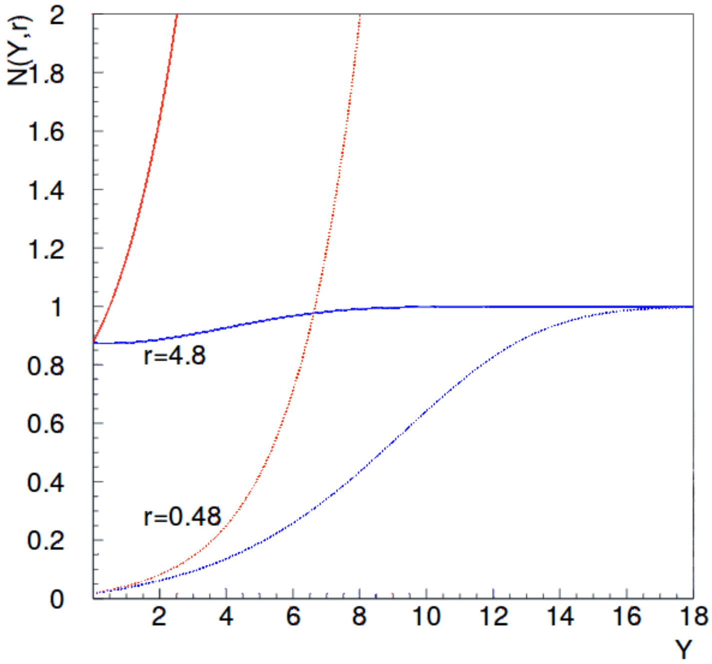

Figure 2.5: Comparison of the BK equation (2.13) solution (blue lines) to the BK equation solution without nonlinear term (red lines), which corresponds to the BFKL equation (2.8) solution for N, for two various transverse sizes r of the dipole. [47]

2.3.2.1 Choice of the kernel

The kernel of the integro-differential equation (2.13) in general causes a change in the width of the fluctuation into $q\bar{q}$ pair. It has an interpretation as the probability of gluon emission which is then weighted by the difference of daugher dipoles and parental dipole scattering probabilities. There are several prescriptions for the kernel of the Balitsky-Kovchegov equation, the ones which are most important for this work are presented in the following text.

The BFKL kernel for the BK equation derived at leading order in $\alpha_S\left(\frac{s}{s_0}\right)$ has the form [45]

$$K_{\text{BFKL}}(r, r_1, r_2) = \frac{\alpha_S N_C}{2\pi^2}\frac{r^2}{r_1^2 r_2^2}. \tag{2.14}$$

The strong coupling constant α_S is kept at a fixed value in this prescription and the kernel is conformally invariant. There is no divergence for $r_1, r_2 \to 0$ provided $N(r, Y) \sim r^a$ for $r \to 0$ and $a > 0$ [45].

The prescription (2.14) can also be modified to include the running coupling by the choice $\alpha_S \to \alpha_S(r^2)$ and therefore the BK equation includes also corrections of higher order. The strong coupling constant α_S [48] is no longer fixed and it depends on the size of the parent dipole r as

$$\alpha_{S,n_f}(r^2) = \frac{4\pi}{\beta_{0,n_f}\ln\left(\frac{4C^2}{r^2\Lambda_{n_f}}\right)} \tag{2.15}$$

where the constant C is the uncertainty inherent to the Fourier transform from momentum to the position space and is usually obtained from a fit to data. The parameter Λ_{n_f} is the QCD scaling parameter and can also be obtained from a fit or it can be calculated from the experimentally measured value of α_S as it, in general, depends on the number of active flavours n_f. The later approach will be described in Chapter 2.3.2.3. The parameter β_{0,n_f} is defined at the one loop approximation of the running coupling as

$$\beta_{0,n_f} = 11 - \frac{2}{3}n_f. \tag{2.16}$$

A more recent form of the kernel to the running coupling BK (rcBK) equation was derived by Balitsky [49] and is given by

$$K_{\mathrm{Bal}}(r, r_1, r_2) = \frac{\alpha_S(r^2)N_C}{2\pi^2}\left[\frac{r^2}{r_1^2 r_2^2} + \frac{1}{r_1^2}\left(\frac{\alpha_S(r_1^2)}{\alpha_S(r_2^2)} - 1\right) + \frac{1}{r_2^2}\left(\frac{\alpha_S(r_2^2)}{\alpha_S(r_1^2)} - 1\right)\right] \tag{2.17}$$

The Balitsky prescription is usually preferred since it gives slower evolution speed consistent with the experimental data of physical observables [11].

2.3.2.2 Initial conditions

The initial condition for the differential equation (2.13) at which the evolution in rapidity Y starts is needed for its numerical solution. There are again several choices of initial conditions and its parameters which we briefly introduce in the following text. One of the typical and frequently used initial form of the scattering amplitude comes from the Golec-Biernat–Wusthoff model [13] and has the form [15, 45]

$$N(r, Y = 0) = 1 - \exp\left[-\frac{(r^2 Q_{s_0}^2)^\gamma}{4}\right]. \tag{2.18}$$

Another widely used initial form of the scattering amplitude comes from the McLerran–Venugopalan model [50] and has the following form [15, 46]

$$N(r, Y = 0) = 1 - \exp\left[-\frac{(r^2 Q_{s_0}^2)^\gamma}{4}\ln\left(\frac{1}{r\Lambda} + e\right)\right]. \tag{2.19}$$

Both initial conditions (2.18) and (2.19) depend on several parameters which can usually be obtained from a fit to data. The parameter $Q_{s_0}^2$ is the saturation scale for the largest x which is considered in the computation. The anomalous dimension γ controls the slope of the dipole amplitude with respect to decreasing dipole size r. Note that e in (2.19) is the Euler's number and not the elementary charge as one could guess. The parameter Λ in (2.19) represents an infrared cutoff of the dipole-nucleon cross section at the level of two gluon exchange or in the semiclassical limit [15]. In general, it does not have to be identical with the scaling parameter Λ_{n_f} which will be introduced in the following chapter. However Λ is often set as Λ_3 from (2.21) or it can be obtained from a fit [15].

2.3.2.3 Variable number of flavours scheme

As already mentioned in the previous section, the scaling parameter Λ_{n_f} in general depends on the number of flavours active in the interaction and can be obtained from the experimentally measured value of α_S using the reciprocal prescription [15].

For $n_f = 3$ only light quarks contribute to the interaction. However fluctuations of the virtual photon wave function (1.27) and (1.28) into dipoles consisting of a heavy flavour quark-antiquark pair are also allowed. Such contribution should be accounted for in the calculation of the running coupling (2.15).

The value of n_f is chosen as number of quark flavours lighter than the momentum scale $\mu^2 = \frac{4C^2}{m_f}$ associated with the scale r^2 at which the running coupling is evaluated. Branches of the coupling with adjacent n_f are matched at the scale corresponding to the quark masses $r_*^2 = \frac{4C^2}{m_f^2}$. At one-loop accuracy of (2.15) and (2.16) at which the BK equation with kernel (2.17) is computed the matching is done according to

$$\alpha_{S,n_{f-1}}(r_*^2) = \alpha_{S,n_f}(r_*^2). \tag{2.20}$$

which results in the reciprocal relation for Λ_{n_f} determination

$$\Lambda_{n_{f-1}} = \left(m_f\right)^{1-\frac{\beta_{0,n_f}}{\beta_{0,n_{f-1}}}} \left(\Lambda_{n_f}\right)^{\frac{\beta_{0,n_f}}{\beta_{0,n_{f-1}}}} \tag{2.21}$$

Values of Λ_{n_f} are determined from Λ_5 which is determined from the experimentally measured value of α_S at the Z^0 mass as

$$\Lambda_5 = M_Z \exp\left(-\frac{2\pi}{\alpha_S(M_Z)\beta_5}\right). \tag{2.22}$$

By the term heavy quarks it is usually meant that charm and beauty quarks contribute, the top quark dipoles are not considered due to the large mass of t quark. For only light quarks contribution one has the choice in the approach to obtain the Λ_3 parameter value. It can be either calculated using the mentioned scheme (2.21) or eventually it can be determined from a fit.

Also it is important to note that α_S is artificially frozen at the certain constant value for dipole sizes larger than the scale at which the running coupling constant reaches the given value according to

$$r_{SAT}^2 = \frac{4C^2}{\Lambda_{n_f}^2 \exp\left(\frac{4\pi}{\beta_{0,n_f}\alpha_{S,\mathrm{fix}}}\right)} \tag{2.23}$$

where $\alpha_{S,\mathrm{fix}}$ is the value of the frozen running coupling, e.g. $\alpha_S = 0.7$. The value of n_f in (2.23) is taken according to appropriate region of r^2 at which the coupling is fixed. This cutoff is due to the fact that also very large dipoles are included in the calculation of the BK equation. These dipoles correspond to emission of gluons with arbitrarily small transverse momenta and therefore the running coupling has to be regulated in the infrared region.

Chapter 3

Dipole cross sections

In this chapter, I study the dipole-proton amplitude under the asumption that the dependence on impact parameter b and on energy can be factorized. Then I foucus on the energy dependent part within the BK equation to study how changes in the solution method affect the resulting amplitude. In particular, I study different kernels, Runge-Kutta methods, and prescriptions to compute the running coupling α_S. In the last part of this chapter I describe a model for the b-dependent part of the amplitude.

3.1 Factorized dipole-proton amplitude

Let us recall the relation (1.30) for the total cross section of the $q\bar{q}$ dipole scatterred off the proton in DIS. Under some assumptions (see Chapter 1.2) we obtained the cross section $\sigma_{q\bar{q}}$ determined only by the parameter σ_0 and the dipole scattering amplitude $N(x,r)$, the impact parameter b dependence being trivial. However, for the description of the production of vector meson states one has to include the dependence of the cross section on the proton structure.

The impact parameter b dependence of the dipole cross section is therefore non-trivial in this case. One of the possible approaches is to include it into the proton profile function $T_p(b)$, which parametrizes the transverse distribution of the proton. This factorization has already been used e.g. in [51]. We will make use of this approach in our calculations of the J/ψ photoproduction cross-sections in Chapter 5. The differential dipole-proton cross section in (1.39) can be then written as

$$\frac{\mathrm{d}\sigma_{q\bar{q}}}{\mathrm{d}^2b} = 2N(x,r,b) = \sigma_0 N(x,r)T_p(b) \tag{3.1}$$

and from the normalization condition

$$\int \mathrm{d}^2b T_p(b) = 1 \tag{3.2}$$

one can obtain the total dipole cross section as defined in Chapter 1.2

$$\sigma_{q\bar{q}} = \int \mathrm{d}^2b \sigma_0 N(x,r)T_p(b) = \sigma_0 N(x,r) \tag{3.3}$$

where the parameter σ_0 is obtained from a fit to data, either as one of the free fit parameters or it can be estimated using the parameter B, which is fixed by the average squared transverse

	B_0 [GeV^{-2}]	α' [GeV^{-2}]	W_0 [GeV]
$Q^2 \lesssim 1$ GeV^2	4.603	0.164	90
$Q^2 = 2 - 80$ GeV^2	3.860	0.019	90

Table 3.1: Parameters to the relation (3.4) for W-dependent value of B. [52].

radius of the proton [15] and under the assumption that the normalisation condition (3.2) does not hold.

In general the value of B should depend on W and is different for each dipole cross section parametrisation. This dependence was measured at HERA [52] leading to a formula

$$B(W) = B_0 + 4\alpha' \ln\left(\frac{W}{W_0}\right) \tag{3.4}$$

where B_0, W_0 and α' are parameters obtained from a fit to data for various kinematic regions in dependence on the scale Q^2 and they are listed in Tab. 3.1.

3.2 Solution to the Balitsky–Kovchegov equation

In this section we present the approach to the numerical solution of the Balitsky-Kovchegov evolution equation (2.13) defined in Chapter 2.3.2. The evolution in rapidity is performed by the Runge-Kutta methods introduced in Appendix A. The specific form of each method with respect to the eq. (2.13) is stated in Appendix B. Evolution proceeds with the step in rapidity $\Delta Y = 0.05$. All the integrals stated in Appendix B are calculated using the Simpson's rule (A.17) defined in Appendix A.

Since the composite Simpson's rule works on the grid spaced uniformly between the integration limits we define a logarithmic grid in r spaced uniformly from minimum $r_{min} = 10^{-7}$ GeV^{-1} to maximum $r_{max} = 10^2$ GeV^{-1} value of r. Note that by r we mean a size of the vector $\vec{r}$ which determines the transverse size of the dipole. The integral on the right-hand side of equation (2.13) depends on the size of $\vec{r}_1$ and therefore for every r it has to be evaluated separately for each value of r_1. Because we work with polar coordinates, the value of r_2 can be obtained in each loop over r_1 according to

$$r_2 = \sqrt{r^2 + r_1^2 - 2rr_1\cos(\varphi)} \tag{3.5}$$

where φ represents the angle between $\vec{r}$ and $\vec{r}_1$. One can thus rewrite the differential $\mathrm{d}^2 r_1$ in eq. (2.13) as $r_1 \mathrm{d}r_1 \mathrm{d}\varphi$ and therefore for every r_1 it is neccessary to calculate the integral over the angle φ between the limits $[0, 2\pi]$. Or alternatively, due to the fact that cosine is an even function, one can calculate the definite integral on the interval $[0, \pi]$ and multiply the result by a factor 2. And of course, one has to include the Jacobian coming from the logarithmic spacing of the grid in r.

In the case that the point r_2 does not match one of the set grid points at which the initial condition and every following step in rapidity evolution have been computed, it is necessary to

	Initial condition	α_S cut-off	Q^2_{s0} [GeV^2]	γ [−]	C [−]	σ_0 [mb]
a	GBW, with light quarks	0.7	0.241	0.971	2.460	32.357
b	MV, with light quarks	0.7	0.165	1.135	2.520	32.895
c	MV, with heavy quarks	0.7	0.165	1.099	3.813	18.740

Table 3.2: Parameters used for the solution of the Balitsky–Kovchegov equation for different initial conditions according to fits from [15].

interpolate the value of $N(r_2, Y)$ at this point. A Lagrange interpolation of the 1st order, i.e. the linear interpolation (A.11) defined in Appendix A is used for this purpose.

It is also necessary to point out that for the same values of $\vec{r}$ and $\vec{r}_1$ eq. (3.5) results in $r_2 = 0$. Such points have to be excluded from the calculation because $r_2 = 0$ results into a divergent kernel $K(r, r_1, r_2)$ and therefore the whole integral with the approximate solution given by the sum (A.17) diverges.

Parameters used for the solution to the BK equation (2.13) according to the choice of initial condition, flavour contribution and fixed or running coupling are listed in Table 3.2. We set the infrared cutoff on the running coupling as $\alpha_{S,cutoff} = 0.7$. The parameter Λ in the MV initial condition (2.19) is set as $\Lambda = 0.241$ GeV or we opt to set it to Λ_{n_f}, the particular choice will be specified in the following sections.

3.2.1 Choice of the kernel and the initial condition

In the following section we present a study of the Balitsky-Kovchegov evolution equation solution $N(r, Y)$ in dependence on the choice of particular initial condition and kernel of the integro-differential equation (2.13). For the purpose of this study we set the Λ_{n_f} parameter in running coupling (2.15) and Λ parameter in MV initial condition to the same value $\Lambda_3 = 0.143$ GeV obtained from the variable flavour scheme introduced in Chapter 2.3.2.3. The implementation of this scheme into the procedure for the solution to BK equation is discussed in Chapter 3.2.3. All the results were obtained using Classical method A.8, i.e. the Runge-Kutta method of the fourth order. The appropriate choice of the method is discussed in Chapter 3.2.2.

First we present a comparison of the solution to the BK equation using the BFKL kernel (2.14) with the coupling constant fixed at $\alpha_S = 0.7$ and the same kernel using the running coupling α_S given by the relation (2.15). The solution is obtained from the GBW initial condition (2.18) with parameters set from Table 3.2) set (a). As can be seen in Figure 3.1 the evolution is much faster for fixed coupling than for running coupling, as already proven in previous studies [13, 53, 54]. The slower evolution of the $N(r, Y)$ due to the running coupling is caused by the decreasing value of α_S for smaller dipole sizes as can be seen from Figure 3.6. This solution therefore provides more appropriate description of the dipole behaviour at large rapidities since value of $\alpha_S(r^2)$ decreases.

The comparison of the two kernels - BFKL kernel (2.14) and Balitsky kernel (2.17) - defined in Chapter 2.3.2 is provided in Figures 3.2 and 3.3, for GBW initial condition with parameters given by Table 3.2 set (a) and MV initial conditions with parameters given by Table 3.2 set

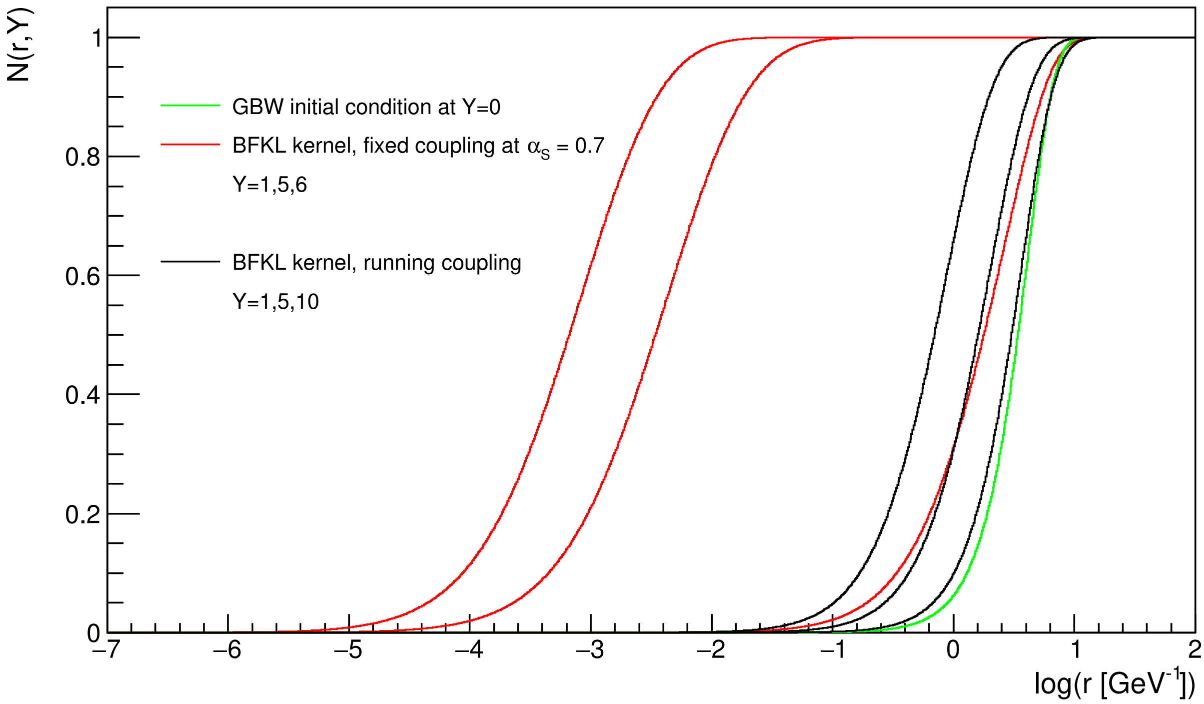

Figure 3.1: Evolution of the scattering amplitude $N(r, Y)$ of a $q\bar{q}$ dipole with a hadronic target for the GBW model initial condition (2.18) with the BFKL kernel (2.14) with the fixed coupling $\alpha_S = 0.7$ and with the running coupling α_S (2.15).

(b), respectively. The results for various rapidities indeed confirm the statement that Balitsky kernal 2.17 provides slower evolution speed which is in better accordance with experimental data according to [11]. Comparing the two figures we also conclude that this behaviour is independent on the choice of the initial condition.

In Figure 3.4 we compare the effect which may come from the choice of the GBW or the MV initial condition with the same parameters from Table 3.2 as in the previous case. As can be seen, the initial conditions slightly differ which is more or less apparent when the evolution to small rapidities Y is performed. However at higher rapidities the solution $N(r, Y)$ no longer depends on the specific choice of initial condition, exhibiting a so-called *geometric scaling* phenomenon [55]. After several units of rapidity the shape of the initial condition is "forgotten" and the solution $N(r, Y)$ propagates independently on the original prescription at $Y = 0$. This phenomenon in solution to the BK equation was studied in more detail in [56].

In conclusion we observed that the running coupling prescription is necessary for the appropriate description of the behavior of dipole cross section using the Balitsky-Kovchegov equation. In accordance with previous studies [11, 15, 45, 46] we choose to use the Balitsky prescription for the BK equation kernel and perform the evolution from MV initial condition in following studies.

3.2.2 Comparison of different Runge-Kutta methods applied to the BK equation

In this section we present the result of the rapidity evolution of the dipole scattering amplitude $N(r,Y)$ and compare the solutions to the BK equation according to the choice of one of the Runge-Kutta methods described in Appendix A and specified for the BK equation in Appendix B. For the purpose of this comparison we have chosen to solve the equation (2.13) using the McLerran-Venugopalan initial condition (2.19) with parameters set according to Table 3.2 row (c) and with $\Lambda = 0.241$ GeV set as was used in the paper [46]. The running coupling constant was calculated under the assumption that only light quarks contribute thus we set $n_f = 3$.

As can be seen in Figure 3.5 at small dipole sizes r the system is in dilute regime and $N(r,Y) \sim r^2$. With increasing r signs of saturation become apparent and for large dipole sizes r the scattering amplitude reaches its maximum value $N(r,Y) = 1$ which results from the unitarity constraints. With increasing rapidity Y the saturation phenomenom becomes more apparent even for small dipole sizes.

In the same figure the comparison is given for the solution of BK eq. using Runge-Kutta methods of the 1$^{\text{st}}$ order - Euler method (denoted as RK1), 2$^{\text{nd}}$ order - Heun's method and 4$^{\text{th}}$ order - Classical method. Minor difference between the Euler method and Classical method can be observed at highest available rapidity $Y = 100$ to which the evolution was performed.

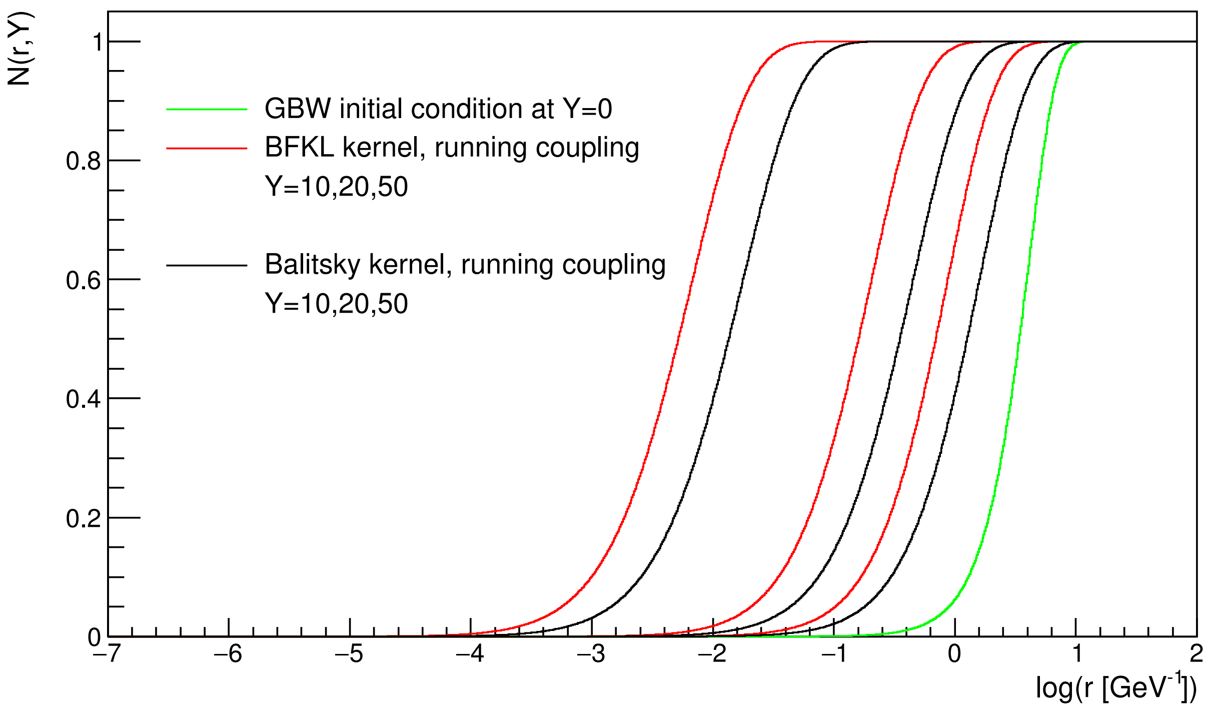

Figure 3.2: Evolution of the scattering amplitude $N(r,Y)$ of a $q\bar{q}$ dipole with a hadronic target for the GBW model initial condition (2.18) with the running coupling α_S (2.15) for the BFKL kernel (2.14) and for the Balitsky kernel (2.17).

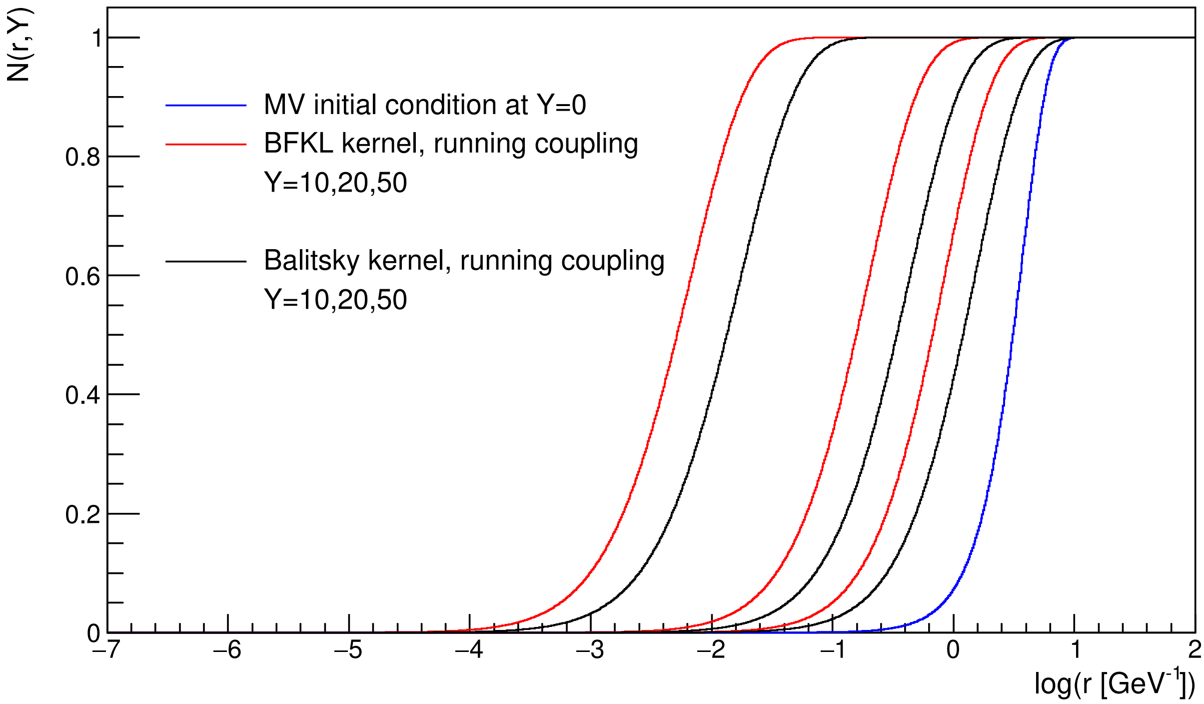

Figure 3.3: Evolution of the scattering amplitude $N(r,Y)$ of a $q\bar{q}$ dipole with a hadronic target for the MV model initial condition (2.19) with the running coupling α_S (2.15) for the BFKL kernel (2.14) and for the Balitsky kernel (2.17).

At lower rapidities the difference is almost invisible. Also there is no observable difference between the Heun's method and Classical method even at high rapidities. It is therefore apparent that the choice of specific numerical RK method has no significant influence on the behavior and resulting values of the solution $N(r,Y)$ to Balitsky-Kovchegov equation. However in the following I will restrict myself to the Classical method due to its higher precision.

3.2.3 Variable scale scheme

In conclusion of our studies of the dependence of the Balitsky-Kovchegov evolution equation solution on the specific choice of initial condition, method, parameters and other conditions we present a comparison of the solution dependence on the choice of the number of active flavours n_f. The comparison is made for the choice of parameters from row (c) of Table 3.2 and the solution to the Balitsky–Kovchegov equation is obtained with the kernel (2.17) and using the Classical Runge-Kutta method.

The running coupling $\alpha_S(r^2)$ calculated from (2.15) according to the variable number of flavours scheme introduced in Chapter 2.3.2.3 can be seen in Figure 3.6. The values of quark masses, β and Λ_{n_f} parameters are listed in Table 3.3. The values of Λ_{n_f} are determined according to relation (2.21) from the experimentally measured values of the strong coupling constant

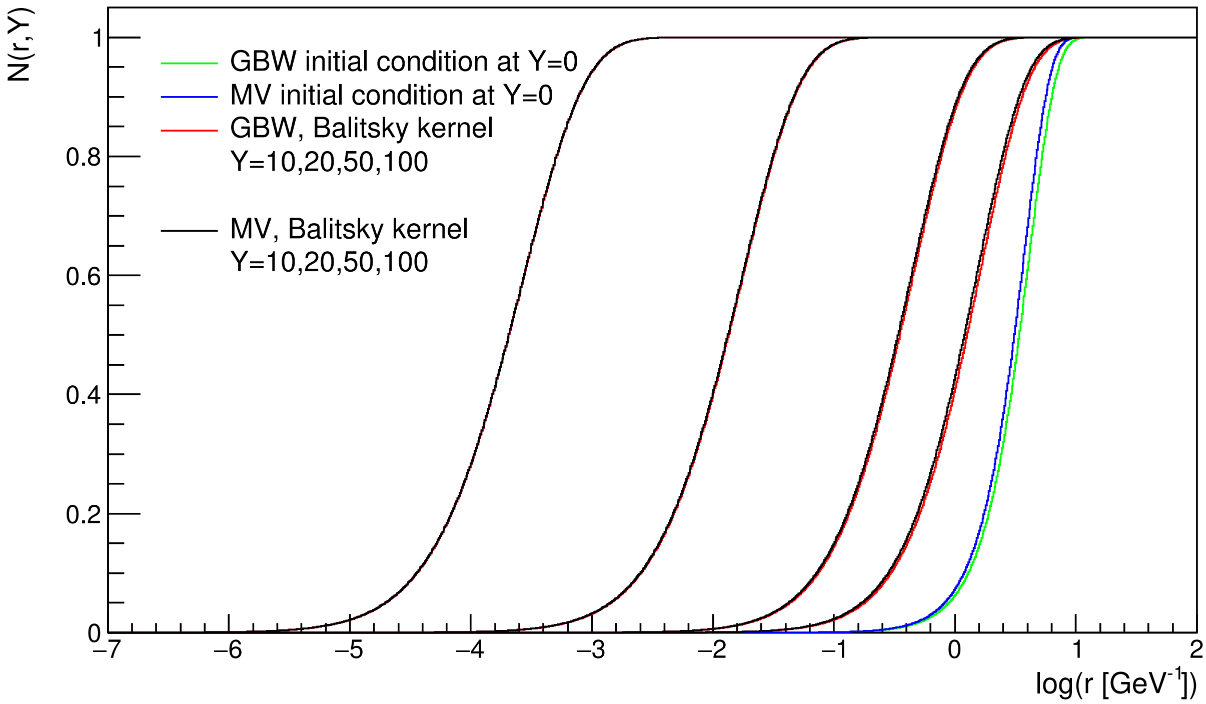

Figure 3.4: Evolution of the scattering amplitude $N(r, Y)$ of a $q\bar{q}$ dipole with a hadronic target for the MV model initial condition (2.19) and the GBW model initial condition (2.18) with the running coupling α_S (2.15) for the Balitsky kernel (2.17).

$\alpha_S(M_Z) = 0.118$ at the Z^0 mass $M_Z = 91.187$ GeV [57]. The comparison is made with the running coupling $\alpha_S(r^2)$ calculated with $\Lambda = 0.241$ GeV, set according to [46]. The running coupling is fixed at the value 0.7 for the saturation value of the dipole size according to (2.23).

Significant influence on the running coupling values can be seen between the choice of Λ parameter fixed and $\Lambda \equiv \Lambda_{n_f}$ obtained from the variable flavour scheme. The variable scheme results in the infrared cutoff of α_S at higher values of dipole sizes r than the calculation with fixed value of $\Lambda = 0.241$ GeV. The difference between the choice of specific flavour contribution within the variable flavour scheme is present for dipole sizes $r \lesssim 1$ GeV^{-1}.

The comparison of the number of active flavours choices in the solution of BK equation can be seen in Figure 3.7. For small rapidities up to $Y \approx 10$ there is no significant difference between the fixed scale with $n_f = 3$ and variable scale according to the number of active flavours. However with increasing Y the solutions exhibit the influence of the choice of active flavours. The heavy quarks contribution is prominent at very high rapidities at which it enhances the solution $N(r, Y)$ for very small dipole sizes.

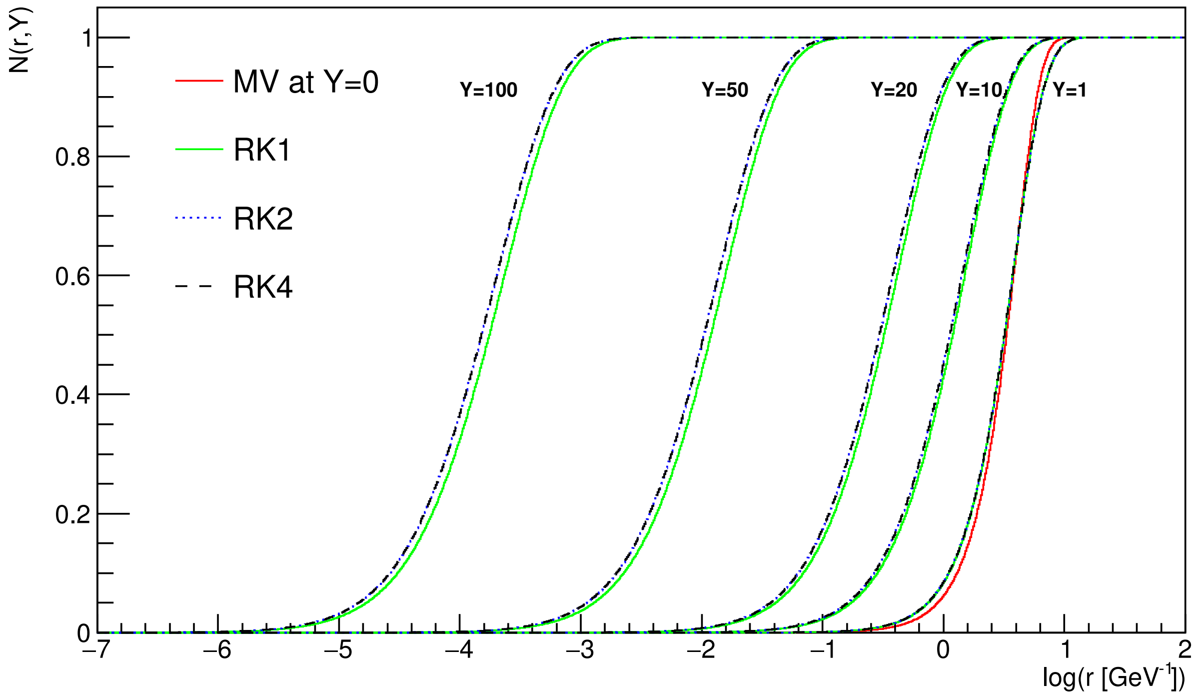

Figure 3.5: Evolution of the scattering amplitude $N(r, Y)$ of a $q\bar{q}$ dipole with a hadronic target up to rapidity $Y = 100$ for RK methods of 1st (B.4), 2nd (B.5) and 4th (B.6) order.

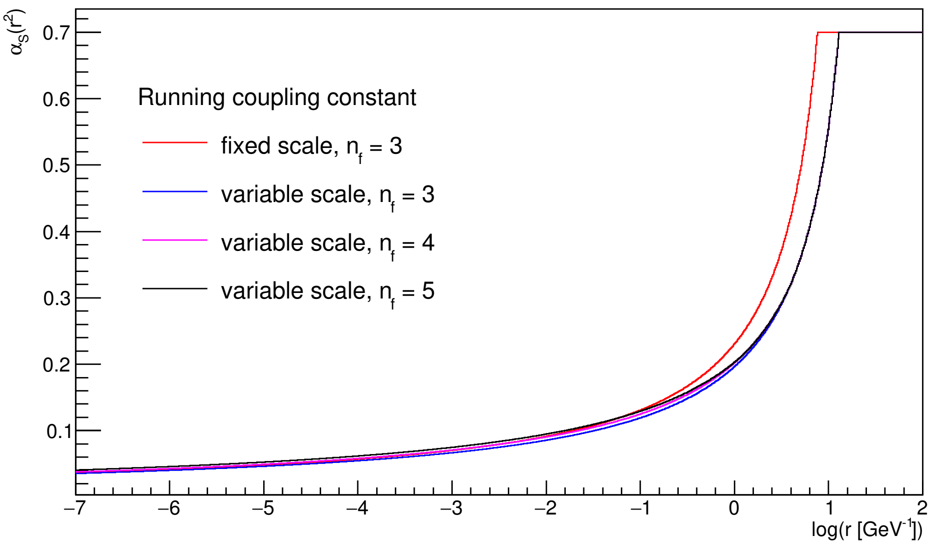

Figure 3.6: Running coupling constant α_S (2.15) depending on the number of active flavours, $\Lambda_{\text{fix}} = 0.241$ GeV, $\Lambda_3 = 0.144$ GeV, $\Lambda_4 = 0.119$ GeV and $\Lambda_5 = 0.087$ GeV.

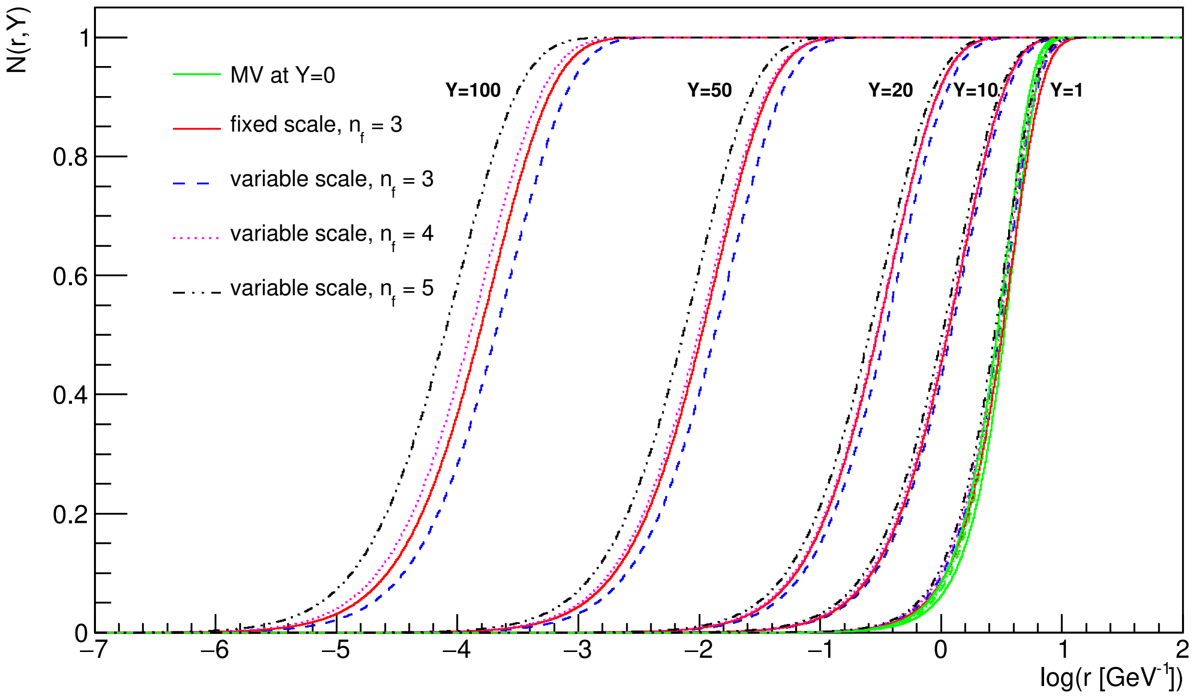

Figure 3.7: Evolution of the scattering amplitude $N(r, Y)$ of a $q\bar{q}$ dipole with a hadronic target up to the rapidity $Y = 100$ for the fixed scale with $n_f = 3$, $\Lambda_{\text{fix}} = 0.241$ GeV and the variable scale for $n_f = 3, 4, 5$, $\Lambda_3 = 0.143$ GeV, $\Lambda_4 = 0.119$ GeV and $\Lambda_5 = 0.087$ GeV.

Quark type	n_f	m_f [GeV]	β	Λ_{n_f} [GeV]
light = u,d,s	3	0.14	9.00	0.143
charm	4	1.4	8.33	0.119
beauty	5	4.18	7.67	0.087

Table 3.3: Parameters in variable flavour scheme for given quark with flavour n_f and resulting Λ_{n_f} parameters. Values of quarks masses m_f are set according to fits performed in [15].

3.3 Proton profile function

The guon density in the proton can be parametrised using various prescriptions for the proton profile function $T_p(b)$.

The simplest form of the profile function is a step function

$$T_p(b) = \frac{1}{\pi B}\theta\left(\sqrt{B} - b\right); \qquad \sigma_0 = 2\pi B \tag{3.6}$$

Another widely used form of the profile function is a Gaussian distribution

$$T_p(b) = \frac{1}{2\pi B}\exp\left(-\frac{b^2}{2B}\right); \qquad \sigma_0 = 4\pi B \tag{3.7}$$

which provides more realistic description of the proton transverse profile than the step function (3.6).

The proton profile can also be modelled based on the pion exchange model with the idea that the proton consists of a hard core given by steep Gaussian profile surrounded by a soft pion cloud given by a broad Gaussian profile, both of them being centered in the middle of the proton. The prescription reads

$$T_p(b) = \frac{1}{4\pi B_h}\exp\left(-\frac{b^2}{2B_h}\right) + \frac{1}{4\pi B_s}\exp\left(-\frac{b^2}{2B_s}\right) \tag{3.8}$$

where the values B_h and B_s have to be fitted to data.

The above described shapes of the transverse profile of the proton are compared in Figure 3.8 where the parameter B_h corresponds to the width of the steep Gaussian profile describing the hard core of the proton and the parameter B_s corresponds to the width of the broad Gaussian prodile describing the soft cloud. For demonstration purpose the values of B in step function (3.6) and Gaussian distribution (3.7) of the function $T_p(b)$ are set to $B \equiv B_s$.

3.3.1 Hot spots model

The proton profile can also be seen as a set of gluon clusters, called hot spots, whose number and position fluctuate from interaction to interaction. This approach was used to study exclusive and dissociative production of J/ψ in [58].

The proton profile can be then defined as a sum of N_{hs} of these regions of high gluonic density as

$$T_p(b) = \frac{1}{N_{hs}}\sum_{j=1}^{N_{hs}} T_g\left(\vec{b} - \vec{b}_j\right); \qquad \sigma_0 = 4\pi B \tag{3.9}$$

where each hot spot has a Gaussian distribution

$$T_g(b) = \frac{1}{2\pi B_{hs}}\exp\left(-\frac{b^2}{2B_{hs}}\right). \tag{3.10}$$

Each $\vec{b}_j$ is obtained from a 2-dimensional gaussian distribution with width B. The parameter B_{hs} can be interpreted as an average of the squared transverse radius of hot spots.

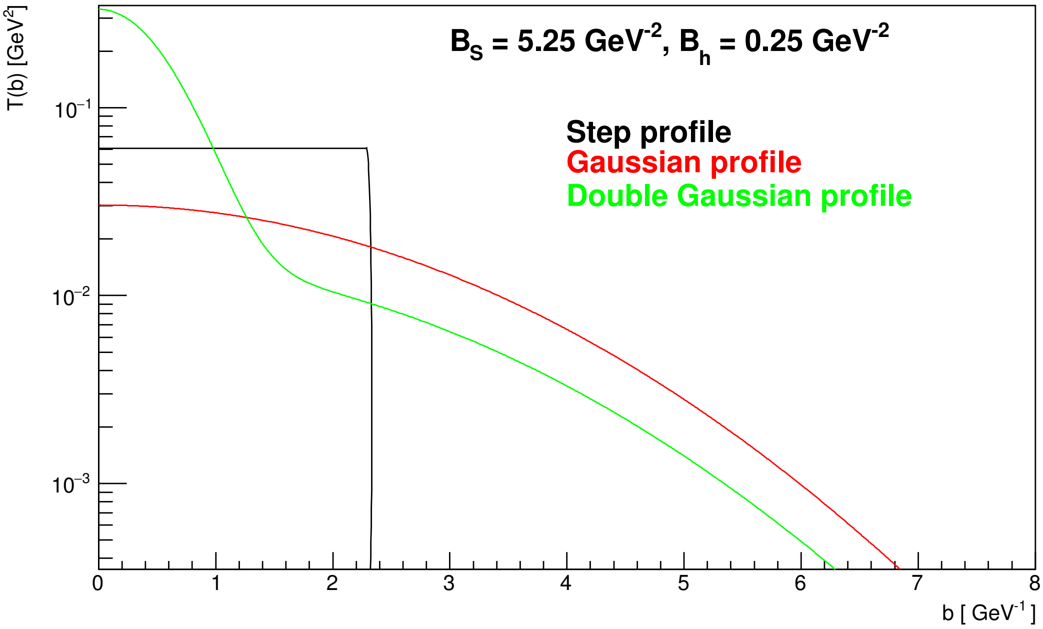

Figure 3.8: Transverse profile of the proton using various models.

p_0	p_1	p_2
0.011	-0.58	300

Table 3.4: Parameters for the x-dependents number of hot spots N_{hs} according to [58] and [59].

The number of hot spots N_{hs} can be in general dependent on x which makes the proton profile (3.9) energy dependent. We use the following prescription for N_{hs} introduced in [58]:

$$N_{hs} = p_0 x^{p_1} \left(1 + p_2 \sqrt{x}\right) \tag{3.11}$$

where p_0, p_1 and p_2 are the parameters. This prescription should follow the idea that at fixed scale the number of gluons increases with increasing energy (i.e. with decreasing x).

The implementation of this model is the following:
First one has to choose sufficiently large number N_{conf} of possible configurations. In each of them one has to calculate N_{hs} given by eq. (3.11) and get the integer value of N_{hs} as its mean value or from a zero-truncated Poisson distribution. For each hot spot one has to obtain a random value of $\vec{b}_i$. Then one has to calculate the hot spot profile (3.10) for each N_{hs} and then obtain its weighted sum (3.9) in each configuration. At the end sum over all possible configurations is calculated and weighted by N_{conf}.

Visualisation of three random configurations of the transverse structure of the proton obtained from the hot spots model are presented in Figures 3.9, 3.10 and 3.11 for three different choices of Bjorken-x in relation (3.11). As can be seen, various different configurations are allowed within the model.

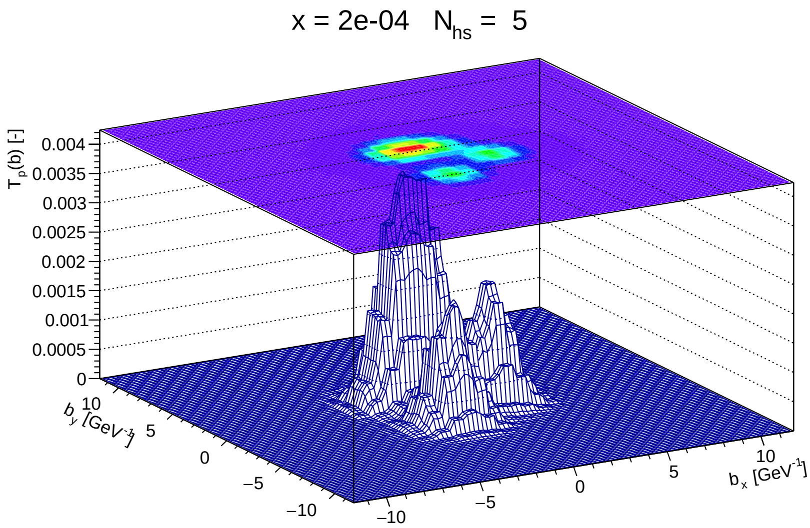

Figure 3.9: Shape of the transverse profile of the proton generated from hot spots model for $x = 2 \cdot 10^{-4}$ with $N_{hs} = 7$.

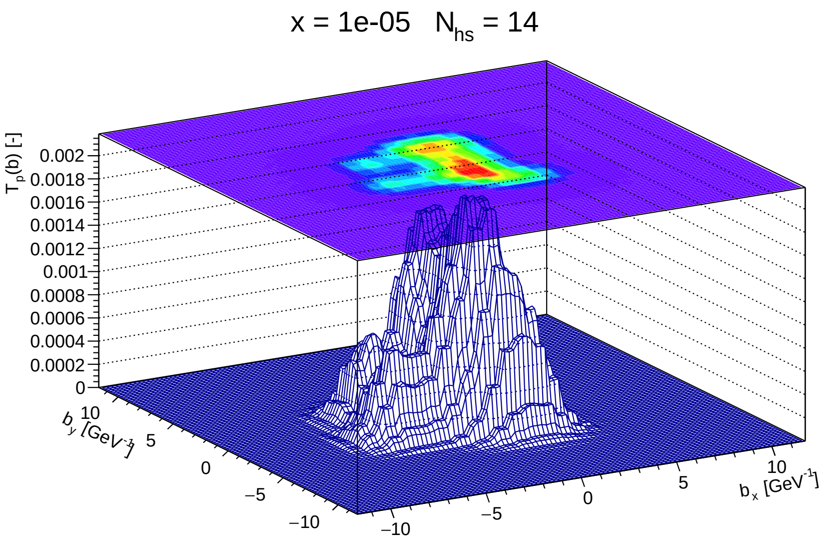

Figure 3.10: Shape of the transverse profile of the proton generated from hot spots model for $x = 1 \cdot 10^{-5}$ with $N_{hs} = 14$.

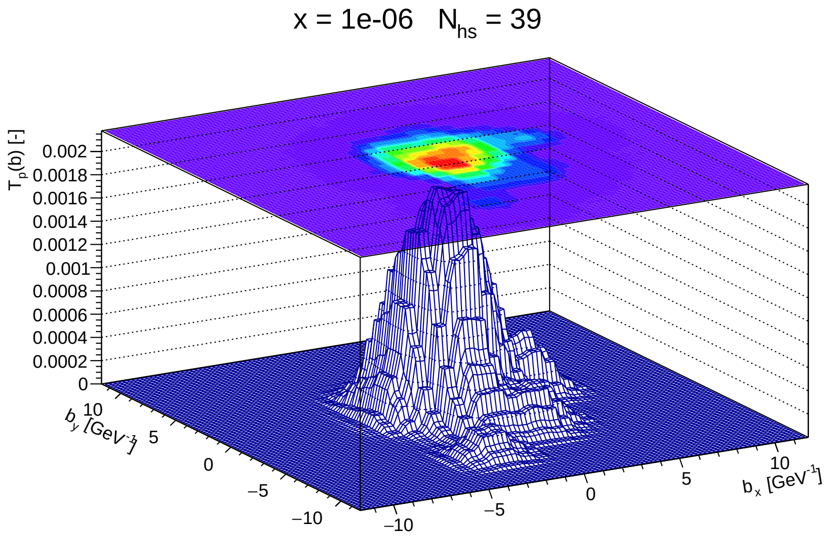

Figure 3.11: Shape of the transverse profile of the proton generated from hot spots model for $x = 1 \cdot 10^{-6}$ with $N_{hs} = 32$.

Chapter 4

Results

The main objective of this work is to study the photoproduction and electroproduction of vector mesons, namely, the study of the J/ψ meson have been chosen. In the following sections I will first present predictions for the structure function F_2 in deep inelastic scattering and compare the predictions with experimentally measured data. Then we will focus on the predictions for cross sections of J/ψ production using various approaches to the dipole cross section presented in the previous chapter. Again, we will provide the comparison of our results to the experimentally measured data.

All of the integrals in the following calculations of cross sections have been solved employing the Simpson's rule (A.17) defined in Appendix A.

4.1 Structure function F_2 in DIS

I computed the predictions for structure function F_2 (1.33) in deep inelastic scattering in order to verify our choice of parameters for the description of vector meson production. The scale $Q^2 = 2.7$ GeV^2 has been chosen since it is close to the J/ψ photoproduction scale $Q^2 = 2.4$ GeV^2 according to [58]. The predictions for the scale $Q^2 = 0.2$ GeV^2 have also been computed. The predictions are compared to HERA data combined from H1 and ZEUS experiments [9].

The comparison for $Q^2 = 2.7$ GeV^2 can be seen in Figure 4.1. Parametrizations according to set (a) and (d) in Table 4.1 will be used in further studies of vector meson production. As can be seen, these two sets of paramters describe the data reasonably well. For demonstration purposes I also compared these two predictions and data to the predictions using parameters given by set (b) and (c) from Table 4.1. These two sets of parameters were extracted from a fit performed by Golec-Biernat and Wusthoff in original publication [13], which proposed the parametrization (1.31). The predictions exhibit higher contribution to F_2 for small-x however they agree with the data reasonably well.

In the same plot we also show a prediction for F_2 using the solution $N(x, r)$ to the BK equation in the dipole cross section (1.30). The evolution of the scattering amplitude is evaluated at rapidity $Y = \ln\left(\frac{x_0}{\tilde{x}}\right)$ with $x_0 = 0.01$ [46] and $\tilde{x}$ defined as (1.26). Although the F_2 prediction obtained using BK equation exhibits the same higher contribution to F_2 at small-x we can conclude that this prediction again provides a reasonable description of the data. It is also in accordance with the other presented models, especially with the prediction from the GBW parametrization with parameters given by set (c) from Table 4.1, which include the charm quark contribution to the total DIS cross section (1.25).

	n_f	λ_{GBW}	x_0	σ_0 [mb]
a	3	0.210	$2.00 \cdot 10^{-4}$	22.998
b	3	0.288	$3.04 \cdot 10^{-4}$	23.030
c	4	0.277	$0.41 \cdot 10^{-4}$	29.120
d	4	0.287	$1.11 \cdot 10^{-4}$	23.900

Table 4.1: Parameters for the GBW parametrization (1.31) including only light quarks $n_f = 3$ and also including charm quark contribution $n_f = 4$. Light and charm quark masses were set as $m_l = 0.14$ GeV and $m_c = 1.4$ GeV, respectively.
(a) parametrization used in [58] in studies of J/ψ production using hot spots model where $\sigma_0 = 4\pi B$ with $B = 4.7$ GeV^{-2}.
(b)-(c) original GBW parametrization with only light quarks contribution and with charm constribution, respectively [13].
(d) parameters from a fit performed in [10].

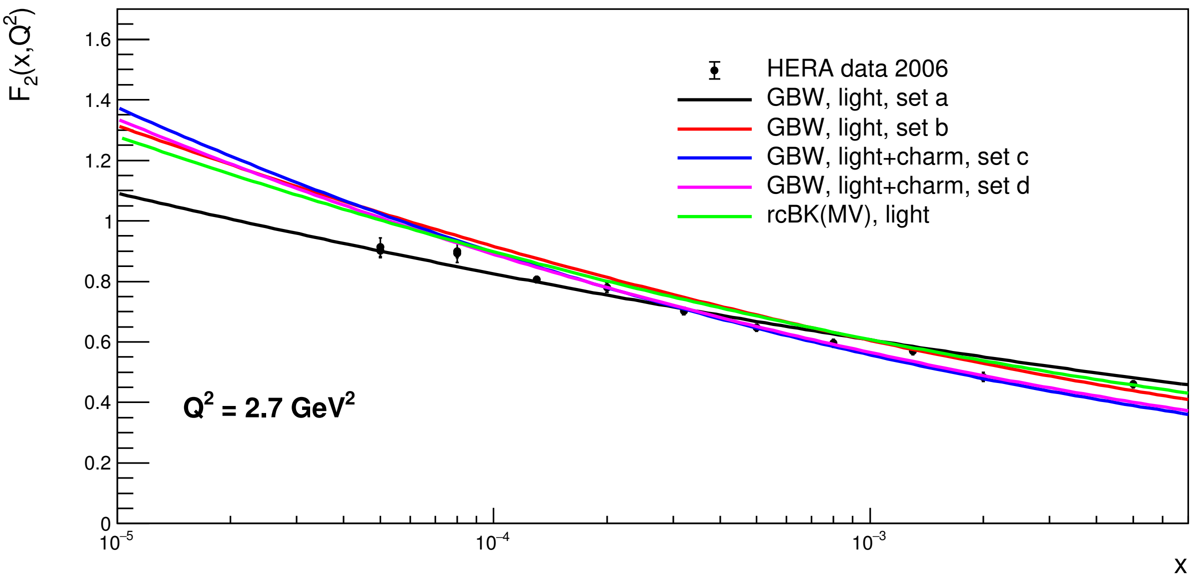

Figure 4.1: Prediction for the structure function F_2 in deep inelastic scattering for $Q^2 = 2.7$ GeV^2 using the GBW parametrization with parameters given in Table 4.1 and using the solution of the BK equation with running coupling kernel (2.17), the MV initial condition (2.19) and parameters given by set (c) in Table 3.2.

These predictions of the structure function F_2 were also computed for the scale $Q^2 = 0.2$ GeV^2 and compared to HERA data [9]. The comparison can be seen in Figure 4.2. At this scale, the GBW parametrization with parameters given by set (b) and set (d) from Table 4.1 provide good description of the H1 and ZEUS data. The GBW parametrization with parameters given by set (c) from Table 4.1 also provides good description of the data, although it slightly overestimates the data in low x. This is in accordance with the behavior of this set of parameters in the case of $Q^2 = 2.7$ GeV^2 depicted in Figure 4.1. The GBW parametrization with parameters given by set (a) from Table 4.1 provides a good desctiption of the data for $x > 10^{-5}$. However, for lower x it tends to underestimate the data which may be the result of lower λ_{GBW} parameter when compared to other sets of parameters in Table 4.1. The prediction of the structure function obtained using the solution $N(\tilde{x}, r)$ to the BK equation provide very good description of the data and it is in good accordance with models obtained from GBW parametrization with parameters given by sets (b) and (d).

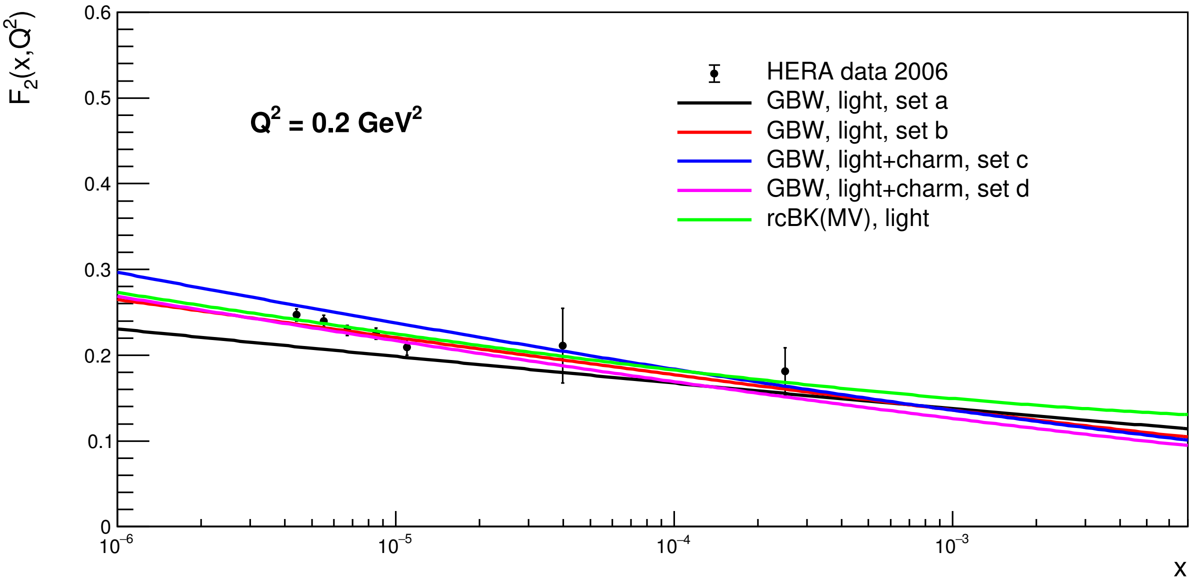

Figure 4.2: Prediction for the structure function F_2 in deep inelastic scattering for $Q^2 = 0.2$ GeV^2 using the GBW parametrization with parameters given in Table 4.1 and using the solution of the BK equation with running coupling kernel (2.17), the MV initial condition (2.19) and parameters given by set (c) in Table 3.2.

4.2 Production of J/ψ meson

I present the predictions for J/ψ photoproduction and electroproduction cross sections in this section. The cross section is obtained using the dipole cross section obtained from the GBW parametrization (1.31) or from the solution $N(x,r)$ to the Balitsky-Kovchegov equation (2.13). We will also present the prediction for the J/ψ photoproduction and electroproduction cross sections using hot-spot model introduced in Chapter 3.3.1.

4.2.1 Wave functions

In the following section we present properties of the J/ψ wave function and its overlap with the photon wave function which were defined in Chapter 1.3. Parameters for the J/ψ wave function are given in Table 4.2.

The scalar part (1.44) of the vector meson wave function obtained from the boosted Gaussian model is depicted in Figure 4.3. As can be seen, the function is symmetrical around the momentum fraction value $z = 0.5$. This model also gives similar contribution for the J/ψ meson originating from transversally and longitudinally polarized virtual photons. This is due to the similar value of N_T and N_L parameters originating from the normalization condition.

The overlap of the meson-photon wave functions (1.42) and (1.43) integrated over z is depicted in Figure 4.4 for a virtuality $Q^2 = 0.05$ GeV^2. The transverse part of the overlap denoted by the red line clearly gives higher contribution to the cross section than the longitudinal part. Depicted results also suggest that the interaction of the proton with dipole of sizes $r = 0.1 - 1$ GeV^{-1} is preferred at this scale.

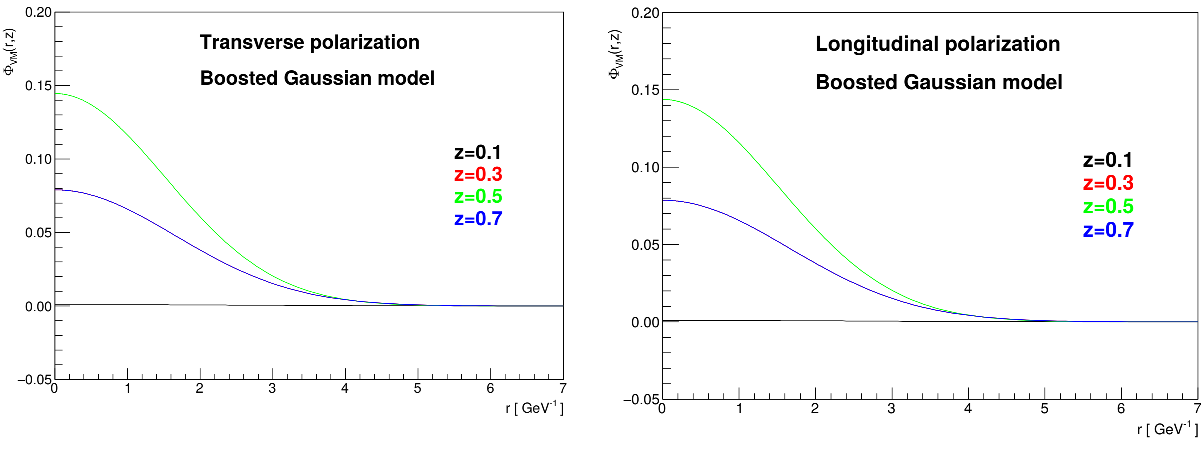

Figure 4.3: Scalar part of the vector meson wave function for transverse (left) and longitudinal (right) polarization of the γ^* using boosted Gaussian model for several momenta fractions z.

$\hat{e}_f$	m_f [GeV]	M_{VM} [GeV]	N_T [−]	N_L [−]	R^2 [GeV^{-2}]
$\frac{2}{3}$	1.4	3.097	0.578	0.575	2.3

Table 4.2: Parameters for the J/ψ vector meson and the photon wave functions overlap and for the scalar part of the vector meson wave function obtained from the boosted Gaussian model, according to [15].

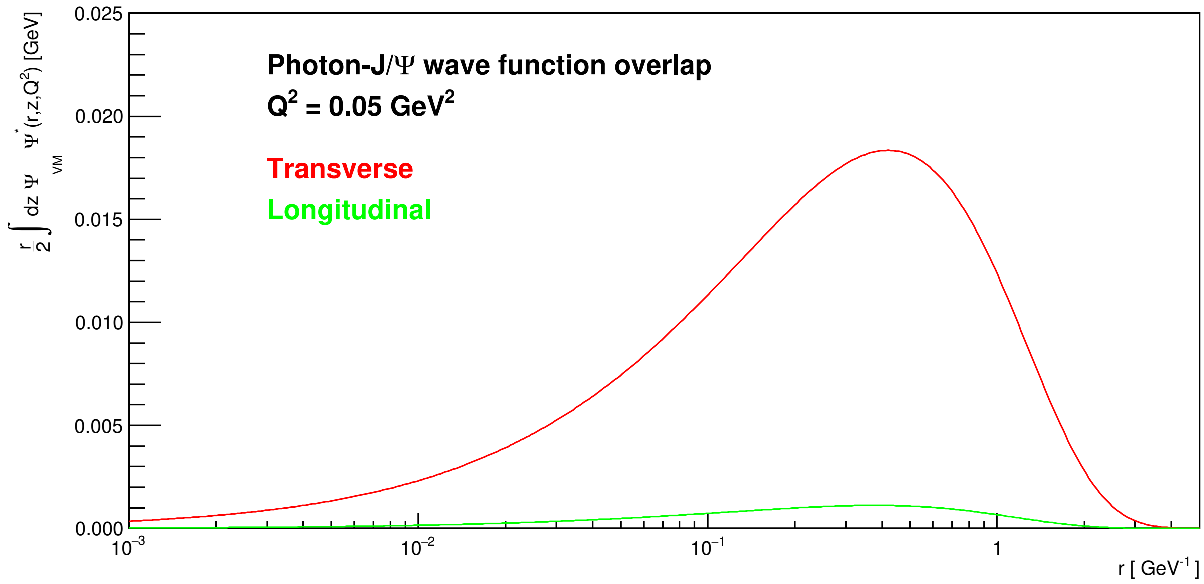

Figure 4.4: Transverse and longitudinal parts of the overlap of the photon and vector meson wave functions integrated over the momentum fraction z for a virtuality $Q^2 = 0.05$ GeV^2.

4.2.2 Cross sections using the GBW parametrization

In this section I present the predictions for the exclusive J/ψ photoproduction and electroproduction cross sections. The properties of all of the parts of the integral over momentum fractions A_z defined as (1.51) were described in the previous section. The integral over the dipole sizes A_r defined as (1.50) is determined by the A_z and the dipole scattering amplitude $N(x, r)$.

The later is obtained from the GBW parametrization (1.31) with parameters set from Table 4.1 row (d) according to [10]. This parametrization also determines the σ_0 parameter. Alternatively, the parameter σ_0 can be obtained from relation $\sigma_0 = 4\pi B$ using the parameter B.

The b-dependent part A_b, defined as (1.49), of the photon-proton amplitude (1.39) is determined by the choice of proton profile function $T_p(b)$. Various options are discussed in Chapter 3.3. We have chosen the Gaussian distribution (3.7) since it provides a simple yet rather realistic parametrization of the proton transverse profile. The integral over b (1.49) can be solved either numerically in the same manner as other integrals in this study, i.e. using Simpson's rule (A.17), or it can be solved analytically. We have decided to obtain the solution of A_b from numerical calculation.

The differential cross section obtained from (1.52) using $\sigma_0 = 23.9$ mb according to Table 4.1 row (d) is presented in Figure 4.5 for various choices of the B parameter and compared to the data from the H1 experiment at HERA [60]. As can be seen this approach does not provide satisfactory predictions for the differential cross section, especially for low values of $|t|$ which form the main contribution to the cross section. Therefore in the Figure 4.6, we provide predictions for the differential cross section with the same parameters except σ_0, which was obtained using relation $\sigma_0 = 4\pi B$ for various choices of B. This approach provides much more accurate description of the HERA data. I chose the value of the B to be $B = 4\ \mathrm{GeV}^{-2}$ based on the results depicted in the Figure 4.6. This choice provides very good description of the differential cross section, especially for the low $|t|$ values, as can be also seen in Figure 4.7 (full red line).

In the Figure 4.7 the computed distribution is compared to the one obtained using $\sigma_0 = 23.9$ mb (full black line). Dashed lines correspond to the cross section obtained without aplying the corrections (1.54) and (1.55) to the scattering amplitude $\mathcal{A}_{T,L}^{\gamma^* p \to VMp}$. These corrections indeed represent a substantial contribution to the differential cross section and therefore can not be neglected. Predictions for electroproduction differential cross sections of the J/ψ photoproduction and their comparison to the H1 data [60] can be seen in Figures 4.8 and 4.9 for the same choice of the $B = 4\ \mathrm{GeV}^{-2}$ parameter. We also present a comparison of the H1 data [60] and our predictions of the differential cross section as a function of W in several bins of $|t|$ for elastic process at $Q^2 = 0.05\ \mathrm{GeV}^2$ and electroproduction at $Q^2 = 8.9$ GeV in Figures 4.10 - 4.13.

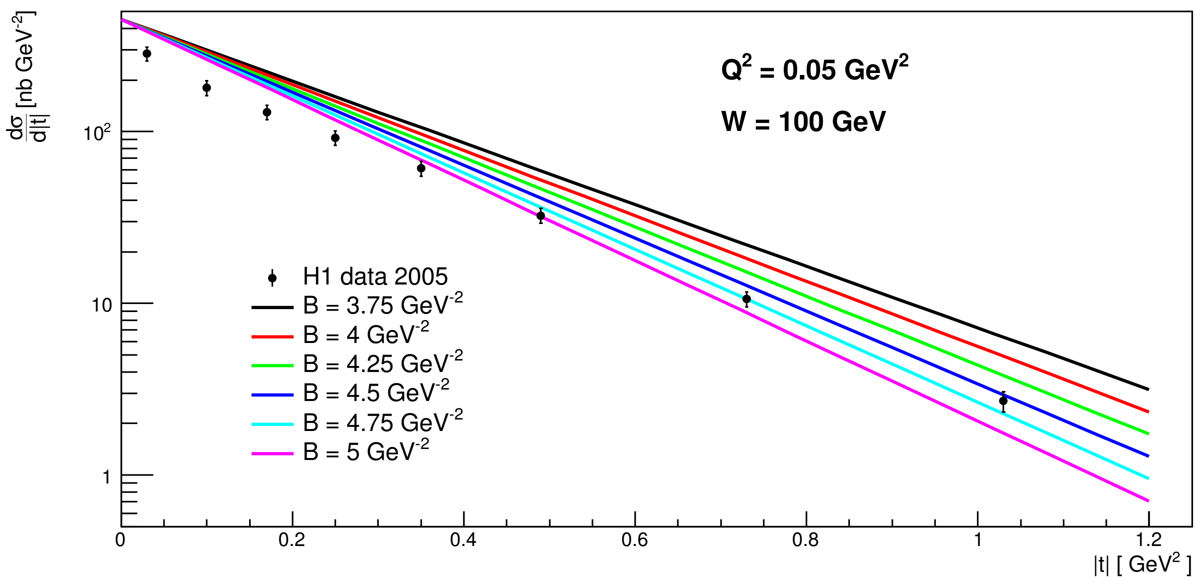

Figure 4.5: The comparison of various choices of the B parameter for the differential cross section of the J/ψ meson at $W = 100$ GeV, $Q^2 = 0.05\ \mathrm{GeV}^2$ using the GBW parametrization with $\sigma_0 = 23.9$ mb. Parameters were used according to Table 4.1 row (d).

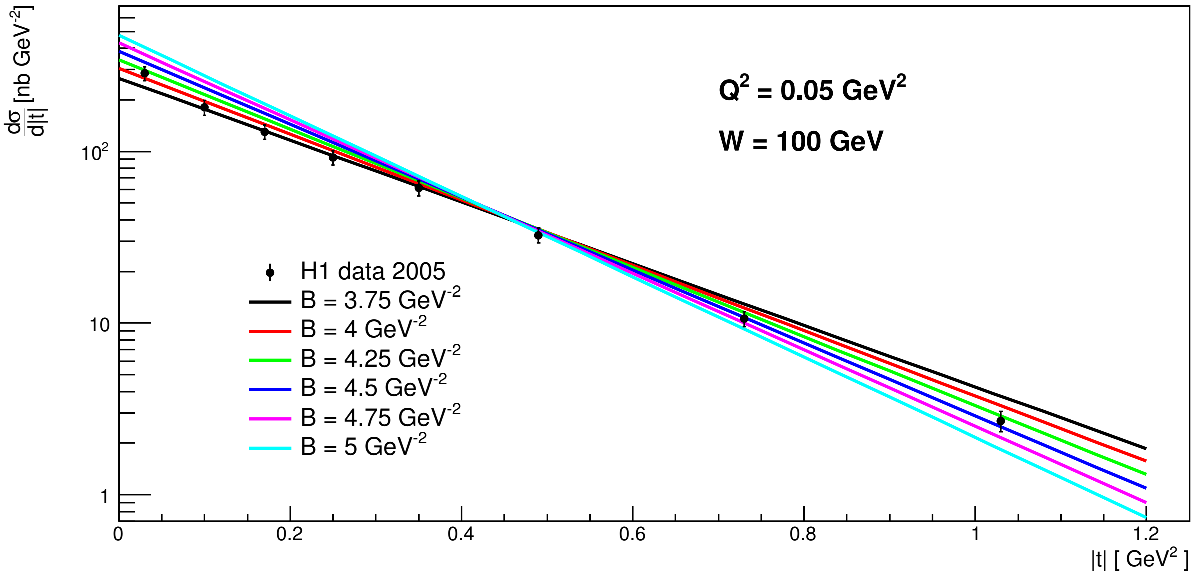

Figure 4.6: The comparison of various choices of the B parameter for the differential cross section of the J/ψ meson at $W = 100$ GeV, $Q^2 = 0.05$ GeV^2 using the GBW parametrization with σ_0 estimated from as $\sigma_0 = 4\pi B$. Parameters were used according to Table 4.1 row (d).

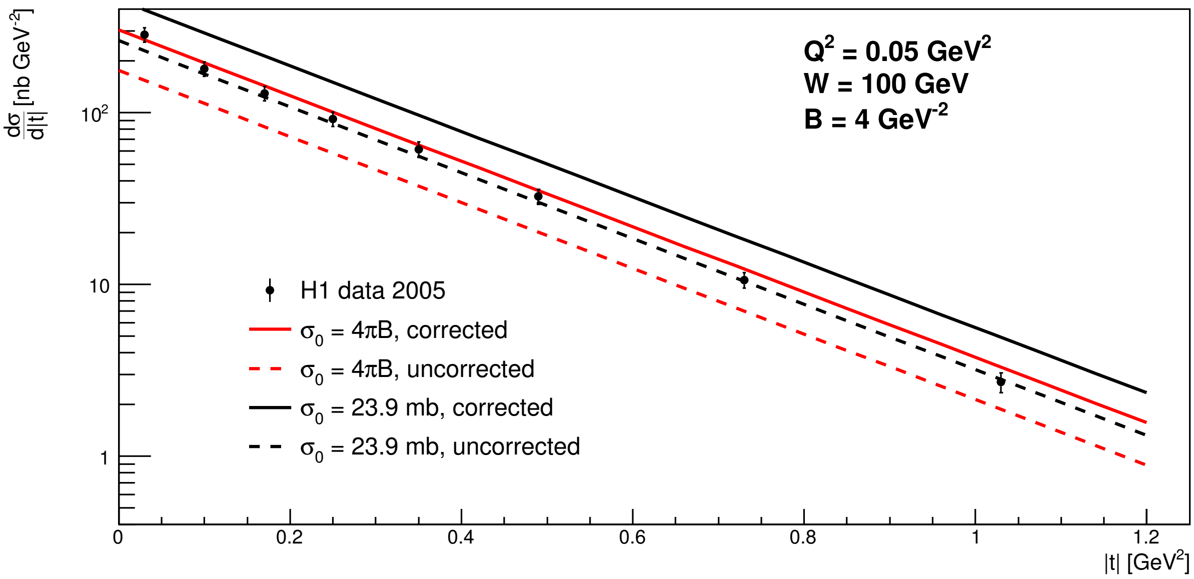

Figure 4.7: The differential cross section of the J/ψ meson at $W = 100$ GeV, $Q^2 = 0.05$ GeV^2 and with $B = 4$ GeV^{-2}. The GBW parametrization was used with parameters according to Table 4.1 row (d).

The predictions for the total exclusive $\gamma^* p \to J/\psi p$ cross section and the comparison to H1 data [60, 61] are presented in Figures 4.14 - 4.16. We present a comparison of three different approaches to the σ_0 and B parameters in Figure 4.14 where predictions for photoproduction

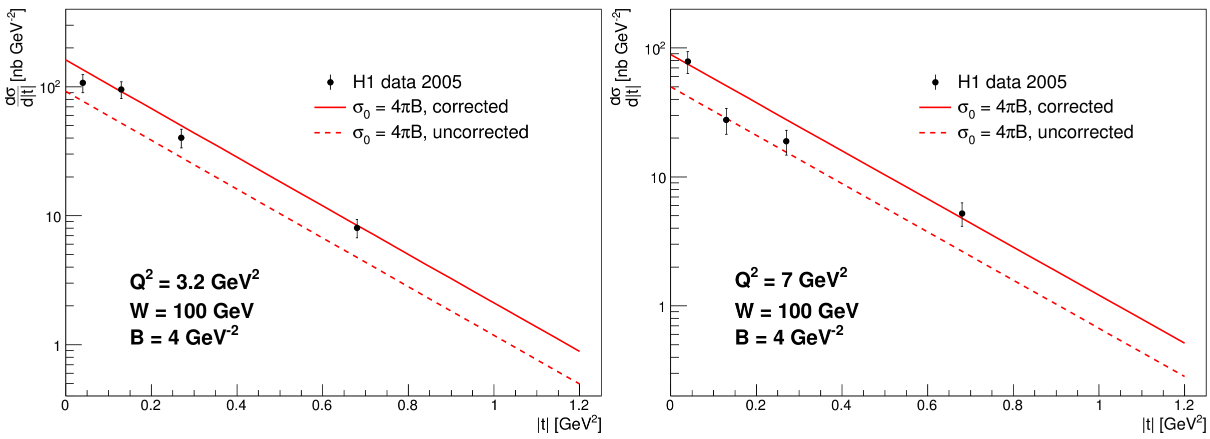

Figure 4.8: The differential cross section of the J/ψ meson at $W = 100$ GeV, for $Q^2 = 3.2$ GeV^2 (left) and $Q^2 = 7$ GeV^2 (right) and with $B = 4$ GeV^{-2}. The GBW parametrization was used with parameters according to Table 4.1 row (d).

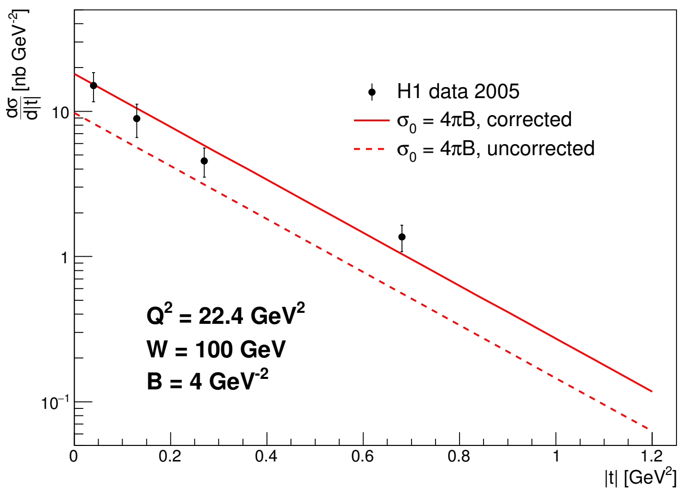

Figure 4.9: The differential cross section of the J/ψ meson at $W = 100$ GeV, $Q^2 = 22.4$ GeV^2 and with $B = 4$ GeV^{-2}. The GBW parametrization was used with parameters according to Table 4.1 row (d).

at $Q^2 = 0.05$ GeV are shown. The $\sigma_0 = 23.9$ mb choice truly does not provide such an accurate description of the data as the choice of $\sigma_0 = 4\pi B$ with $B = 4$ GeV^{-2} in both cases. The disagreement has already been discussed in the previous text and these results only confirm our previous conclusion on this issue. In the same graph, we also present a prediction for the total $\gamma^* p \to J/\psi p$ cross section obtained using W-dependent values of B according to relation (3.4). We conclude that this approach also provides reasonable predictions for the exclusive J/ψ photoproduction cross section using the GBW parametrization with parameters set according to Table 4.1 row (d) [10]. This conclusion is supported by the results for the total $\gamma^* p \to J/\psi p$ electroproduction cross sections compared to H1 data at Figures 4.15 and 4.16.

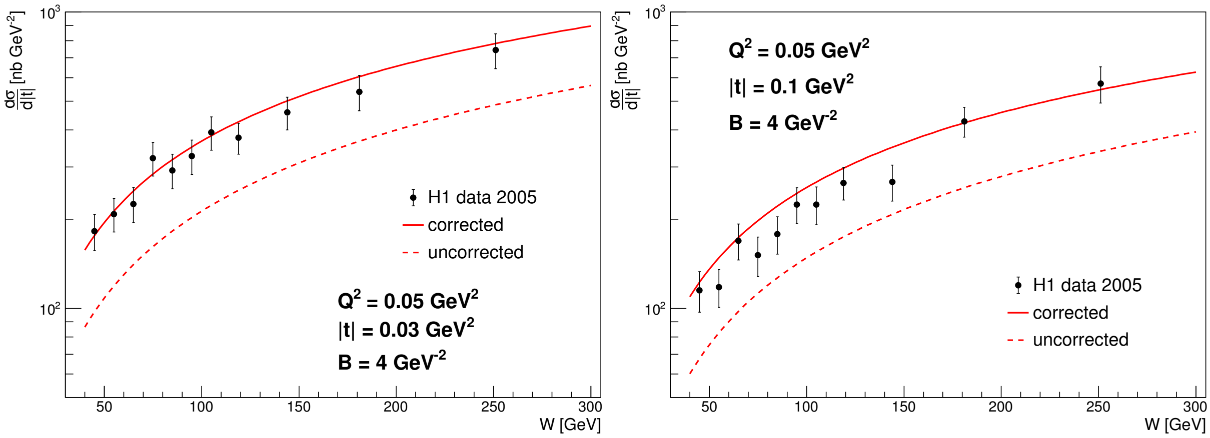

Figure 4.10: The differential cross section of the J/ψ meson as a function of W for $|t| = 0.03$ GeV^2 (left) and $|t| = 0.1$ GeV^2 (right), $Q^2 = 0.05$ GeV^2 and $B = 4$ GeV^{-2}. The GBW parametrization was used with parameters according to Table 4.1 row (d).

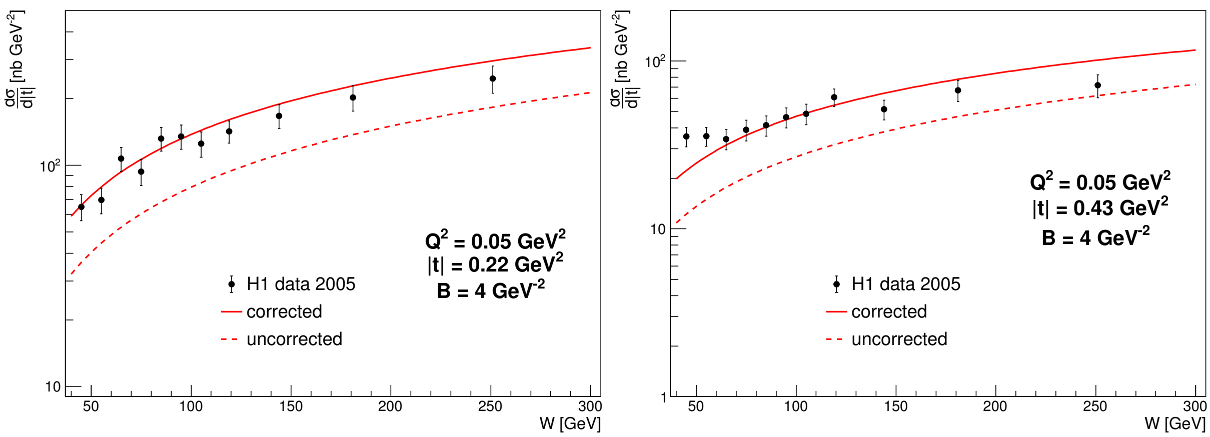

Figure 4.11: The differential cross section of the J/ψ meson as a function of W for $|t| = 0.22$ GeV^2 (left) and $|t| = 0.43$ GeV^2 (right), $Q^2 = 0.05$ GeV^2 and $B = 4$ GeV^{-2}. The GBW parametrization was used with parameters according to Table 4.1 row (d).

4.2.3 Cross sections using the BK solution

In this section I present the predictions for the exclusive J/ψ photoproduction and electroproduction cross sections obtained using the dipole scattering amplitude $N(x, r)$ from a solution to the Balitsky-Kovchegov evolution equation (2.13). The procedure for obtaining the BK equation solution was introduced in Chapter 3.2. We have used the kernel (2.17) with running coupling and evolution was performed from the McLerran-Venugopalan initial condition (2.19) with parameters set according to Table 3.2 row (c). These parameters include the charm quark contribution to the dipole scattering amplitude [15]. The evolution was performed at rapidity $Y = \ln\left(\frac{x_0}{x}\right)$ where x_0 represents the Bjorken-x value from which the evolution from MV initial condition starts. All the other procedures concerning the cross section calculation were permormed in the same manner as described in previous section where the GBW parametrization

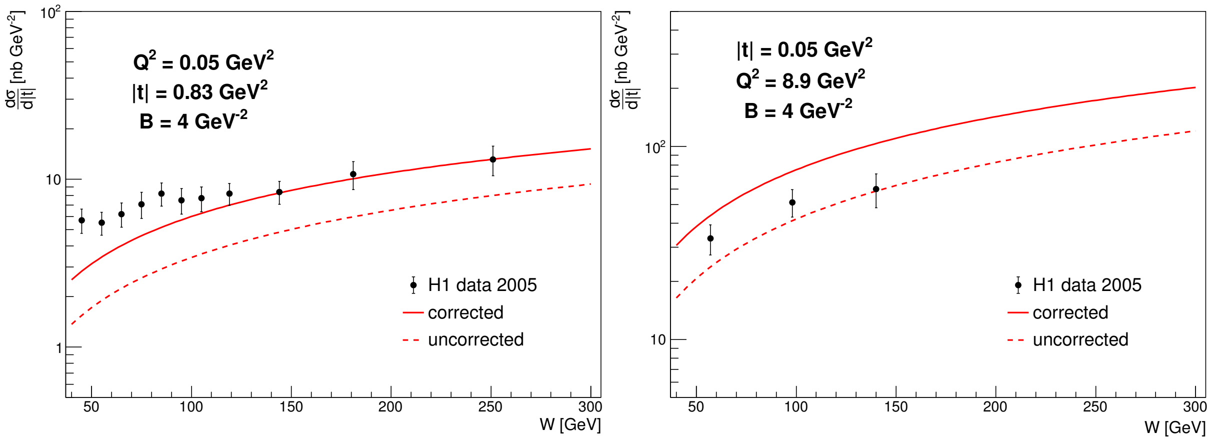

Figure 4.12: The differential cross section of the J/ψ meson as a function of W with $B = 4$ GeV^{-2} for $|t| = 0.83$ GeV^2 with $Q^2 = 0.05$ GeV^2 (left) and for $|t| = 0.05$ GeV^2 with $Q^2 = 8.9$ GeV^2 (right). The GBW parametrization was used with parameters according to Table 4.1 row (d).

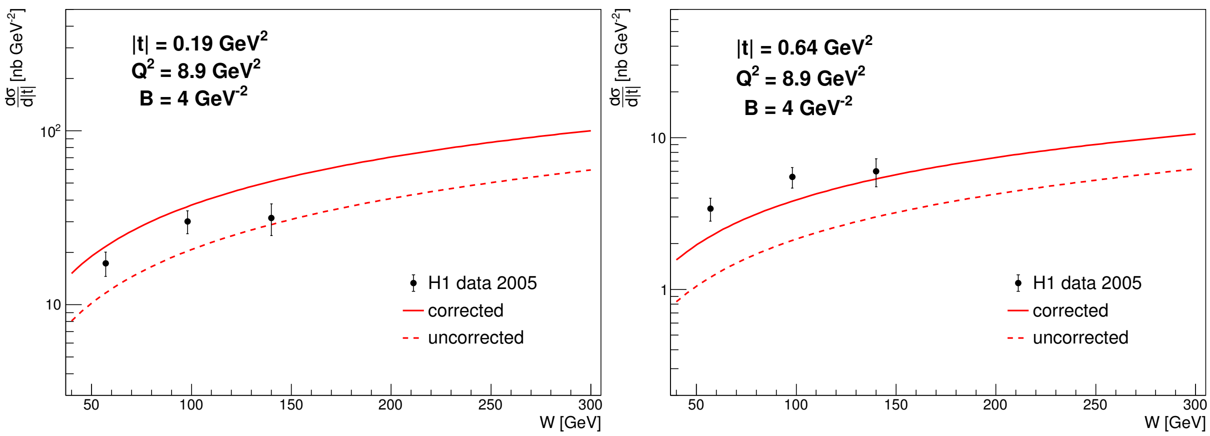

Figure 4.13: The differential cross section of the J/ψ meson as a function of W for $|t| = 0.19$ GeV^2 (left) and $|t| = 0.64$ GeV^2 (right), $Q^2 = 8.9$ GeV^2 and $B = 4$ GeV^{-2}. The GBW parametrization was used with parameters according to Table 4.1 row (d).

was used.

Similarly to the previous section we present the comparison of the differential cross section to the H1 data [60, 61] at $Q^2 = 0.05$ GeV^2 for various choices of the B parameters in Figure 4.17. Due to the reasons discussed in previous section we no longer use the σ_0 parameter estimated from a fit from [15]. Based on the results presented in Figure 4.17 we have chosen the value $B = 5$ GeV for the next calculation. As can be seen from Figures 4.18 and 4.19 this choice provides a satisfactory agreement with the data. We also present the predictions for the differential cross section as a function of W for various values of $|t|$ in Figures 4.20 - 4.13. For the elastic process at $Q^2 = 0.05$ GeV^2 our predictions are in a good agreement with the data, although for higher values of W and $|t|$ the trend of the model underestimates the data. For the electroproduction at $Q^2 = 8.9$ GeV^2 a somehow satisfactory result is obtained at $|t| = 0.19$ GeV^2 in Figure 4.23 (left), however for the other two $|t|$ bins our prediction is rather unsuccessful.

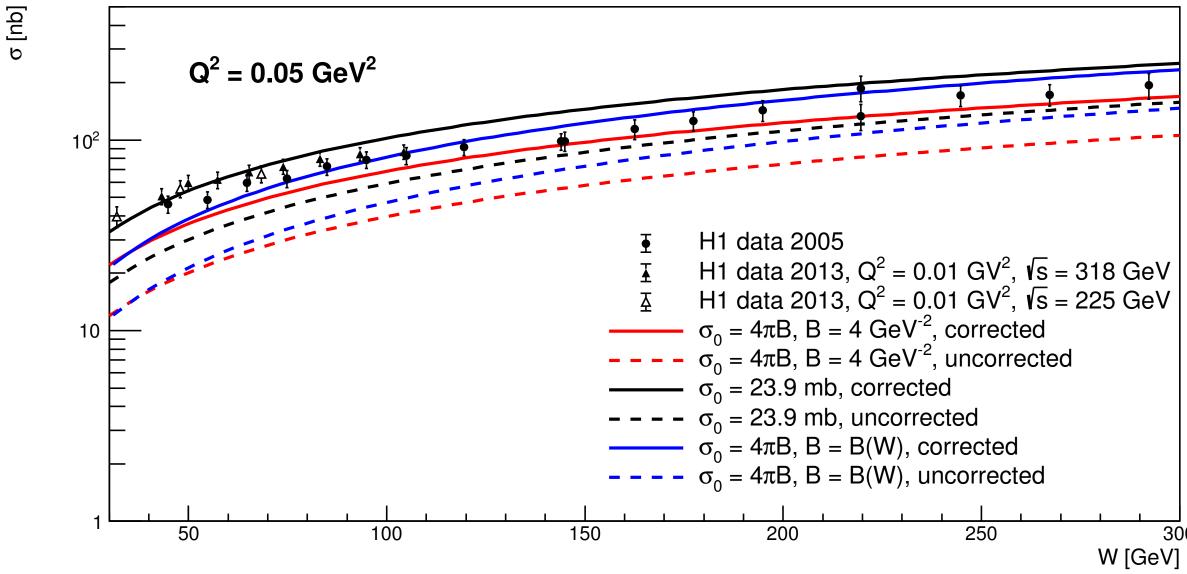

Figure 4.14: The total cross section of the J/ψ meson at $Q^2 = 0.05$ GeV^2 with $B = 4$ GeV^{-2} and using W-dependent B according to (3.4). The GBW parametrization was used with parameters according to Table 4.1 row (d).

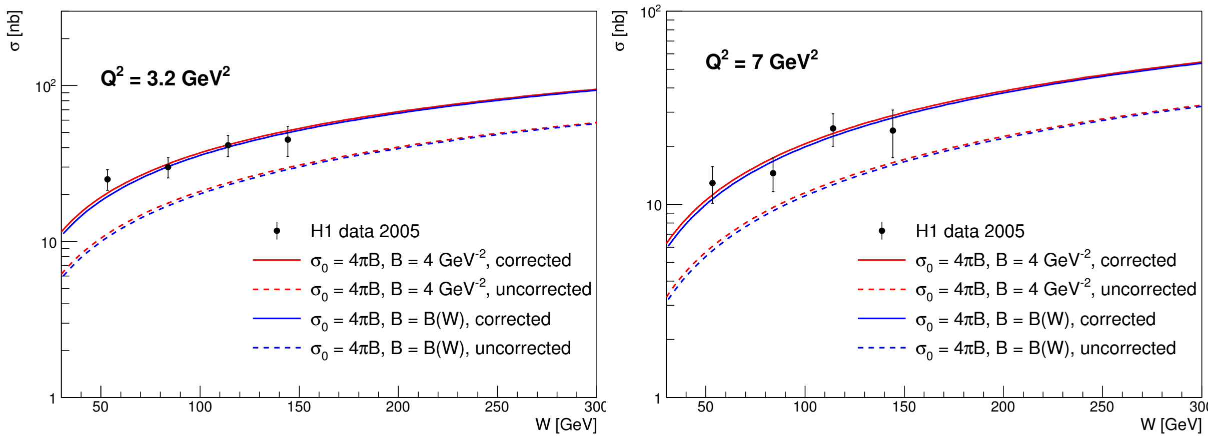

Figure 4.15: The total cross section of the J/ψ meson with $B = 4$ GeV^{-2} and using W-dependent B according to (3.4) at $Q^2 = 3.2$ GeV^2 (left) and at $Q^2 = 7$ GeV^2 (right). The GBW parametrization was used with parameters according to Table 4.1 row (d).

The predictions for the total $\gamma^* p \to J/\psi p$ cross section are presented in Figures 4.24, 4.25 and 4.26 and compared to H1 data [60]. In Figure 4.24 we again present the comparison between the fixed choice of the B parameter at value $B = 5$ GeV^{-2} and the W-dependent parameter B scenario for the elastic process at $Q^2 = 0.05$ GeV^2. As can be seen both approaches describe the data very well at low values of W, however they tend to underestimate the data for the values of energy W larger than $W \approx 180$ GeV. The choice of $\sigma_0 = 4\pi B$ with $B = 5$ GeV^2 provides good agreement with the data for electroproduction processes, as can be seen from Figures 4.25

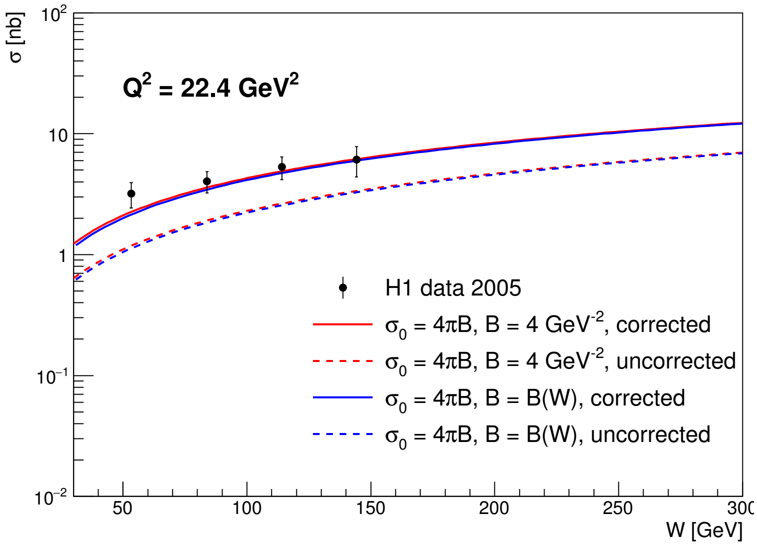

Figure 4.16: The total cross section of the J/ψ meson at $Q^2 = 22.4$ GeV^2 with $B = 4$ GeV^{-2} and using W-dependent B according to (3.4). The GBW parametrization was used with parameters according to Table 4.1 row (d).

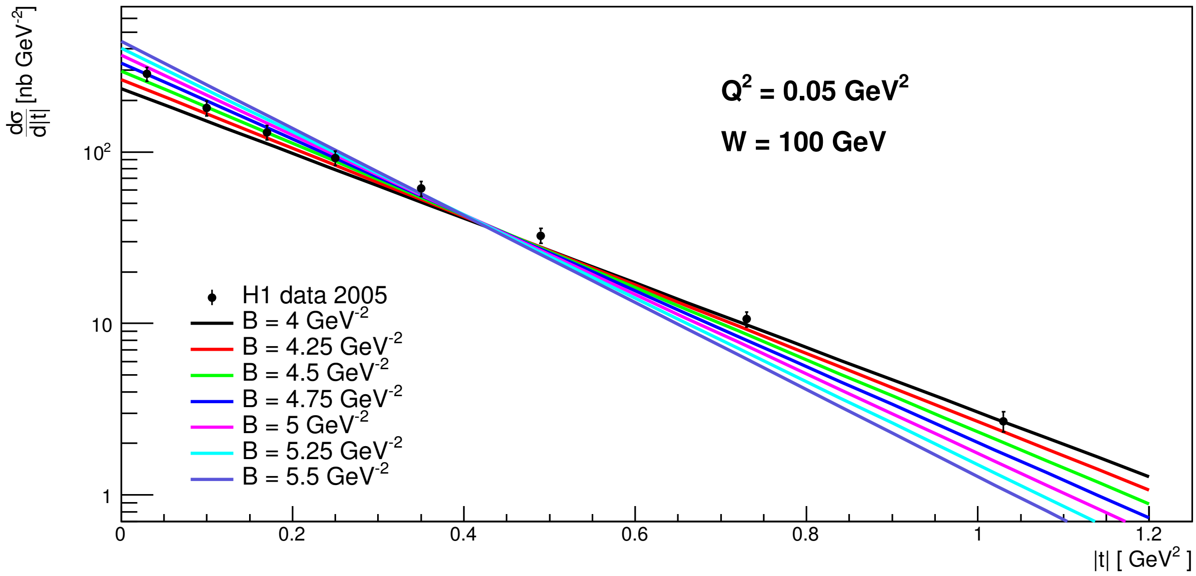

Figure 4.17: The comparison of various choices of the B parameter for the differential cross section of the J/ψ meson at $W = 100$ GeV, $Q^2 = 0.05$ GeV^2 using the BK equation (2.13) solution with σ_0 estimated from as $\sigma_0 = 4\pi B$. Parameters were used according to Table 3.2 row (c).

and 4.26. The W-dependent approach to the parameter B, however, significantly overestimates the J/ψ electroproduction cross section at $Q^2 = 3.2$ GeV^2. We therefore don't further employ this approach for the electroproduction cross-sections depicted in Figure 4.26.

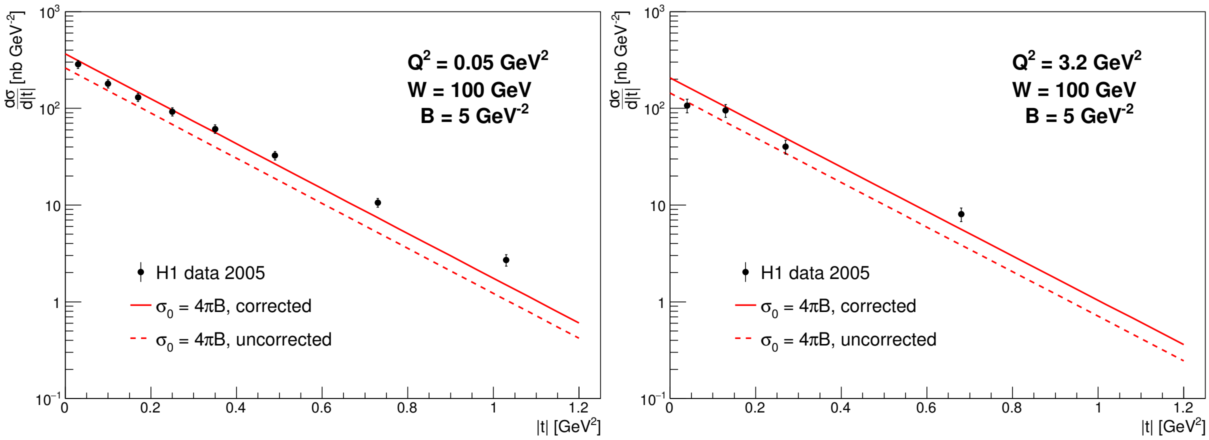

Figure 4.18: The differential cross section of the J/ψ meson with $B = 5\ \mathrm{GeV}^{-2}$ at $Q^2 = 0.05\ \mathrm{GeV}^2$ (left) and at $Q^2 = 3.2\ \mathrm{GeV}^2$ (right). Solution to the BK equation (2.13) was used with parameters according to Table 3.2 row (c).

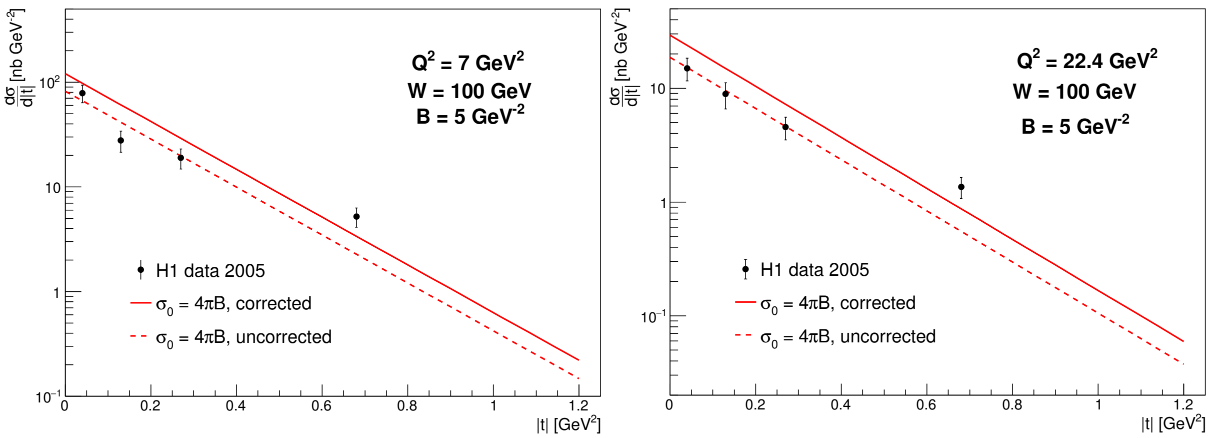

Figure 4.19: The differential cross section of the J/ψ meson with $B = 5\ \mathrm{GeV}^{-2}$ at $Q^2 = 7\ \mathrm{GeV}^2$ (left) and at $Q^2 = 22.4\ \mathrm{GeV}^2$ (right). Solution to the BK equation (2.13) was used with parameters according to Table 3.2 row (c).

4.2.4 Exclusive J/ψ cross section with hot-spot model

In this section I provide a prediction for the exclusive J/ψ photoproduction cross section using hot-spot model to parametrize the transverse structure of the proton. The main properties of this model are presented in Chapter 3.3.1. The b-dependent part of the amplitude (1.39) is solved analytically in this case, details are given in Appendix D. The dipole scattering amplitude $N(x, r)$ is obtained from the GBW parametrization (1.31) with parameters set to row (a) of the Table 4.1. The parameter B is set as $B = 4.7$ GeV and σ_0 is obtained from $\sigma_0 = 4\pi B$ as in previous studies. Average of the squared transverse radius of hot spots is set to $B_{hs} = 0.8\ \mathrm{GeV}^{-2}$ and the parameters for the x-dependent value of number of hot spots given by (3.11) are given in Table 3.4. All the parameters were set according to paper [58]. In this paper however the authors use a fixed number of hot spots in each configuration. Since we obtain the number of

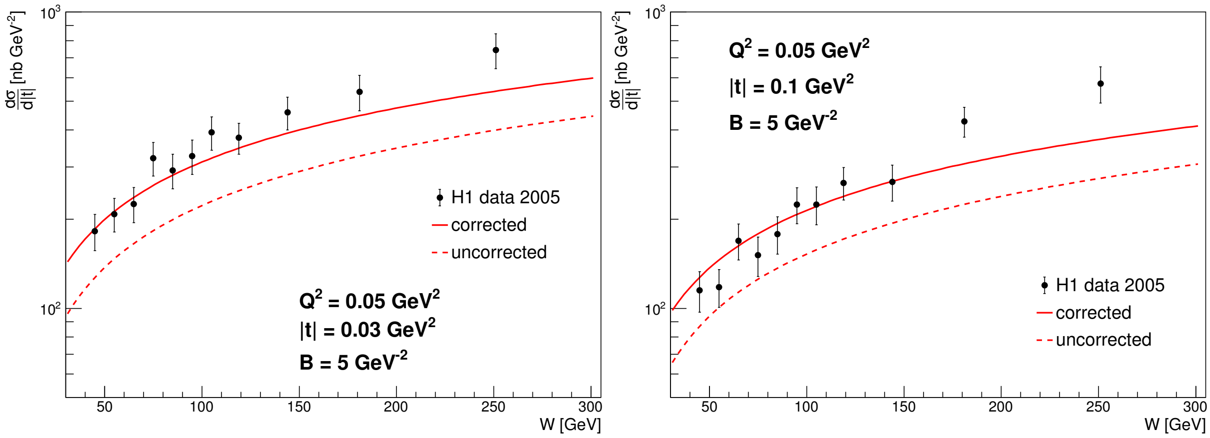

Figure 4.20: The differential cross section of the J/ψ meson as a function of W for $|t| = 0.03$ GeV^2 (left) and $|t| = 0.1$ GeV^2 (right), $Q^2 = 0.05$ GeV^2 and $B = 5$ GeV^{-2}. Solution to the BK equation (2.13) was used with parameters according to Table 3.2 row (c).

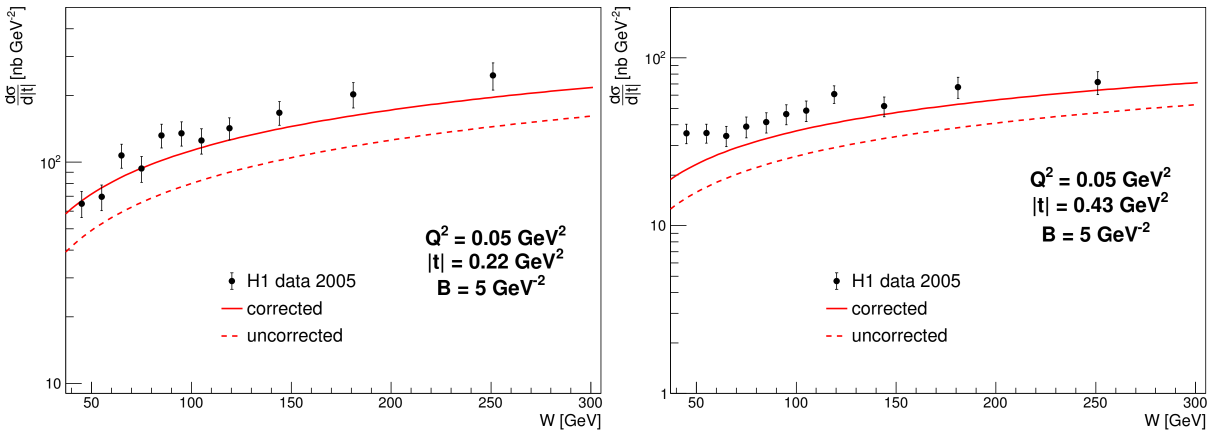

Figure 4.21: The differential cross section of the J/ψ meson as a function of W for $|t| = 0.22$ GeV^2 (left) and $|t| = 0.43$ GeV^2 (right), $Q^2 = 0.05$ GeV^2 and $B = 5$ GeV^{-2}. Solution to the BK equation (2.13) was used with parameters according to Table 3.2 row (c).

hot spots N_{hs} in the given configuration from the zero-truntcated Poisson distribution (see [62]) the slight change of the p_2 parameter was applied according to paper [59]. This change however should not affect the exclusive cross section results.

The predictions for the differential cross section are shown in Figure 4.27. We compare these predictions to the two sets of data measured at the H1 experiment [61]. Our predictions provide a satisfactory description of the data for low values of $|t|$, especially at $< W >= 78$ GeV which is the mean value of energy W at which the high energy data set [61] was obtained.

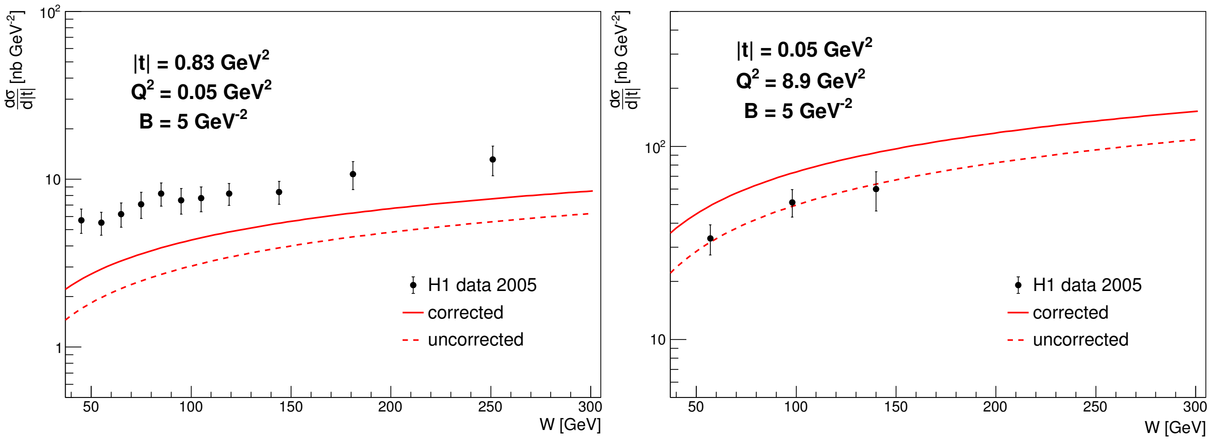

Figure 4.22: The differential cross section of the J/ψ meson as a function of W with $B = 5$ GeV^{-2} for $|t| = 0.83$ GeV^2 with $Q^2 = 0.05$ GeV^2 (left) and for $|t| = 0.05$ GeV^2 with $Q^2 = 8.9$ GeV^2 (right). Solution to the BK equation (2.13) was used with parameters according to Table 3.2 row (c).

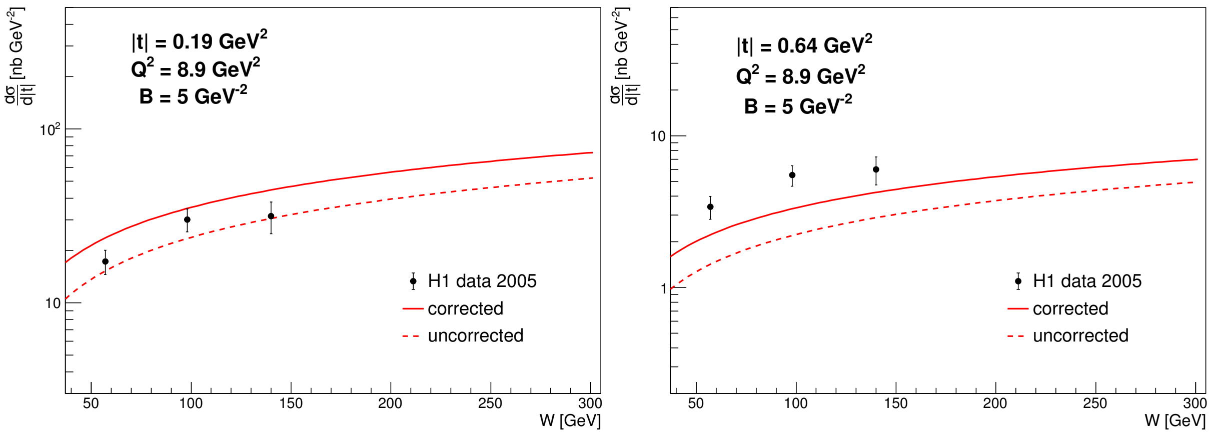

Figure 4.23: The differential cross section of the J/ψ meson as a function of W for $|t| = 0.19$ GeV^2 (left) and $|t| = 0.64$ GeV^2 (right), $Q^2 = 8.9$ GeV^2 and $B = 5$ GeV^{-2}. Solution to the BK equation (2.13) was used with parameters according to Table 3.2 row (c).

The prediction for the energy dependence of the total exclusive J/ψ photoproduction cross section using hot-spot model is depicted in Figure 4.28 and compared to both the high energy and low energy H1 datasets [61], the H1 data [60] measured at $< Q^2 = 0.05$ GeV^2 and also to the data obtained by the ALICE experiment in $p - Pb$ collisions at $\sqrt{s} = 5.02$ TeV at the LHC [63]. In the $p - Pb$ ultra-peripheral collisions the lead nucleus is taken as a virtual photon flux source since it is more probable for the lead ion to radiate the virtual photon and also the cross section of the coherent virtual photon interaction is much larger for the proton than for the lead nucleus. We conclude that the model describes reasonably well the data from both experiments.

I also present the prediction for the energy dependence of the total exclusive J/ψ electroproduction cross section with the hot-spot model. The comparison of results and H1 data [60] is depicted in Figures 4.29, 4.30 and 4.31. The predictions for $Q^2 = 3.2$ GeV^2 and $Q^2 = 7$ GeV^2 provide satisfactory description of the provided data. The prediction of the model for electro-

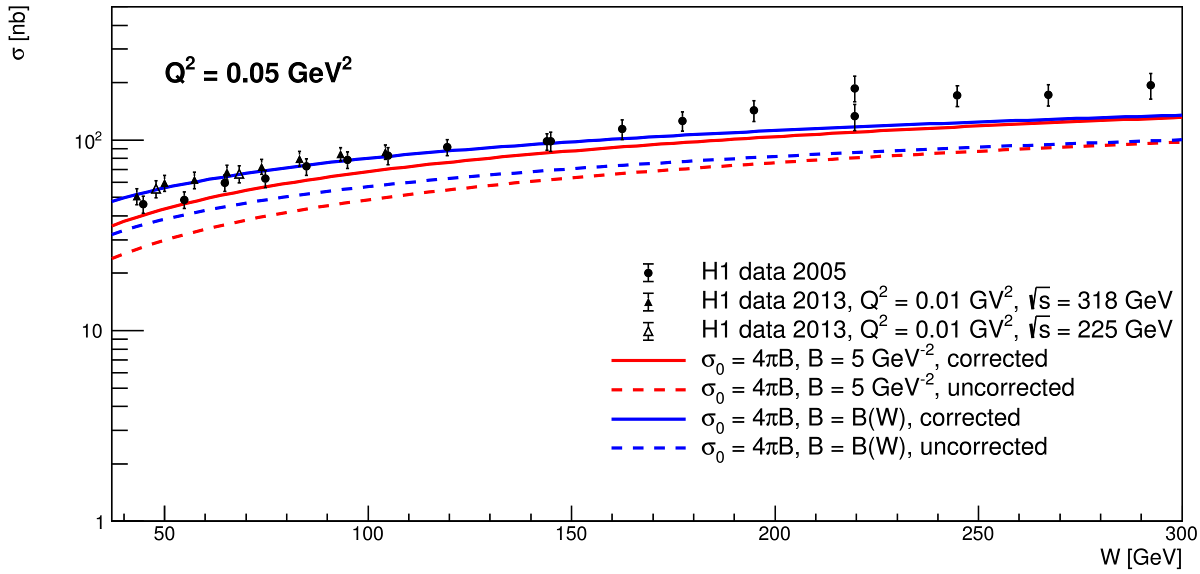

Figure 4.24: The total cross section of the J/ψ meson at $Q^2 = 0.05$ GeV^2 with $B = 5$ GeV^{-2} and using the W-dependent parameter B according to (3.4). Solution to the BK equation (2.13) was used with parameters according to Table 3.2 row (c).

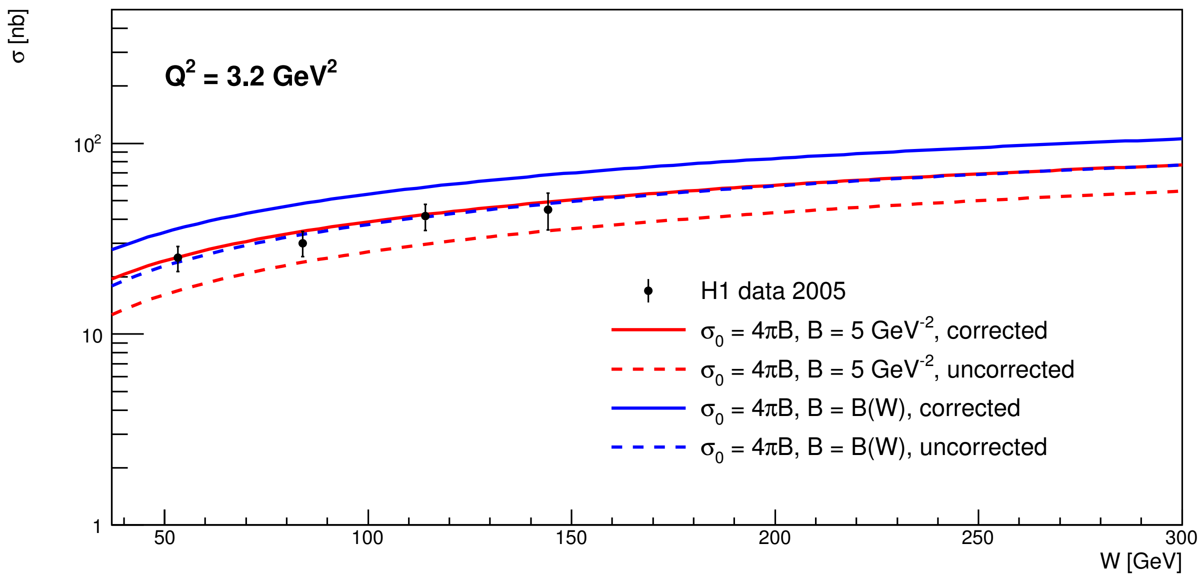

Figure 4.25: The total cross section of the J/ψ meson at $Q^2 = 3.2$ GeV^2 with $B = 5$ GeV^{-2} and using the W-dependent parameter B according to (3.4). Solution to the BK equation (2.13) was used with parameters according to Table 3.2 row (c).

production cross section at $Q^2 = 22.4$ GeV however uderestimates the data but still is within the uncertainties of the data. The conslusion is therefore that parametrization of the transverse

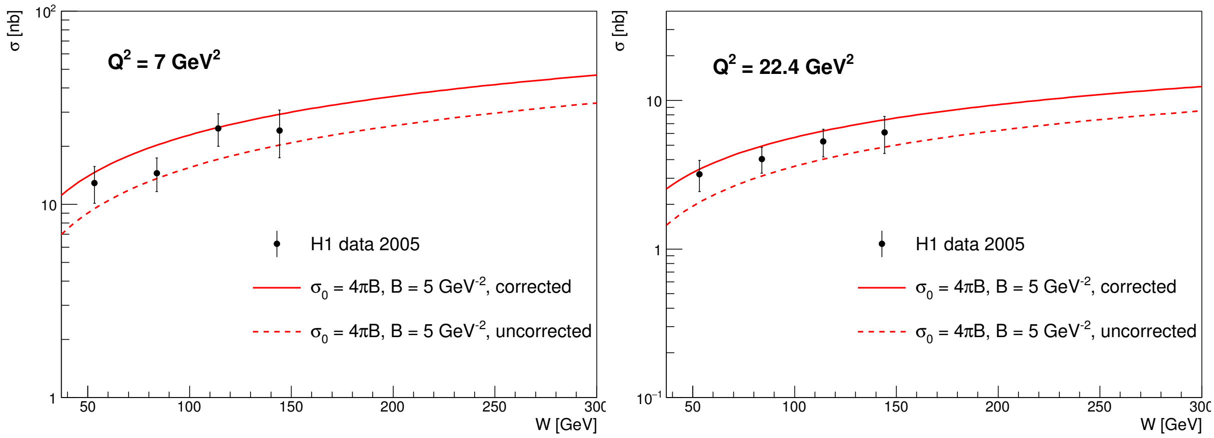

Figure 4.26: The total cross section of the J/ψ meson with $B = 5\ \mathrm{GeV}^{-2}$ and using the W-dependent parameter B according to (3.4) at $Q^2 = 7\ \mathrm{GeV}^2$ (left) and at $Q^2 = 22.4\ \mathrm{GeV}^2$ (right). Solution to the BK equation (2.13) was used with parameters according to Table 3.2 row (c).

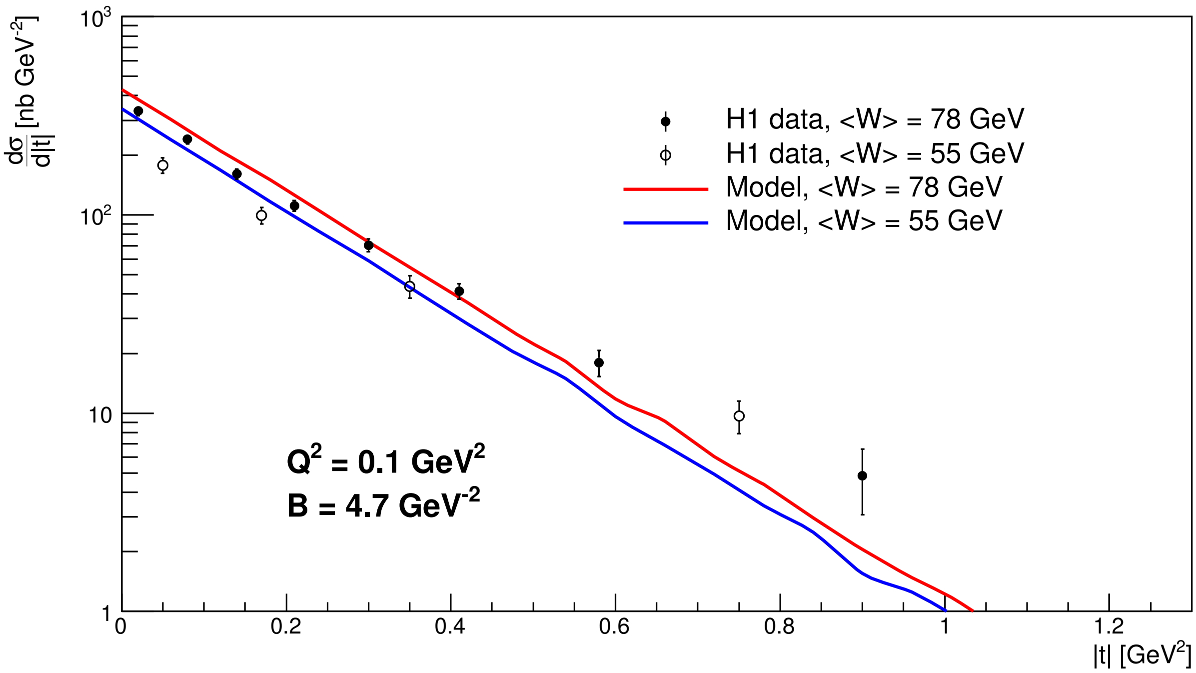

Figure 4.27: The differential cross section of the exclusive J/ψ photoproduction at $Q^2 = 0.1\ \mathrm{GeV}^2$ with $B = 4.7\ \mathrm{GeV}^{-2}$ using hot-spot model with parameters from Table 3.4. The GBW parametrization was used with parameters according to Table 4.1 row (a).

structure of the proton provided by the hot-spot model gives satisfactory results for both the exclusive photoproduction and electroproduction cross sections.

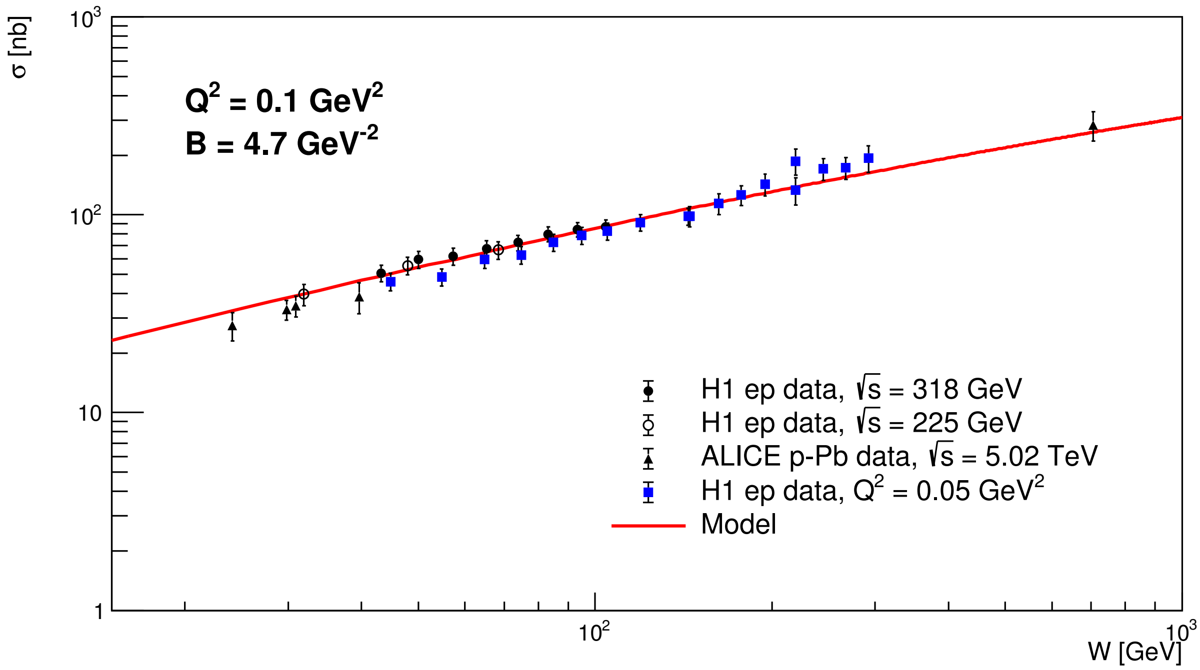

Figure 4.28: The total cross section of the exclusive J/ψ photoproduction at $Q^2 = 0.1$ GeV^2 with $B = 4.7$ GeV^{-2} using hot-spot model with parameters from Table 3.4. The GBW parametrization was used with parameters according to Table 4.1 row (a).

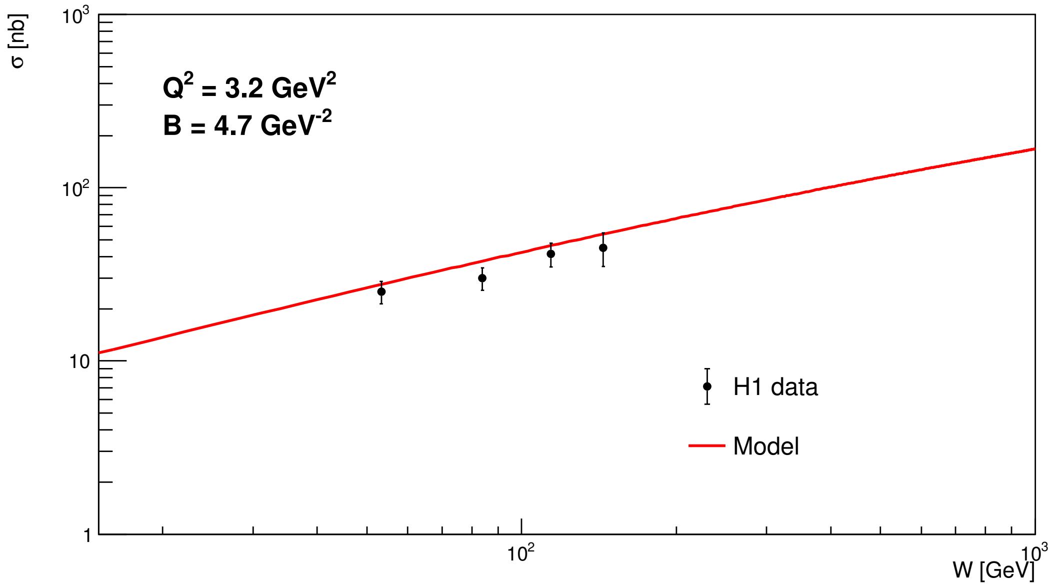

Figure 4.29: The total cross section of the exclusive J/ψ electroproduction at $Q^2 = 3.2$ GeV^2 with $B = 4.7$ GeV^{-2} using hot-spot model with parameters from Table 3.4. The GBW parametrization was used with parameters according to Table 4.1 row (a).

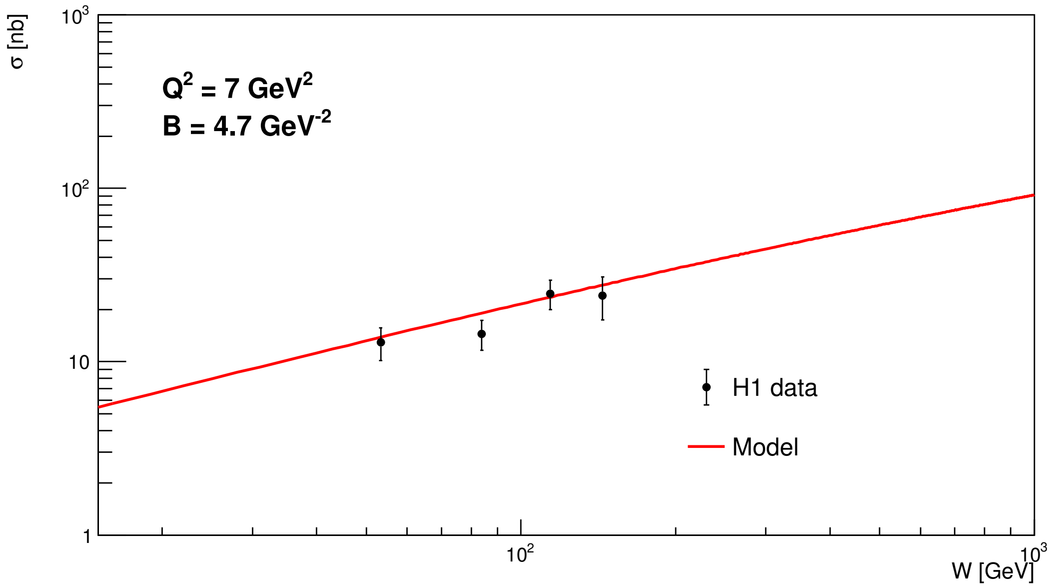

Figure 4.30: The total cross section of the exclusive J/ψ electroproduction at $Q^2 = 7$ GeV^2 with $B = 4.7$ GeV^{-2} using hot-spot model with parameters from Table 3.4. The GBW parametrization was used with parameters according to Table 4.1 row (a).

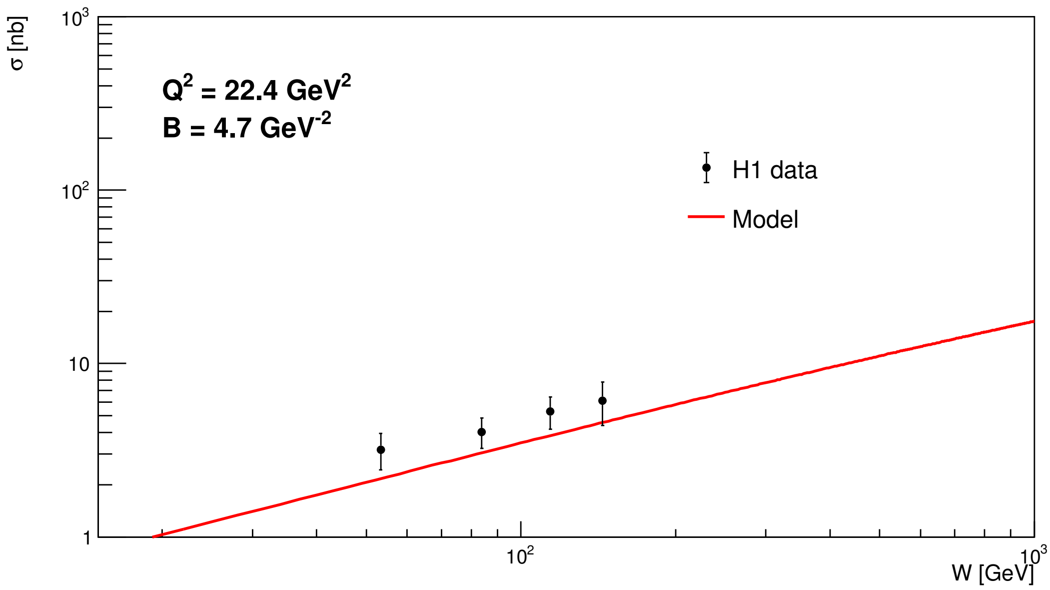

Figure 4.31: The total cross section of the exclusive J/ψ electroproduction at $Q^2 = 22.4$ GeV^2 with $B = 4.7$ GeV^{-2} using hot-spot model with parameters from Table 3.4. The GBW parametrization was used with parameters according to Table 4.1 row (a).

Conclusion

The exclusive vector meson production can be used as a probe of gluon structure of hadrons. There are several approaches and models which describe the individual parts of the $\gamma^* p \to VMp$ scattering amplitude. The photon wave function can be obtained from Quantum electrodynamics and its properties are well known. However the vector meson wave function has to be modelled in order to obtain its overlap with the virtual photon wave function, for example by the the boosted Gaussian model used in this work. Another non-trivial task is to obtain the amplitude of the dipole-proton scattering which in general depends on the impact parameter b. One of the possible approaches is to express the b-dependence of the dipole-proton cross section by the function $T_p(b)$ which parametrizes the transverse structure of the proton. The appropriate choice of $T_p(b)$ again represents a challenge. I have chosen to examine two choices - the parametrization of the transverse proton profile by the simple Gaussian distribution (3.7) and the parametrization using the hot spots model 3.3.1. This model allows us to consider a proton as a set of clusters with high gluonic density (called hot spots). The proton profile is then estimated from various random configurations of such clusters. The rest of the dipole-proton is then determined by the b-independent dipole scattering amplitude $N(x, r)$ and the normalisation factor σ_0. The later is determined by a fit to data. The dipole scattering amplitude $N(x, r)$ can be obtained from the simple parametrization (1.31) from model of Golec-Biernat and Wusthoff or it can be obtained as the solution to the evolution equation of parton densities such as the Balitsky–Kovchegov equation (2.13).

The Balitsky–Kovchegov evolution equation was numerically solved using the Runge-Kutta methods of the first, the second and the fourth order, Simpson's rule and the linear interpolation. Several input choices were investigated. I have solved the Balitsky–Kovchegov equation using the LO kernel (2.14) with either fixed and running strong coupling constant α_S using the GBW initial condition (2.18). From the comparison of the resultant $N(r, Y)$ evolution the conclusion is that the choice of a fixed coupling does not provide satisfactory results since the evolution proceeds too fast. The running coupling, even at the one loop approximation of α_S, therefore provides more sufficient evolution of the dipole scattering amplitude $N(r, Y)$. I have also compared the evolution of $N(r, Y)$ using the LO kernel (also called the BFKL kernel within this work) given by eq. (2.14) and the NLO kernel (also called the Balitsky kernel) given by eq. (2.17), both with the running coupling and for both initial conditions - GBW (2.18) and MV (2.19). The conclusion is that the the NLO kernel provides much more sufficient $N(r, Y)$ evolution which is slower and the result is consistent with the data as will be discussed later. The comparison of the two choices of the initial conditions for the NLO kernel shows only small differences of the dipole scattering amplitude $N(r, Y)$ at small rapidities. These differences are gradually disappearing with the increasing rapidity, exhibiting the geometric scaling phenomenon. The dipole can be in general formed by the $q\bar{q}$ pair of any flavours which allows the heavy charm and beauty quarks to contribute to the dipole scattering amplitude. The contribution of the top quark is not accounted as its lifetime is shorter then the mean lifetime of the dipole existence. Heavy quark contribution influences the running coupling values and therefore via the kernel it affects the resulting evolution in Y of the dipole scattering amplitude. Since the transverse distance of the $q\bar{q}$ is smaller for the quarks of heavier flavours, the scattering amplitude is therefore larger than that of the dipole formed by only light quarks at the same rapidity Y.

The solution to the Balistky–Kovchegov equation was used for the dipole scattering amplitude estimation within the deep inelastic scattering. We have obtained the prediction for the structure function F_2 and compared it to the predictions obtained from the GBW parametrization of the dipole-proton cross section with various choices of the prescription (1.31) parameters. I have also compared all the mentioned predictions of the F_2 structure function with the HERA data [9] combined from H1 and ZEUS experiments. The conclusion is that the predictions are in good agreement with the data. In the following parts of this work I have therefore focused on the vector meson production, which can also be viewed in the color dipole framework.

First I have chosen to estimate the exclusive J/ψ cross section using a simple and direct GBW prescription for the dipole scattering amplitude $N(x, r)$. The comparison of the differential and the total J/ψ exclusive photoproduction and electroproduction cross section with the data yields very satisfactory results for such a simple model. The best agreement was obtained using a B-dependent factor $\sigma_0 = 4\pi B$ with the choice of the Gaussian distribution width $B = 4$ GeV^{-2}. I have also employed the energy-dependent prescription (3.4) for the values of the B parameter. This concrete prescription was obtained from fits to the H1 experiment data [52]. As a result of the presented calculations suggest, this prescription provide very good description of the experimental data in both photoproduction and electroproduction for the GBW parametrization. Such an agreement is truly remarkable as the employed model is rather simple, yet it depends on the number of various parameters estimated from a fit to the relevant data.

I have also performed all of the above described calculations of the exclusive J/ψ photoproduction cross sections using the previously obtained dipole scattering amplitude $N(x, r)$ as a solution of the running coupling Balitsky-Kovchegov evolution equation (2.13) with the NLO Balitsky kernel (2.17), McLerran-Venugopalan model inspired initial condition (2.19) and allowing the charm quark contribution within the variable scale scheme 2.3.2.3. The slight change of the Gaussian width $B = 5$ GeV^{-2} parameter had to be make in order to compensate the resulting difference between the two approaches to the dipole scattering amplitude $N(x, r)$. The differential J/ψ cross section data [60] are described reasonably well with these predictions. However the trend of the differential cross section energy dependence differs from the measured data at high values of W and also for electroproduction at $Q^2 = 8.9$ GeV. The total photoproduction $\gamma^* p \rightarrow J/\psi p$ cross section at $Q^2 = 0.05$ GeV^2 with the $\sigma_0 = 4\pi B$ parameter gives reasonably good results when compared to the data for both fixed $B = 5$ GeV^{-2} and energy dependent value of B according to (3.4). However the W-dependent value of B seems to be an inappropriate choice for the electroproduction at $Q^2 = 3.2$ GeV, $Q^2 = 7.0$ GeV and $Q^2 = 22.4$ GeV.

The prediction of the exclusive J/ψ photoproduction cross section were also obtained with the hot spots model as the way to parametrize the transverse structure of the proton. Both the differential and the total cross section calculations exhibit a good agreement with the two sets of the HERA data measured at H1 experiment. The total cross section is also compared to the data from ultra-peripheral collisions of $p - Pb$ at ALICE experiment. Our predictions give very satisfactory predictions to the both H1 and ALICE data. The electroproduction cross sections were also obtained using this approach to the transverse proton profile parametrization. It provides good agreement with the combined H1 and ZEUS data, especially at $Q^2 = 3.2$ GeV^2 and $Q^2 = 7$ GeV^2. The results for exclusive J/ψ electroproduction are new and therefore their successful description of the HERA data is very promising for future studies of vector meson production using the hot-spot model. The interesting phenomenon for further work is the dissociative J/ψ cross section which represents a significant contribution to the total J/ψ cross section. However the increasing trend of the cross section with increasing energy W, observed in the exclusive case, should exhibit a turnover at the value $W \approx 500$ causing the disappearance of the dissociative contribution to the total J/ψ cross section at high energies as have been predicted in [58].

The above concluded three sets of results for exclusive J/ψ photoproduction and electroproduction indicate that the approach to the impact-parameter dependence of the dipole cross section presented in Chapter 3 provides very good description of the experimentally measured data. It is therefore highly desirable to examine its applicability to other vector mesons or to the interaction of nuclei, as have recently been presented in papers [59, 64].

All of the presented approaches rely on a set of various parameters which determine the behavior of the given model. These parameters were mostly obtained from various fits to HERA data, see e.g. [10, 15]. The above presented models are therefore strongly dependent on the given choice of the parameters and inaccuracy of the result correlates with the appropriate choice of parameters.

To conclude, in this thesis we have explained the concept of color dipole approach to the deep inelastic scattering 1.2 and to the vector meson production 1.3. We have also introduced the basic concepts of evolution equations of parton densities 2 and the concept of parton saturation 2.3. We have numerically solved the Balitsky-Kovchegov evolution equation (2.13) and examined the dependence of the solution $N(r, Y)$ on the choice of the kernel prescription, initial condition, order of the numerical Runge-Kutta method and the choice of heavy quarks contribution. A prediction of the structure function F_2 in deep inelastic scattering was obtained with the use of GBW parametrization (1.31) and also with the use of rcBK equation given by (2.13) with the kernel 2.17 and the initial condition (2.19). These predictions were compared with the data from HERA experiments 4.1. We have also estimated the predictions of the exclusive J/ψ vector meson production and compared them to the data from H1 and ALICE experiments. The predictions were obtained using a GBW parametrization and also using the solution to the rcBK equation with the pressumption of the parametrization the transverse structure of the proton with the Gaussian distribution. We have also obtained the prediction for the exclusive J/ψ production by modelling the proton transverse structure with the so-called hot-spot model. Therefore all the tasks of this master's thesis assigment were successfully fulfilled.

Appendices

Appendix A

Numerical methods

A.1 Runge-Kutta methods

By the term Runge-Kutta (RK) methods we usually denote several numerical methods which we use to approximate the solution of differential equations of the first order with an initial condition, the *Cauchy problem*

$$y'(x) = f(x, y(x)), \qquad y(x_0) = y_0. \tag{A.1}$$

According to [65] let $I = (x_0, x_0 + T)$ be the integration interval with $T \in (0, \infty)$ fixed and for $h > 0$ let $x_n = x_0 + nh$ with $n = 0, 1, ...N_h$. Then points x_n are the discretization nodes which divide I into the set of subintervals $I_n = [x_n, x_{n+1}]$. Integer N_h is the maximum integer which fulfills the condition $x_{N_h} \leq x_0 + T$. Let us denote η_n the approximation at point x_n of the exact solution $y(x_n) \equiv y_n$, the value $f(x_n, \eta_n)$ is denoted as f_n and we obviously set $\eta_0 \equiv y_0$.

These methods are also called *one step* (or *single-point*) as the method uses the approximation η_n of the eq. (A.1) solution y_n to advance the approximation to the next value η_{n+1}. In the case that η_{n+1} depends only on η_n we call the method *explicit*. Otherwise, it is called an *implicit method*. In the following text we will focus on explicit methods only as we do not make use of the any of implicit methods.

A Runge-Kutta method can be written in its most general form as [65]

$$\eta_{n+1} = \eta_n + h\Phi(x_n, \eta_n, h; f) \tag{A.2}$$

where Φ is the increment function which depends on the step size h as follows:

$$\Phi(x_n, \eta_n, h; f) = \sum_{i=1}^{s} b_i K_i, \quad K_i = f\left(x_n + c_i h, \eta_n + h \sum_{j=1}^{s} a_{ij} K_j\right). \tag{A.3}$$

Coefficients a_{ij}, b_i and c_i fully describe an Runge-Kutta method and the following condition holds

$$c_i = \sum_{j=1}^{s} a_{ij}. \tag{A.4}$$

If the coefficients a_{ij} are equal to zero for $i \leq j$ the method is explicit and hence each K_i can be obtained using $i - 1$ coefficients $K_1, ...K_{i-1}$ that have already been determined in the previous step. The parameter s denotes the number of stages of the method which is for $s \leq 4$ equal to the order of the method. In the following text we will introduce three most common methods.

Euler method

Forward Euler method represents one of the Runge-Kutta method of the first order. It can be derived by the simple observation that $f(x, y(x))$ in (A.1) is the slope of $y(x)$. Therefore, for $h \neq 0$ it approximately stands [66]

$$y(x+h) = y(x) + hf(x, y(x)). \tag{A.5}$$

Starting with an initial condition $y_0 \equiv u_0$ defined in (A.1) and using a step length h one thus arrives to approximations η_n to the values y_n of the exact solution at equidistant points $x_n = x_0 + nh$ given by the following relationship

$$\eta_{n+1} = \eta_n + hf(x_n, \eta_n), \qquad x_{n+1} = x_n + h. \tag{A.6}$$

For the Euler method the function $\Phi(x_n, \eta_n, h; f)$ in the general relation (A.2) is therefore simply equal to $f(x_n, y(x_n))$ in the limit of $h \to 0$. For the ilustration, the graphical interpretation of the method can be seen in Figure 4.32.

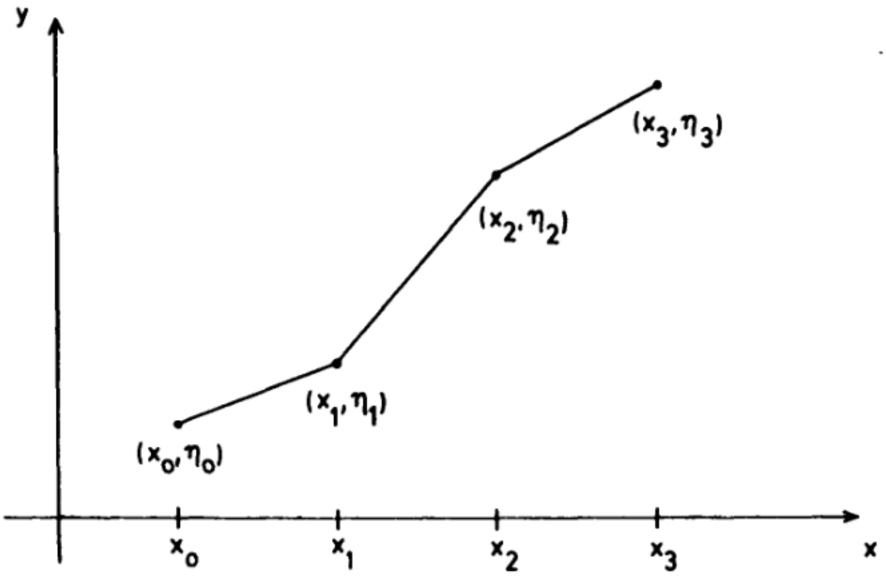

Figure 4.32: Graphical interpretation of the Euler method. [66]

Heun's method

Heun's method represent a second order Runge-Kutta method. Indeed, if we take $s = 2$ in general relation (A.2) we obtain for the step size $h \neq 0$ the approximation of the exact solution y_n at $(n+1)$-th step as [65]

$$\eta_{n+1} = y_n + h\Phi(x_n, y_n, h; f) = y_n + h(b_1 K_1 + b_2 K_2)$$

where

$$K_1 = f(x_n, y(x_n)) \equiv f_n, \quad \text{and} \quad K_2 = f(x_n + hc_2, y_n + hc_2 K_1).$$

Expanding K_2 to the 2^{nd} order of the Taylor series in the neighbourhood of point x_n we get for the approximation at $(n+1)$-th step

$$\eta_{n+1} = y_n + hf_n(b_1 + b_2) + h^2 b_2 c_2 (f_{n,x} + f_n f_{n,y}) + O(h^3)$$

where by $f_{n,x}$ and $f_{n,y}$ we denote the partial derivative of f_n evaluated at (x_n, y_n). Comparing the previous expansion to the same expansion performed on the exact solution

$$y_{n+1} = y_n + hy_n' + \frac{h^2}{2} y_n'' + O(h^3) = y_n + hf_n + \frac{h^2}{2}(f_{n,x} + f_n f_{n,y}) + O(h^3)$$

we obtain that the coefficients of the Runge-Kutta method have to satisfy

$$b_1 + b_2 = 1 \quad \text{and} \quad b_2 c_2 = \frac{1}{2}.$$

There exist two solutions to the above relations. The RK coefficients are in case of Heun's method as follows

$$b_1 = \frac{1}{2}, \quad b_2 = \frac{1}{2} \quad \text{and} \quad c_2 = 1$$

and therefore the relation of the approximation at $(n+1)$-th steps for the Heun's method stands

$$\eta_{n+1} = \eta_n + \frac{h}{2}\left[f(x_n, \eta_n) + f\left(x_n + h, \eta_n + hf(x_n, \eta_n)\right)\right]. \tag{A.7}$$

Classical method

Using the equivalent method as in previous part where we derived the relation for Heun's method we can obtain the relation for approximations in the case of higher-stage methods, accounting for equivalent number of terms in the Taylor's expansion and therefore acquire higher-order Runge-Kutta methods.

The RK method of the 4^{th} order, also called the *classical method* can be obtained expanding the Taylor's series of the approximation and the exact solution to the fourth order. Due to its demanding nature will not perform the whole procedure here and we will only introduce the definition of the classical method.

For the RK method of fourth order the increment function $\Phi(x_n, \eta_n, h; f)$ stands as

$$\Phi(x_n, \eta_n, h; f) = \frac{1}{6}(K_1 + 2K_2 + 2K_3 + K_4)$$

where

$$\begin{aligned}
K_1 &= f(x_n, y(x_n)) \\
K_2 &= f\left(x_n + \frac{h}{2}, \eta_n + \frac{h}{2}K_1\right) \\
K_3 &= f\left(x_n + \frac{h}{2}, \eta_n + \frac{h}{2}K_2\right) \\
K_4 &= f\left(x_{n+1}, \eta_n + hK_3\right)
\end{aligned}$$

and the classical method is therefore defined as [65]

$$\eta_{n+1} = \eta_n + \frac{h}{6}(K_1 + 2K_2 + 2K_3 + K_4). \tag{A.8}$$

A.2 Lagrange interpolation

Interpolation methods represent a tool for the approximation of given functions at certain point x, assuming we know the values of the function at given set of points $[x_0, ...x_n]$ for $i = 0, 1, ..., n$. One of the cases of the set of interpolation techniques is the polynomial interpolation in which we obtain the desired value of the function using a polynom

$$P(x) \equiv a_0 + a_1 x + a_2 x^2 + ... + a_n x^n$$

of the degree n, which depends on $n + 1$ parameters $a_0, ..., a_n$.

Let us first introduce the theoretical basis of the polynomial interpolation methods, the general *Lagrange interpolation formula* [66]

$$P(x) \equiv \sum_{i=0}^{n} f_i L_i(x) \equiv \sum_{i=0}^{n} f_i \prod_{\substack{k=0 \\ k\neq i}}^{n} \frac{x - x_k}{x_i - x_k}, \tag{A.9}$$

where $P(x)$ is a polynomial of the degree $\leqslant n$ fulfilling $P(x_i) = f_i$ for $i = 0, ..., n$ and $L_i(x)$ are the Lagrange polynomials of the degree i which satisfy

$$L_i(x_k) = \delta_{ik} = \begin{cases} 1 & \text{if } i = k \\ 0 & \text{if } i \neq k \end{cases}$$

and thus we define [66] them as

$$L_i(x) := \frac{(x - x_0)...(x - x_{i-1})(x - x_{i+1})...(x - x_n)}{(x_i - x_0)...(x_i - x_{i-1})(x_i - x_{i+1})...(x_i - x_n)}.$$

For $n = 1$ the Lagrange polynomials are

$$L_0(x) = \frac{x - x_1}{x_0 - x_1} \qquad \text{and} \qquad L_1(x) = \frac{x - x_0}{x_1 - x_0}.$$

Using these we get a Lagrange interpolation of the 1st order, also called a *linear interpolation*

$$f(x) \equiv P(x) = \frac{f_1(x - x_0) - f_0(x - x_1)}{x_1 - x_0}, \qquad f_i = f(x_i), \quad i = 0, 1. \tag{A.10}$$

The above derived formula can be also rewritten as

$$f(x) = f(x_0) + \frac{f(x_1) - f(x_0)}{x_1 - x_0}(x - x_0) \tag{A.11}$$

of which we make use later on.

A.3 Simpson's rule

Simpson's rule is a numerical method for evaluation of the definite integral of a function if the values of the integrand over the integration interval are known. Simpson's rule is the special case of the so-called *Newton-Cotes integration formulas*. They can be obtained if we replace the integrated function $f(x)$ by an interpolating polynomial $P_n(x)$ of the order $n > 0$ [66]. Then

$$\int_a^b f(x)\mathrm{d}x \approx \int_a^b P_n(x)\mathrm{d}x. \tag{A.12}$$

Let us consider a uniform partition of the closed interval $[a, b]$ given by

$$x_i = a + ih, \qquad i = 0, ..., n,$$

where $h := \frac{b-a}{n}$ is the step length.

Using a Lagrange interpolation formula (A.9)

$$P_n(x) \equiv \sum_{i=0}^{n} f_i L_i(x), \qquad f_i := f(x_i) = P_n(x_i) \quad \text{and} \quad L_i(x) = \prod_{\substack{k=0 \\ k\neq i}}^{n} \frac{x - x_k}{x_i - x_k}. \tag{A.13}$$

Let us now introduce a new variable t which fulfills $x = a + ht$. Then $L_i(x)$ can be expressed as

$$L_i(x) = \phi_i(t) := \prod_{\substack{k=0 \\ k\neq i}}^{n} \frac{t - k}{i - k}. \tag{A.14}$$

Integrating the interpolating polynomial we obtain

$$\int_a^b P_n(x) = \sum_{i=0}^{n} f_i \int_a^b L_i(x)\mathrm{d}x = h \sum_{i=0}^{n} f_i \int_0^n \phi_i(t)\mathrm{d}t = h \sum_{i=0}^{n} f_i \alpha_i.$$

If we conclude all the above derived relationships, the Newton-Cotes integration formulas which give an approximate value of the definite integral from the function $f(x)$ over the finite interval $[a, b]$ can be written as

$$\int_a^b f(x)\mathrm{d}x \approx \int_a^b P_n(x)\mathrm{d}x = h \sum_{i=0}^{n} f_i \alpha_i, \quad f_i = f(a + ih), \quad h := \frac{b-a}{n}. \tag{A.15}$$

The coefficients $\alpha_i := \int\limits_0^n \phi_i(t)\mathrm{d}t$ do not depend od the integrand function $f(x)$ nor the limits a, b. They depend solely on the degree n of the interpolating polynom.

For $n = 2$ the corresponding coefficients are $\alpha_0 = \frac{1}{3}$, $\alpha_1 = \frac{4}{3}$ and $\alpha_2 = \frac{1}{3}$. Using these coefficients we obtain the following rule

$$\int_a^b f(x)\mathrm{d}x \approx \int_a^b P_2(x)\mathrm{d}x = \frac{h}{3}\left[f_0 + 4f_1 + f_2\right] \tag{A.16}$$

which is called the *Simpson's 1/3 rule* [66].

Usually, Newton-Cotes formulas are not applied directly to the entire interval $[a, b]$. They are rather applied in each of the set of N subintervals into which the interval of integration $[a, b]$ is equidistantly divided. The total approximate value of the integral is then given as a sum of the approximations calculated in each of the intervals resulting in the so-called *composite rule*.

If N is an even number, the Simpson's rule (A.16) can be applied to each of subintervals $[x_{2i}, x_{2i+1}, x_{2i+2}]$ as described above and summing all of these $\frac{N}{2}$ subintegrals gives the *composite Simpson's rule*

$$\int_a^b f(x)\mathrm{d}x \approx \frac{h}{3}\left[f(a) + 2\sum_{i=1}^{\frac{N}{2}-1} f(x_{2i}) + 4\sum_{i=1}^{\frac{N}{2}} f(x_{2i-1}) + f(b)\right]. \tag{A.17}$$

The error $E(f)$ of the (A.17) is given as a sum of all $\frac{N}{2}$ individual errors to the Simpson's rule (A.16) applied on each of subintervals [66]

$$E(f) = \int_a^b P_n(x)\mathrm{d}x - \int_a^b f(x)\mathrm{d}x = \frac{h^5}{90}\sum_{i=0}^{\frac{N}{2}-1} f^{(4)}(\xi_i) = \frac{b-a}{180}h^4 f^{(4)}(\xi), \qquad \xi \in (a, b). \tag{A.18}$$

A.4 Special functions

Gamma function

The gamma function is defined [67] as

$$\Gamma(z) = \int_0^\infty t^{z-1}e^{-t}\mathrm{d}t \tag{A.19}$$

where z can in general be any complex number. It satisfies the recursive relation

$$\Gamma(z + 1) = z\Gamma(z).$$

Additionally, for complex numbers z, for which holds $\mathrm{Re}(z) > 1$, the reflection formula for $\mathrm{Re}(z) < 1$ can be expressed as

$$\Gamma(z)\Gamma(z - 1) = \frac{\pi}{\sin(\pi z)}.$$

For the z being an integer, gamma function can be related to factorial of n using

$$n! = \Gamma(n + 1).$$

Bessel functions of the First and the Second Kind

The Bessel functions of the first kind $J_\nu(x)$ are defined as the solutions to the *Bessel differential equation*

$$x^2\frac{\mathrm{d}^2y}{\mathrm{d}x^2} + x\frac{\mathrm{d}y}{\mathrm{d}x} + (x^2 - \nu^2)y = 0 \tag{A.20}$$

and can be expressed [67] by the series representation

$$J_\nu(x) = \left(\frac{x}{2}\right)^\nu \sum_{k=0}^{\infty} \frac{\left(-\frac{x^2}{4}\right)^k}{k!\Gamma(\nu + k + 1)}. \tag{A.21}$$

with ν being an integer.

The Bessel functions of the second kind $Y_\nu(x)$ (also called the Neumann functions $N_\nu(x)$) are the solutions to the Bessel differential equation (A.20) which is singular at its origin. It can be expressed for non-integer ν using the Bessel functions of the first kind (A.21) by the series representation

$$N_\nu(x) = Y_\nu(x) = \frac{J_\nu(x)\cos(\nu\pi) - J_{-\nu}(x)}{\sin(\nu\pi)}. \tag{A.22}$$

Modified Bessel functions of the Second Kind

Modified Bessel functions of the second kind $K_\nu(x)$ are (together with the modified Bessel functions of the first kind $I_\nu(x)$) one of the solutions to the *modified Bessel differential equation* [67]

$$x^2\frac{\mathrm{d}^2 y}{\mathrm{d}x^2} + x\frac{\mathrm{d}y}{\mathrm{d}x} - (x^2 + \nu^2)y = 0. \tag{A.23}$$

They can be expressed by the relationship

$$K_\nu = \frac{\pi}{2} i^{\nu+1} \left[J_\nu(ix) + iN_\nu(ix)\right] \tag{A.24}$$

for $\nu > 0$ and $x > 0$, using the above defined Bessel functions (A.21) and (A.22). As can be seen, modified Bessel functions correspond to the usual Bessel functions evaluated for purely imaginary arguments.

Appendix B

Numerical solution to the BK equation using Runge-Kutta methods

For the Balitsky-Kovchegov equation (2.13) we define following expressions [46]:

$$I_0 \equiv \int \mathrm{d}^2 r_1 K(r, r_1, r_2) \left[N(r_1, Y) + N(r_2, Y) - N(r, Y) - N(r_1, Y)N(r_2, Y)\right] \tag{B.1}$$

$$I_1 \equiv \int \mathrm{d}^2 r_1 K(r, r_1, r_2) \left[1 - N(r_1, Y) - N(r_2, Y)\right] \tag{B.2}$$

$$I_2 \equiv \int \mathrm{d}^2 r_1 K(r, r_1, r_2). \tag{B.3}$$

Eq. (2.13) is then solved numerically using Runge-Kutta methods presented in Chapter 2 over a grid in r. For the RK method of the 1st order, i.e. the forward Euler method, solution reads

$$N(r, Y + \Delta Y) = N(r, Y) + \Delta Y I_0, \tag{B.4}$$

for the RK method of the 2nd order, i.e. Heun's method, solution reads

$$N(r, Y + \Delta Y) = N(r, Y) + \Delta Y I_0 + \frac{(\Delta Y)^2}{2} I_0 I_1 - \frac{(\Delta Y)^3}{2} I_0^2 I_2 \tag{B.5}$$

and for the RK method of the 4th order, i.e. the Classical method, solution reads

$$N(r, Y + \Delta Y) = N(r, Y) + \frac{\Delta Y}{6} \left(I_0 + 2K_2 + 2K_3 + K_4\right) \tag{B.6}$$

where

$$\begin{aligned}
K_2 &\equiv I_0 + \frac{\Delta Y}{2} I_0 I_1 - \frac{(\Delta Y)^2}{4} I_0^2 I_2 \\
K_3 &\equiv I_0 + \frac{\Delta Y}{2} K_2 I_1 - \frac{(\Delta Y)^2}{4} K_2^2 I_2 \\
K_4 &\equiv I_0 + \Delta Y K_3 I_1 + (\Delta Y)^2 K_3^2 I_2.
\end{aligned}$$

Appendix C

Calculation of the derivatives of the scalar part of vector meson wave function

For the $1S$ vector meson states such as J/ψ the transverse and longitudinal scalar parts of the vector meson wave function using the boosted Gaussian model is given by the following description

$$\phi_{T,L}(r,z) = N_{T,L} z(1-z) \exp\left[-\frac{m_f^2 R^2}{8z(1-z)} - \frac{2z(1-z)r^2}{R^2} + \frac{m_f^2 R^2}{2}\right]. \tag{C.1}$$

The first derivative according to r is then calculated as

$$\partial_r\left(\phi_{T,L}(r,z)\right) = N_{T,L} z(1-z) \exp\left[-\frac{m_f^2 R^2}{8z(1-z)} - \frac{2z(1-z)r^2}{R^2} + \frac{m_f^2 R^2}{2}\right] \cdot \left(-\frac{4z(1-z)r}{R^2}\right)$$

resulting in

$$\partial_r\left(\phi_{T,L}(r,z)\right) = -\frac{4z(1-z)r}{R^2}\phi_{T,L}(r,z). \tag{C.2}$$

The second derivative to the $\phi_{T,L}(r,z)$ according to r is calculated as

$$\partial_r^2\left(\phi_{T,L}(r,z)\right) = -\frac{4z(1-z)}{R^2}\phi_{T,L}(r,z) - \frac{4z(1-z)r}{R^2}\partial_r\left(\phi_{T,L}(r,z)\right) =$$

$$= -\frac{4z(1-z)}{R^2}\phi_{T,L}(r,z) + \left(-\frac{4z(1-z)r}{R^2}\right)^2 \phi_{T,L}(r,z) = -\frac{4z(1-z)r}{R^2}\left[\frac{1}{r} - \frac{4z(1-z)r}{R^2}\right]\phi_{T,L}(r,z)$$

resulting in

$$\partial_r^2\left(\phi_{T,L}(r,z)\right) = \left[\frac{1}{r} - \frac{4z(1-z)r}{R^2}\right]\partial_r\left(\phi_{T,L}(r,z)\right). \tag{C.3}$$

And finally the Laplacian of the $\phi_{T,L}(r,z)$ in polar coordinates is given as

$$\nabla_r^2\left(\phi_{T,L}(r,z)\right) = \partial_r^2\left(\phi_{T,L}(r,z)\right) + \frac{1}{r}\partial_r\left(\phi_{T,L}(r,z)\right) = \left[\frac{1}{r} - \frac{4z(1-z)r}{R^2}\right]\partial_r\left(\phi_{T,L}(r,z)\right) + \frac{1}{r}\partial_r\left(\phi_{T,L}(r,z)\right)$$

resulting in

$$\nabla_r^2\left(\phi_{T,L}(r,z)\right) = \left[\frac{2}{r} - \frac{4z(1-z)r}{R^2}\right]\partial_r\left(\phi_{T,L}(r,z)\right). \tag{C.4}$$

Appendix D

Analytical solution to the integral over the impact parameter for the hot spots model

The scattering amplitude to the $\gamma^* p \to VMp$ process stands as

$$\mathcal{A}_{T,L}^{\gamma^* p \to VMp} = i \int \mathrm{d}^2 r \int_0^1 \frac{\mathrm{d}z}{4\pi} \int \mathrm{d}^2 b |\Psi_{VM}^* \Psi_{\gamma^*}|_{T,L} \exp\left[-i\left(\vec{b} - (1-z)\vec{r}\right)\vec{\Delta}\right] \frac{\mathrm{d}\sigma_{q\bar{q}}}{\mathrm{d}^2 b} \tag{D.1}$$

with the dipole cross section expressed as

$$\frac{\mathrm{d}\sigma_{q\bar{q}}}{\mathrm{d}^2 b} = \sigma_0 N(x,r) T_p(b) \tag{D.2}$$

where the profile function $T_p(b)$ in the hot spots model has the form

$$T_p(b) = \frac{1}{2\pi B_{hs} Nhs} \sum_{j=1}^{N_{hs}} \exp\left[-\frac{(\vec{b} - \vec{b}_i)^2}{2B_{hs}}\right]. \tag{D.3}$$

We can thus rewrite the amplitude $\mathcal{A}_{T,L}^{\gamma^* p \to VMp}$ as

$$\mathcal{A}_{T,L}^{\gamma^* p \to VMp} = i \int \mathrm{d}^2 r \int_0^1 \frac{\mathrm{d}z}{4\pi} |\Psi_{VM}^* \Psi_{\gamma^*}|_{T,L} e^{i(1-z)\vec{r}\vec{\Delta}} N(x,r) \frac{\sigma_0}{2\pi B_{hs} N_{hs}} \int \mathrm{d}^2 b e^{-i\vec{b}\vec{\Delta}} \sum_{j=1}^{N_{hs}} e^{-\frac{(\vec{b}-\vec{b}_j)^2}{2B_{hs}}} \equiv i\sigma_0 A_r A_b$$

where the part A_b can be, under the presumption that one can exchange the sum and the integral, solved in the following way:

$$A_b = \frac{1}{2\pi B_{hs} N_{hs}} \int \mathrm{d}^2 b e^{-i\vec{b}\vec{\Delta}} \sum_{j=1}^{N_{hs}} e^{-\frac{(\vec{b}-\vec{b}_j)^2}{2B_{hs}}} = \frac{1}{2\pi B_{hs} N_{hs}} \sum_{j=1}^{N_{hs}} \int \mathrm{d}^2 b e^{-i\vec{b}\vec{\Delta}} e^{-\frac{(\vec{b}-\vec{b}_j)^2}{2B_{hs}}}$$

Performing the substitution $\vec{c} = \vec{b} - \vec{b}_i$ we obtain:

$$A_b = \frac{1}{2\pi B_{hs} N_{hs}} \sum_{j=1}^{N_{hs}} e^{-i\vec{b}_j\vec{\Delta}} \int \mathrm{d}^2 c e^{-i\vec{c}\vec{\Delta}} e^{-\frac{c^2}{2B_{hs}}} = \frac{1}{2\pi B_{hs} N_{hs}} \sum_{j=1}^{N_{hs}} e^{-i\vec{b}_j\vec{\Delta}} \int \mathrm{d}^2 c e^{-\frac{1}{2B_{hs}}\left(c^2 + 2i\vec{c}B_{hs}\vec{\Delta}\right)} =$$

$$= \frac{1}{2\pi B_{hs} N_{hs}} \sum_{j=1}^{N_{hs}} e^{-i\vec{b}_j\vec{\Delta}} \int \mathrm{d}^2 c e^{-\frac{1}{2B_{hs}}\left((\vec{c} + iB_{hs}\vec{\Delta})^2 + B_{hs}^2\Delta^2\right)}$$

Next we shall substitute $\vec{f} = \vec{c} + iB_{hs}\vec{\Delta}$ resulting in:

$$A_b = \frac{1}{2\pi B_{hs} N_{hs}} \sum_{j=1}^{N_{hs}} e^{-i\vec{b}_j\vec{\Delta}} \int \mathrm{d}^2 f e^{-\frac{1}{2B_{hs}}\left(f^2 + B_{hs}^2\Delta^2\right)} = \frac{1}{2\pi B_{hs} N_{hs}} \sum_{j=1}^{N_{hs}} e^{-i\vec{b}_j\vec{\Delta}} e^{-\frac{B_{hs}\Delta^2}{2}} \int_0^{+\infty} 2\pi f \mathrm{d}f e^{-\frac{f^2}{2B_{hs}}}$$

and finally we shall substitute $g = -\frac{f^2}{2B_{hs}}$ with differentials obtained from the substitution as $f\mathrm{d}f = -B_{hs}\mathrm{d}g$ resulting in

$$A_b = \frac{2\pi}{2\pi B_{hs}N_{hs}}\sum_{j=1}^{N_{hs}} e^{-i\vec{b}_j\vec{\Delta}}e^{-\frac{B_{hs}\Delta^2}{2}}\int\limits_0^{-\infty}(-B_{hs})\mathrm{d}ge^g = \frac{1}{N_{hs}}\sum_{j=1}^{N_{hs}} e^{-i\vec{b}_j\vec{\Delta}}e^{-\frac{B_{hs}\Delta^2}{2}}\int\limits_{-\infty}^{0}\mathrm{d}ge^g$$

Integrating over g we obtain for the b-dependent part of the $\gamma^* p \to VMp$ amplitude

$$A_b = e^{-\frac{B_{hs}\Delta^2}{2}}\frac{1}{N_{hs}}\sum_{j=1}^{N_{hs}} e^{-i\vec{b}_j\vec{\Delta}} \tag{D.4}$$

where the argument in the sum can be further decomposed as

$$\exp\left(-i\vec{b}_j\vec{\Delta}\right) = \cos\left(\vec{b}_j\vec{\Delta}\right) + i\sin\left(\vec{b}_j\vec{\Delta}\right).$$

The resulting scattering amplitude $\mathcal{A}_{T,L}^{\gamma^* p\to VMp}$ is then given as

$$\mathcal{A}_{T,L}^{\gamma^* p\to VMp} = i\sigma_0 e^{-\frac{B_{hs}\Delta^2}{2}}\left[\frac{1}{N_{hs}}\sum_{j=1}^{N_{hs}} e^{-i\vec{b}_j\vec{\Delta}}\right]\cdot\int \mathrm{d}^2r\int\limits_0^1\frac{\mathrm{d}z}{4\pi}|\Psi_{VM}^*\Psi_{\gamma^*}|_{T,L}e^{i(1-z)\vec{r}\vec{\Delta}}N(x,r). \tag{D.5}$$

Bibliography

[1] H1 and ZEUS Collaborations, *Combination of measurements of inclusive deep inelastic $e^{\pm}p$ scattering cross sections and QCD analysis of HERA data*, Eur. Phys. J. C 75 (2015) no. 12, 580.

[2] W. Greiner, S. Schramm and E. Stein, *Quantum Chromodynamics (Third Edition)*, Springer-Verlag Berlin, 2007, ISBN 978-3-540-48535-3.

[3] J. Chýla, *Quarks, partons and Quantum Chromodynamics*, textbook for lectures on Quantum Chromodynamics at MFF UK, Prague, 2003.
Available at: http://www-hep2.fzu.cz/ chyla/lectures/text.pdf

[4] R. P. Feynmann, *Very High-Energy Collisions of Hadrons*, Phys. Rev. Lett. 23 (1969) 1415.

[5] J. D. Bjorken and E. A. Paschos, *Inelastic Electron-Proton and γ-Proton Scattering and the Structure of the Nucleon*, Phys. Rev. 185 (1969) 1975.

[6] B. R. Martin, *Nuclear and Particle Physics: An Introduction*, John Wiley & Sons, Ltd., 2006, ISBN-13: 978-0-470-01999-3.

[7] J. D. Bjorken, *Asymptotic Sum Rules at Infinite Momentum*, Phys. Rev. 179 (1969) 1547.

[8] H. Mantysaari, *Scattering off the Color Glass Condensate*, PhD Thesis, 2015, ISBN 978-951-39-6175-6.
Available at: arXiv:1506.07313

[9] H1 and ZEUS collaborations, *Combined Measurement and QCD Analysis of the Inclusive $e^{\pm}p$ Scattering Cross Sections at HERA*, JHEP 1001 (2010) 109

[10] H. Kowalski, L. Motyka and G. Watt, *Exclusive diffractive processes at HERA within the dipole picture*, Phys. Rev. D 74 (2006) 074016.

[11] H. Mantysaari, *Balitsky-Kovchegov equation*, Master's thesis, 2011.
Available at: http://users.jyu.fi/ hejajama/gradu/gradu.pdf

[12] S. Donnachie, G. Dosch, P. Landshoff and O. Nachtmann, *Pomeron Physics and QCD*, Cambridge University Press, 2002, ISBN 0-521-78039-X.

[13] K. Golec-Biernat and M. Wusthoff, *Saturation effects in deep inelastic scattering at low Q2 and its implications on diffraction*, Phys. Rev. D 59 (1998) 014017.

[14] Y. V. Kovchegov and E. Levin, *Quantum Chromodynamics at High Energy*, Cambridge University Press, 2012, ISBN 978-0-521-11257-4.

[15] J. L. Albacete, N. Armesto, J. G. Milhano, P. Quiroga-Arias and C. A. Salgado, *AAMQS: A non-linear QCD analysis of new HERA data at small-x including heavy quarks*, Eur. Phys. J. C 71 1705 (2011).

[16] K. Golec-Biernat and M. Wusthoff, *Saturation in diffractive deep inelastic scattering*, Phys. Rev. D 60 (1999) 114023.

[17] J. Bartels, K. Golec-Biernat and H. Kowalski, *Modification of the saturation model: Dokshitzer-Gribov-Lipatov-Altarelli-Parisi evolution*, Phys. Rev. D 66 (2002) 014001.

[18] E. Iancu, K. Itakura and S. Munier, *Saturation and BFKL dynamics in the HERA data at small-x*, Phys. Lett. B 590 (2004) 199.

[19] M. Arneodo and M. Diehl, *Diffraction for non-believers*, Proceedings of the Workshop on HERA and the LHC, DESY and CERN, 2004-2005.
Available at: arXiv:hep-ph/0511047

[20] J. Bartels, K. Golec-Biernat and K. Peters, *On the Dipole Picture in the Nonforward Direction*, Acta Phys. Polon. B 34 (2003) 3051.

[21] J. Nemchik, N. N. Nikolaev and B. G. Zakharov, *Scanning the BFKL pomeron in elastic production of vector mesons at HERA*, Phys. Lett. B 341 (1994) 228.

[22] J. Nemchik, N. N. Nikolaev, E. Predazzi and B. G. Zakharov, *Color dipole phenomenology of diffractive electroproduction of light vector mesons at HERA*, Z. Phys. C 75 (1997) 71.

[23] J. R. Forshaw, R. Sandapen and G. Shaw, *Color dipoles and ρ, ϕ electroproduction*, Phys. Rev. D 69 (2004) 094013.

[24] E. Iancu, *Clor Glass Condensate and its relation to HERA physics*, Nucl. Phys. Proc. Suppl. 191 (2009) 281-294.

[25] C. Marquet, *Open questions in QCD at high parton density*, Nucl. Phys. A904-905 (2013) 294c-301c.

[26] V. N. Gribov and L. N. Lipatov, *Deep inelastic ep scattering in parturbation theory*, Sov. J. Nucl. Phys. 15 (1972) 438-450.

[27] G. Altarelli and G. Parisi, *Asymptotic freedom in parton language*, Nucl. Phys. B 126 (1977) 298-318.

[28] Yu. L. Dokshitser, *Calculation of structure functions of deep-inelastic scattering and e^+e^- annihilation by perturbation theory in quantum chromodynamics*, Sov. Phys. JETP 46 (1977) 641.

[29] F. Halzen and A. D. Martin, *Quarks and Leptons - Introductory Course in Modern Particle Physics*, John Wiley & Sons, 1984, ISBN-13: 978-0471887416.

[30] V. S. Fadin, E. A. Kuraev and L. N. Lipatov, *The Pomeranchuk singularity in nonabelian gauge theories*, Sov. Phys. JETP 45 (1977) 199.

[31] Y. Y. Balitsky and L. N. Lipatov, Sov. J. Nucl. Phys. 28 (1978) 282.

[32] M. Kuhlen, *QCD at HERA: The Hadronic Final State in Deep Inelastic Scattering*, Springer-Verlag Berlin Heidelberg, 1999, ISBN 978-3-662-14733-7.

[33] F. Gelis, E. Iancu, J. Jalilian-Marian and R. Venugopalan, *The Color Glass Condensate*, Ann. Rev. Nucl. Part. Sci. 60 (2010) 463.

[34] J. L. Albacete, C. Marquet, *Gluon saturation and initial conditions for relativistic heavy ion collisions*, Prog. Part. Nucl. Phys. 76 (2014) 1.

[35] J. Jalilian-Marian, A. Kovner, A. Leonidov and H. Weigert, *The BFKL equation from the Wilson renormalization group*, Nucl. Phys. B 504 (1997) 415-431.

[36] J. Jalilian-Marian, A. Kovner, A. Leonidov and H. Weigert, *Wilson renormalization group for low x physics: Towards the high density regime*, Phys. Rev. D 59 (1998) 014014.

[37] E. Iancu, A. Leonidov, L. McLerran, *The renormalization group equation for the color glass condensate*, Phys. Lett. B 510 (2001) 133-144.

[38] E. Iancu, A. Leonidov, L. McLerran, *Nonlinear gluon evolution in the color glass condensate: I & II*, Nucl. Phys. A 692 (2001) 583-645 & Nucl. Phys. A 703 (2002) 489-538.

[39] A. H. Mueller, *A Simple Derivation of the JIMWLK Equation*, Phys. Lett B523 (2001) 243-248.

[40] Y. V. Kovchegov, *Small-x F_2 structure function of a nucleus including multiple Pomeron exchanges*, Phys. Rev. D 60 (1999) 034008.

[41] K. Rummukainen and H. Weigert, *Universal features of JIMWLK and BK evolution at small-x*, Nucl. Phys. A 739 (2004) 183-226.

[42] I. Balitsky, *Operator expansion for high-energy scattering*, Nucl. Phys. B 463 (1996) 99-157.

[43] A. H. Mueller, *Soft gluons in the infinite momentum wave function and the BFKL pomeron*, Nucl. Phys. B 415 (1994) 373-385.

[44] A. H. Mueller and B. Patel, *Single and double BFKL pomeron exchange and a dipole picture of high energy hard processes*, Nucl. Phys. B 425 (1994) 471-488.

[45] J. L. Albacete, N. Armesto, J. G. Milhano, C. A. Salgado and U. A. Wiedemann, *Numerical analysis of the Balitsky-Kovchegov equation with running coupling: dependence of the saturation scale on nuclear size and rapidity*, Phys. Rev. D 71 (2005) 014003.

[46] J. Cepila and J.G. Contreras, *Rapidity dependence of saturation in inclusive HERA data with the rcBK equation*, 2016.
arXiv:1501.06687v3

[47] E. G. de Oliveira, *Balitsky-Kovchegov evolution equation*, talk given at Universidade Federal do Rio Grande do Sul, 2009.
Available at: http://www.if.ufrgs.br/gfpae/sem/2008/BK.pdf

[48] A. Deur, S. J. Brodsky and G. F. de Teramond, *The QCD Running Coupling*, Prog. Part. Nuc. Phys. 90 (2016) 1-74.

[49] I. Balitsky, *Quark contribution to the small-x evolution of color dipole*, Phys. Rev. D 75 (2007) 014001.

[50] L. McLerran and R. Venugopalan, *Boost covariant gluon distributions in large nuclei*, Phys. Lett. B 424 (1998) 15-24.

[51] C. Marquet, *A unified description of diffractive deep inelastic scattering with saturation*, Phys. Rev. D 76 (2007) 094017.

[52] H1 Collaboration, *Elastic J/ψ production at HERA*, Eur. Phys. J. C 46 (2006) 585-603.

[53] K. Golec-Biernat, L. Motyka and A. M. Stasto, *Diffusion into infra-red and unitarization of the BFKL pomeron*, Phys. Rev. D 65 (2002) 074037.

[54] M. A. Braun, *Pomeron fan diagrams with an infrared cutoff and running coupling*, Phys. Lett. B 576 (2003) 115.

[55] K. Golec-Biernat, J. Kwiecinski and A. M. Stasto, *Geometric scaling for the total $\gamma^* p$ cross section in the low x region*, Phys. Rev. Lett. 86 (2001) 596-599.

[56] M. Matas, *Study of Properties of the Dipole Scattering Amplitude Using Balitsky-Kovchegov Evolution Equation*, Master's thesis, 2016.
Available at: https://physics.fjfi.cvut.cz/publications/ejcf/dp_ejcf_16_matas.pdf

[57] C. Patrignani et al. (Particle Data Group), Chin. Phys. C 40 (2016) 100001 and 2017 update.

[58] J. Cepila, J. G. Contreras and J. D. Tapia Takaki, *Energy dependence of the dissociative J/ψ photoproduction as a signature of gluan saturation at the LHC*, Phys. Lett. B 766 (2017) 186.

[59] J. Cepila, J. G. Contreras, M. Krelina and J. D. Tapia Takaki, *Mass dependence of vector meson photoproduction off protons and nuclei within the energy-dependent hot-spot model*, 2018.
arXiv:1804.05508

[60] H1 Collaboration, *Elastic J/ψ production at HERA*, Eur. Phys. J. C 46 (2006) 585-603.

[61] H1 Collaboration, *Elastic and proton-dissociative photoproduction of J/ψ mesons at HERA*, Eur. Phys. J. C 73 (2013) 2466.

[62] C. J. Geyer, *Stat 3701 Lecture Notes: Zero-Truncated Poisson Distribution*, University of Minnesota lectures on statistics, 2017.
Available at: http://www.stat.umn.edu/geyer/3701/notes/zero.html

[63] ALICE Collaboration, *Exclusive J/ψ photoproduction off protons in ultra-peripheral p-Pb collisions at* $\sqrt{s_{NN}} = 5.02$ TeV, Phys. Rev. Lett. 113 (2014) 232504.

[64] J. Cepila, J. G. Contreras and M. Krelina, *Coherent and incoherent J/ψ photonuclear production in an energy-dependent hot-spot model*, Phys. rev. C 97 (2018) 024901.

[65] A. Quarteroni, R. Sacco and F. Saleri, *Numerical Mathematics*, Springer-Verlag New York, 2000, ISBN 0-387-98959-5.

[66] J. Stoer and R. Bulirsch, *Introduction to Numerical Analysis (2^{nd} Edition in English)*, Springer-Verlag New York, 1993, ISBN 3-540-97878-X.

[67] W. H. Press et al., *Numerical Recipes in C: The Art of Scientific Computing (Second Edition)*, Cambridge University Press, 1992, ISBN 0-521-43108-5.